A new cosmic dust distribution model inside the Earth's orbit based on IKAROS-ALADDIN results

by

Takayuki Hirai

A dissertation submitted in partial fulfillment of the requirements for the degree of Doctor of Philosophy

Department of Space and Astronautical Science
The Graduate University for Advanced Studies Japan

March, 2014

Abstract

This dissertation investigates a new modeling of cosmic dust distribution inside the Earth's orbit mainly based on in-situ dust measurement data by the Arrayed Large-Area Dust Detectors in INterplanetary space (ALADDIN) onboard the Interplanetary Kite-craft Accelerated by Radiation of the Sun (IKAROS). In addition to the modeling work, laboratory calibration experiments with the ALADDIN flight-spare were conducted with hypervelocity microparticle accelerators and a nanosecond pulsed laser. Furthermore, analysis and reduction of the measurement data from the ALADDIN are also presented as part of the dissertation.

Recent optical observation results suggest that orbital trapping of 10–100's-μm-sized dust particles by planets' mean motion resonances (MMRs) and dust-dust collisions are key roles in sculpting morphology of debris disks in exo-planetary systems. As is the case with extrasolar planetary systems, dust disks in our Solar System, i.e., zodiacal dust cloud and Edgeworth-Kuiper belt, are also predicted to have the characteristic morphology governed by the dust-planet MMRs and the dust-dust collisions. In order to establish a general reference model for debris disks in planetary systems, some dust distribution models in the Solar System have been developed and validated mainly from optical observation results. However, optical observation faces difficulty in revealing fine structures of the dust disk such as local size distribution, attributed to fundamental characteristics of the optical observations such as physical complexity of visible light scattering and thermal infrared emission of dust particles, which are superimposed brightness from various sized dust particles that exist in an observer's line of sight. Moreover, optical observations from the vicinity of the Earth are not suited to investigate the inner planetary region than the Earth's orbit because of the sunlight interference. In order to uniquely determine the size distribution and investigate the fine structure within dust disks, in-situ dust impact detection along the trajectory of spacecraft is a more promising option. Nevertheless,

the dust distribution inside the Earth's orbit has not been well investigated even by in-situ detection until now, because of the lack of sufficient flight opportunities. Furthermore, all the past in-situ dust detectors have had only too small sensor areas to measure sparse distribution of the 10–100's-μm-sized dust particles, which are likely to be trapped in the planets' MMRs.

In these situations, the large-area in-situ dust detector based on PVDF named ALADDIN has been developed for IKAROS mission, in order to reveal the dust distribution between 0.7–1 AU. This study contributes to reveal and to model the size distribution and the fine structure of dust distribution, especially focusing on ≥10-μm-sized dust particles inside the Earth's orbit mainly by using measurement data of the IKAROS-ALADDIN during its 16 months orbiting around the Sun from 0.7 to 1 AU.

This thesis presents results of laboratory calibration of the ALADDIN flight spare with three types of experiments: hypervelocity (> 1 km/s) microparticle impacts at the 2 MV Van de Graaff dust accelerator, hypervelocity (> 1 km/s) 100's-μm-sized particle impacts with the two-stage light gas gun, and laser irradiation with the nano-second pulsed Nd:YAG laser. Considering the characteristics of analog signal processing of the ALADDIN's detector electronics, A modified signal acquisition system and signal analysis method, which utilizes signals measured at intermediate points of the analog circuits were developed. As the results of these calibration methods, it was verified that the detection size range of the dust particles onto the ALADDIN corresponds to 3–37 μm at the average impact velocity of 20 km/s at 1 AU heliocentric distance while representative dust density is 2.0 g/cm^3.

In addition to the laboratory calibration experiments focusing on the ALADDIN's analog signal, the ALADDIN measurement data were analyzed and reduced, by investigating the digital circuit characteristics of the ALADDIN electronics, multi-flagged features of some obtained data, and possible thermal degradation of the PVDF sensors. Based on the signal sampling rate of the analog-to-digital converter inside the digital electronics, sampling probabilities were calculated for a given amplitude of analog signal. Thus, it was found that impact events showing ≥4 V of measured signal amplitude, which are thought to be generated by impacts of ~30-μm or larger dust particles at 20 km/s, can be straightforwardly interpreted with the probabilistic sampling effect. A large portion of the ALADDIN space data have indicated multi-flagged features, which show more than one channels are flagged despite being caused by a single dust impact.

These multi-flagged events have recorded appropriate event rate as dust impact frequency in the interplanetary space. From its reproductive experiment on the ground and careful analysis of the flagged signal pattern, 736 high-confidence dust impact data at ≥4 V signal were determined on the ALADDIN's 20-μm-thick large sensors, among all the transmitted ~4500 data obtained during 16-month measurement in the Earth-Venus region.

In order to estimate the size of the detected dust particles at each IKAROS position of heliocentric distance, the in-flight thermal degradation of PVDF sensitivity were investigated through impact experiments of the heated large PVDF sensor. As the result, the possible thermal degradation of the ALADDIN PVDF seems not to affect significantly on the detectable size of impacting dust particles. Consequently, a total amount of such large dust particles detected by the ALADDIN measurement is more than 10 times of that of the past in-situ dust detectors. Thus, the applicability of the ALADDIN to measuring ≥10-μm-sized dust particles inside the Earth's orbit was verified. The dust particles in this size range correspond to the dust particles observed by optical observations and also the dominant-sized dust in the characteristic dust distribution governed by the planets' MMRs.

The number density calculated with part of the reduced ALADDIN data in the Earth's trailing region was compared with the existing standard dust flux model (Grün flux) at 1 AU heliocentric distance, which was established on the in-situ measurement at the vicinity of the Earth. It was found that there was a clear discrepancy between them which should be caused by the dust-Earth MMRs and the dust-dust collisions. In order to reproduce the observed azimuthal discrepancy, a new dust distribution model was developed by combining the existing MMRs-only model and the collision-only model. The new model has an ability to simultaneously handle the effect of the dust-planet MMRs and the dust-dust collisions for the dust distribution modeling in the interplanetary space. As the result, the newly developed model demonstrates a better estimate than the past MMRs-only model or the collision-only models for azimuthal variation of the dust number density at 1 AU heliocentric distance observed by the ALADDIN. In the future, this model calculation will be expanded to the Venus orbit for interpreting the ALADDIN data measured around its closest approach to Venus, and then a new comprehensive view of the cosmic dust distribution between the two planets-MMRs regions by the Earth and Venus can be achieved.

Contents

List of Figures

List of Tables

Chapter 1

Introduction

1.1 Debris Disks

Circumstellar dust disks, or debris disks, have been observed around Sun-like stars by astronomical telescopes with infrared and submillimeter wavelengths (Holland et al., 1998; Su et al., 2013). These debris disks are made from condensation of nebula gas and dust and continually replenished by outgassing and collisions among planetesimals. Fig. 1.1 shows a few examples of the observed disks.

These disks often show inhomogeneous morphology: asymmetric, shifted, warped, and ringed structures. It is believed that these inhomogeneities reflect the temporal state of planetary formation and existence of embedded planets inside the disks (e.g. Ozernoy et al., 2000; Zuckerman, 2001). Specifically, mean motion resonances (MMRs) between dust particles and planets, and dust-dust mutual collisions are key roles in evolution of the disk morphology (Stark and Kuchner, 2008; Wyatt, 2005; Wyatt et al., 1999). MMR is defined that the orbital periods of two celestial bodies are in some integer ratio.

Dust particles inside the disk transit from the source region to the central star under the radiation and wind drag forces, i.e. Poynting-Robertson (PR) effect (Robertson, 1937). The PR effect results in the decrease of the semi-major axis, a, and the eccentricity, e, of a dust particle's orbit according to Wyatt and Whipple (1950):

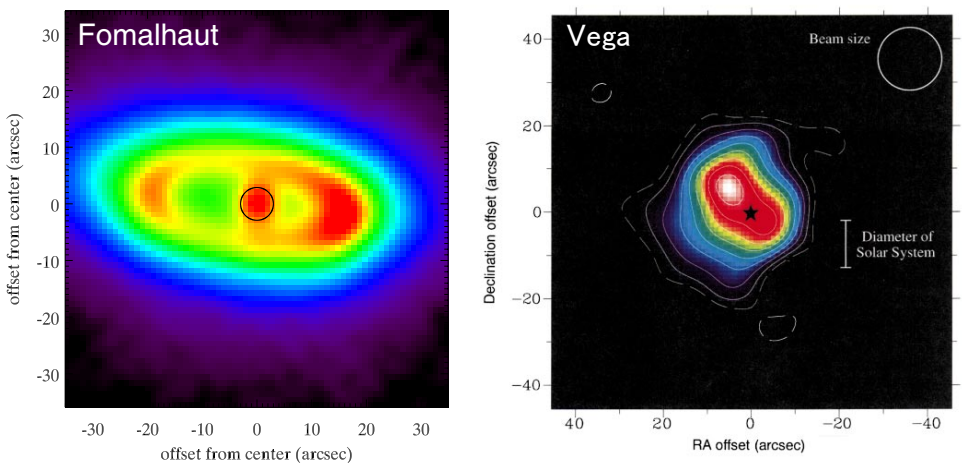

Fig. 1.1. Morphology of exo-debris disks. Fomalhaut observed at 70 μm (left: Su et al., 2013) and Vega observed by 850 μm (right: Holland et al., 1998).

$$\dot{a} = -(\alpha/a)(2 + 3e^2)/(1 - e^2)^{3/2} \tag{1.1}$$

and

$$\dot{e} = -2.5(\alpha/a^2)e/(1 - e^2)^{1/2} \tag{1.2}$$

where $\alpha = 6.24 \times 10^{-4}\beta$ AU^{2}yr^{-1}, and β is the ratio of radiation pressure force to the gravitational force on the dust particle. For spherical particles, β is given by

$$\beta = \frac{3L_\star Q_{\rm PR}}{16\pi G M_\star c \rho s} \tag{1.3}$$

where $L_\star$ is the stellar luminosity, $M_\star$ is the stellar mass, G is the gravitational constant, c is the speed of light, ρ is the mass density of a grain, s is the grain radius, and $Q_{\rm PR}$ is the radiation pressure coefficient (Burns et al., 1979).

A specific portion of the migrated dust particles, which have typical diameters of 10–100's-μm-sized in spherical silicates, is captured into external MMRs with planets and form ring structures along the planets' orbit, clumps at the leading and trailing positions of the planet, and a gap region nearby the planet (e.g. Dermott et al., 1994). Fig. 1.2 shows an example of the

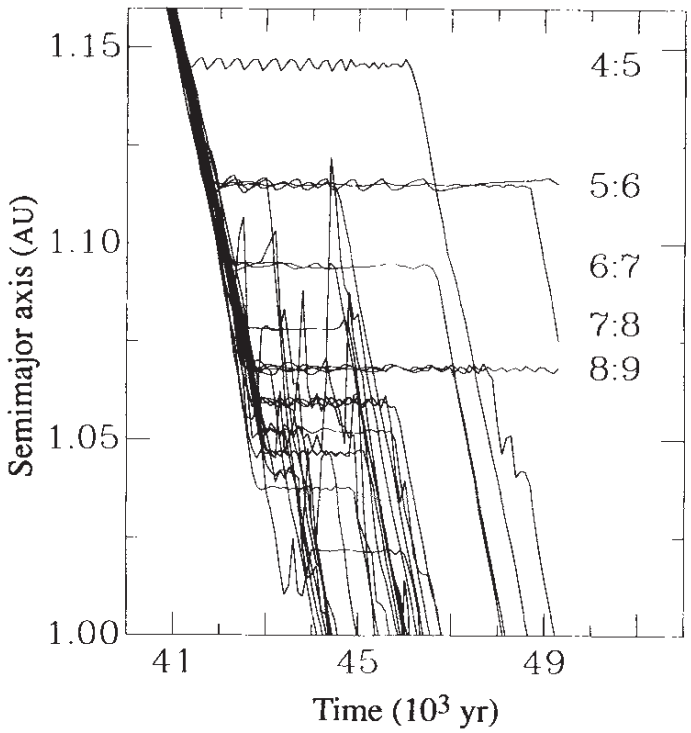

Fig. 1.2. The results of numerical calculation showing the orbital evolution of 12-μm-sized dust particles spiraling towards the Sun under the PR effect (Dermott et al., 1994). When the dust particles approach the Earth's external MMRs, a part of the particles get captured into each ratio of resonance.

orbital evolution of dust particles that are temporarily captured by the Earth's external MMRs.

While transiting through the interplanetary space, dust particles are exposed to dust-dust mutual collisions. The size distribution of the collisional fragments is given by

$$\frac{dN}{d\log m} = c_1 m^{-\eta} \ (m \leq m_{\mathrm{L}}) \tag{1.4}$$

where $\frac{dN}{d\log m}$ is the differential number density at log bin of dust mass, c_1 is a constant, m_{L} is the mass of the largest fragment, and η is the power law index which is ranging between 0.7–1.1 at hypervelocity (>1 km/s) impacts (Asada, 1985; Fujiwara et al., 1977; Gault and Wedekind, 1969; Nakamura and Fujiwara, 1991; Takasawa et al., 2011). These mutual collisions should naturally change the size distribution within the dust disk from location to location. Furthermore, higher number density of dust particles increased by MMRs stimulates the mutual

collisions.

Therefore, for comprehensive understanding of planetary formation and discovery of the embedded planets inside the dust disk that infer the mass and orbital elements of the planets, a realistic model of dust disk morphology considering both the effects of MMRs and dust-dust collision is required.

1.2 Solar System Dust Disks as References to Debris Disks

Dust disks in our solar system, known as zodiacal cloud and Edgeworth-Kuiper belt, are the best benchmark for validation of the dust disks morphology model because we can directly and closely observe or measure the dust distribution in detail. Also, we are well acquainted with the dynamical properties of planets orbiting inside the disks.

Several models for describing either dust-dust collisions or MMRs in the solar system dust disk have been proposed (Dermott et al., 1994; Ishimoto, 2000; Kelsall et al., 1998; Stark and Kuchner, 2008, 2009). These models are mainly validated by the observation results from visible to infrared telescopes onboard earth-orbiting satellites. For example, circumsolar dust accumulation accompanied with the asymmetric dust distribution at the trailing and leading side of earth was discovered and modeled by observational data from the Infrared Astronomical Satellite (IRAS). Fig 1.3 shows a model of discovered circumsolar dust distribution.

Optical observation in the dust disk of solar system is much closer compared to looking far out into the universe for exo-planetary disks. Nevertheless, there are fundamental difficulties in optical observation of dust distribution. The physics of light scattering and thermal infrared emission of dust particles are rather complicated, so it is difficult for optical observation to uniquely determine the size distribution of the dust disk. In addition, the brightness measured by optical instruments is a superimposed contribution from various sizes of the dust particles that exist in an observer's line of sight. These prohibit optical observations from detecting the fine variation of spatial number density and size distribution at given spatial positions.

In-situ dust impact detection is a more promising option in order to reveal the fine structure and size distribution within the dust disk in the interplanetary space. Also, in-situ detection is, in principle, not subjected to the sunlight interference, hence dust measurements at any given solar angles are possible.

Since the earliest stage of the solar system exploration in 1960's, in-situ dust measurements have provided valuable information about the size distribution and the fine component of dust in the solar system. In-situ dust detectors orbiting around earth contributed to determining the size distribution of incoming dust onto the Earth (e.g., Grün et al., 1985). Several detectors bound to the outer solar system discovered dust streams nearby the outer planets (Grün et al., 1993;

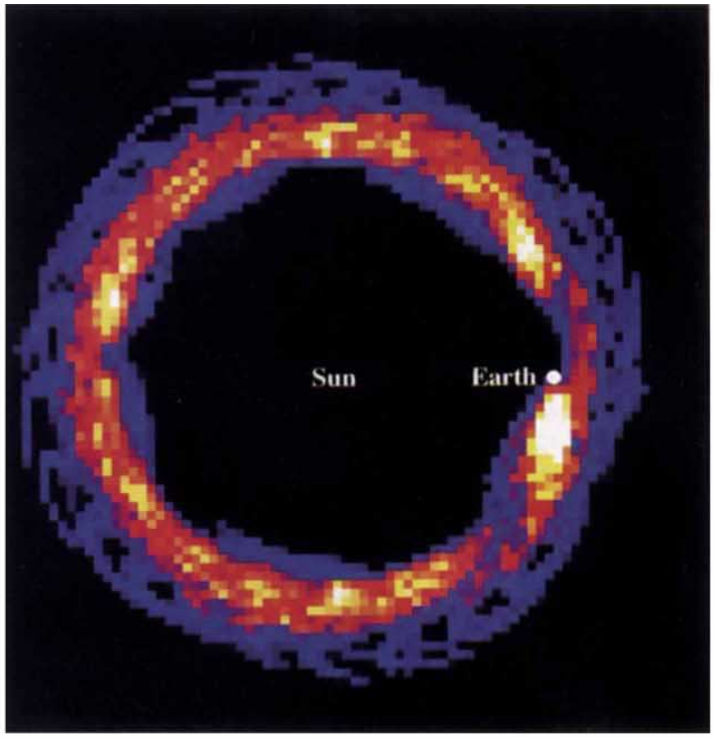

Fig. 1.3. Model of circumsolar dust ring around Earth's orbit composed of asteroidal dust particles (Dermott et al., 1994).

Kempf et al., 2005). However, the small sensor area of the conventional in-situ dust detectors onboard deep space exploration probes only posed insufficient flux of >10-μm-sized dust particles which preferably form the MMRs structure with planets. Therefore, in order to determine the fine structure and size distribution inside MMRs accumulation, there is a need for in-situ dust detectors having much larger sensor area for larger dust particles of >10-μm-sized than the past detectors. Moreover, there has been little flight opportunity for in-situ measurement inside 1 AU. As a result, information about large-sized dust distribution sensitive to MMRs inside 1 AU is highly valuable.

1.3 Objectives and content of the thesis

The primary objective of this thesis is to develop a new hybrid model, which simultaneously handles both the dust capturing by MMRs and the dust-dust mutual collisions, by combining existing MMRs models and collisions models for estimating dust distribution in the solar system, particularly within Earth orbit. The new model has revisited a standard model for dust distribution at 1 AU from the Sun (Grün model: Grün et al., 1985) and can be extended to 0.7 AU heliocentric distance in order to reveal dust distribution structure around Venus. The model flux calculated with given parameters such as initial size distribution and collisional fragment size distribution was compared with the dust flux measured in-situ by the Arrayed Large-Area Dust Detectors in INterplanetary space (ALADDIN) onboard the Interplanetary Kite-craft Accelerated by Radiation of the Sun (IKAROS), together with several results from the past in-situ dust detectors.

In order to properly assess the dust distribution model, the performance of the ALADDIN as an in-situ dust detector was investigated through laboratory calibration experiments using Van de Graaf dust accelerators, two-stage light gas guns, and a nano-second pulsed Nd:YAG laser. Also, the space data from ALADDIN were analyzed and reduced in order to extract the dust impact data from all the measurement data of ALADDIN transmitted to the ground station.

This thesis consists of 6 chapters including this introduction. Chapter 2 reviews optical observations, in-situ dust measurements, and dust distribution models inside the Earth's orbit. Chapter 3 describes the characteristics of the ALADDIN dust detector and the results of laboratory calibration experiments. In chapter 4, screening and reduction process and interpretation of the ALADDIN space data are presented. Chapter 5 proposes the new MMRs-collision hybrid model and describes the dust distribution at 1 AU from the Sun. Finally, Chapter 6 discusses conclusions and future works including the measurement results of ALADDIN at its Venus flyby and possible expansion of the new model to the Venus orbit.

Chapter 2

Past Observations, Measurements, and Distribution Models of Dust inside the Earth's Orbit

In this chapter, we will review the results and limitation of past optical observations, in-situ measurements, and dust distribution models inside the Earth's orbit. Because of fundamental characteristics in optical observations, e.g. light scattering theory, and small sensor area of detectors in in-situ measurements, detailed distribution of 10–100-μm-sized dust particle described in Chapter 1 has not been understood well.

2.1 Optical Observations for Dust Distribution within 1 AU from the Sun

Optical observations for dust distribution in the Solar System have been conducted by measuring visible light scattering and thermal infrared emission of dust particles. The diameter of dust particles contributing in these wavelengths is ranging from approximately 10 to 100 μm (Reach et al., 2003; Röser and Staude, 1978). Therefore, the optical observations in Solar System measure the superimposed brightness from 10 to 100-μm-sized dust particles that exist in an observer's line of sight. However, the sunlight, which is the most luminous body at the both wavelengths in the Solar System, have prevented us from optical observations of dust distribu-

tion within 1 AU from the Sun. In what follows, a few examples of the optical observations within 1 AU from the Sun are reviewed.

2.1.1 The Helios Photometers

Helios 1 and Helios 2 (also known as Helios-A and Helios-B) are a pair of spacecrafts to study the solar activity orbiting around the Sun between 0.3 and 1 AU heliocentric distance. After its launch in the middle of 1970s, photometers for the U-, B-, and V-bands (364 nm, 442 nm, and 540 nm, respectively) onboard Helios 1 and Helios 2 had made "in-situ" optical observation of interplanetary dust for 10 years (Leinert et al., 1981). Fig 2.1 shows radial increase of brightness observed by the photometer onboard Helios 2. The more brightness, the higher spatial number density of dust particles. The spatial number density of interplanetary dust calculated from the brightness-density conversion scheme is proportional to $r^{-1.3}$, r is radial distance from the Sun, as shown in Fig 2.1. Furthermore, Helios observation revealed asymmetric structure of the zodiacal dust disk induced by giant planets' secular perturbation (Leinert et al., 1980).

Leinert et al. (1983) proposed a dust-source distribution model based on the results from Helios 1 and Helios 2, and collisional evolution algorithm by Dohnanyi (1969). As a result, The source extended 0.1 AU$\geq a \geq$10 AU to 20 AU with the semimajor axes distributed $\sim a^{-1.0}$ or $\sim a^{-1.1}$ reproduce the observed number density profile along the heliocentric distance. However, MMRs between dust particles and planets is not considered in this model.

Leinert and Moster (2007) reanalyzed the Helios observation data around Venus orbit and suggested the existence of dust accumulated ring along Venus' orbital path.

Fig. 2.3 shows the trajectory of the Helios 2 spacecraft and Fig. 2.4 represents 5-year-averaged brightness variation around the Venus' orbit. The brightness is attributed to dust particles with 10–100 μm sized (Leinert et al., 1983). The observed brightness increased at Venus orbit crossing every time during the mission. They attributed the brightness increase to the ringed structure formed by 10–100 μm sized dust particles. The width of ring was estimated as 0.06 AU.

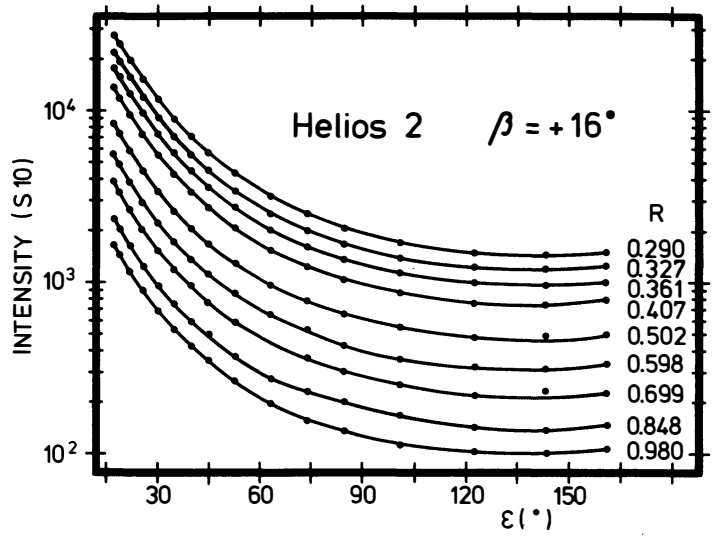

Fig. 2.1. Radial increase of the brightness observed by Helios 2 (Leinert et al., 1981). The unit of brightness is S10. The elevation of the line of sight was 15°.

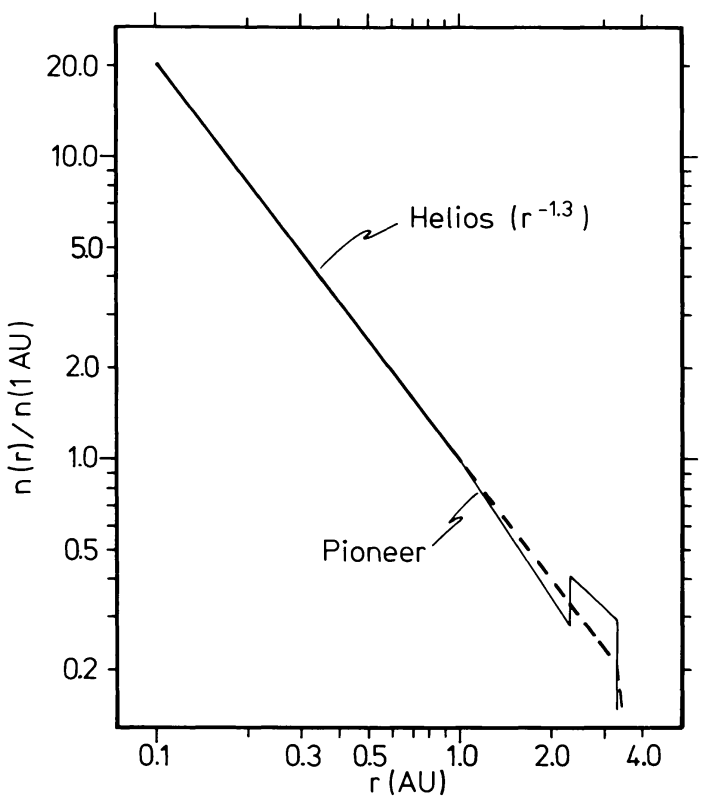

Fig. 2.2. Radial dependence of spatial number density of interplanetary dust inferred by Helios 1 and Helios 2 observations (Leinert et al., 1983).

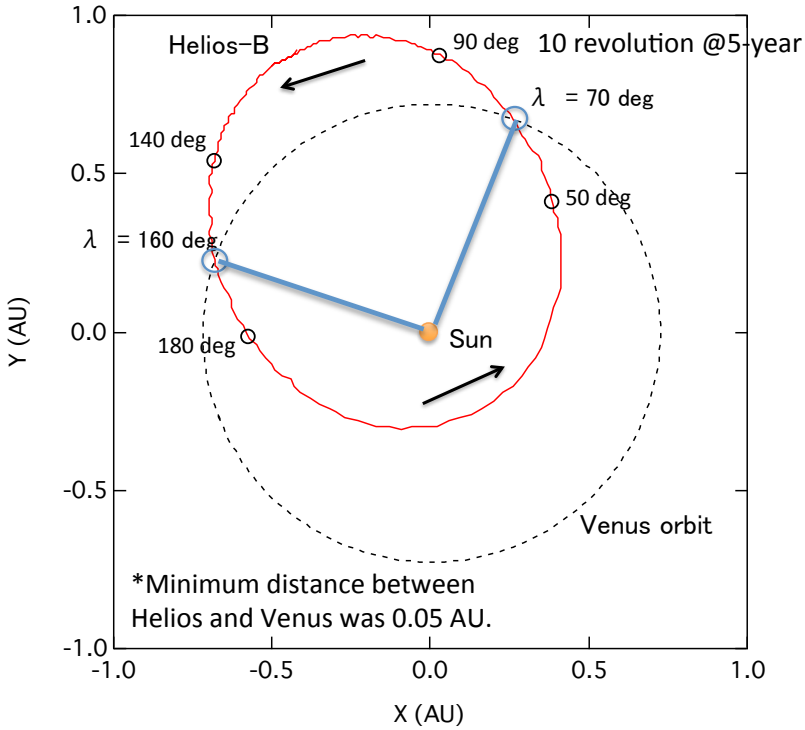

Fig. 2.3. Trajectory of the Helios 2 spacecraft in the J2000 inertial coordinate system. The ecliptic longitude corresponding to the range of horizontal axis in Fig. 2.4 are shown.

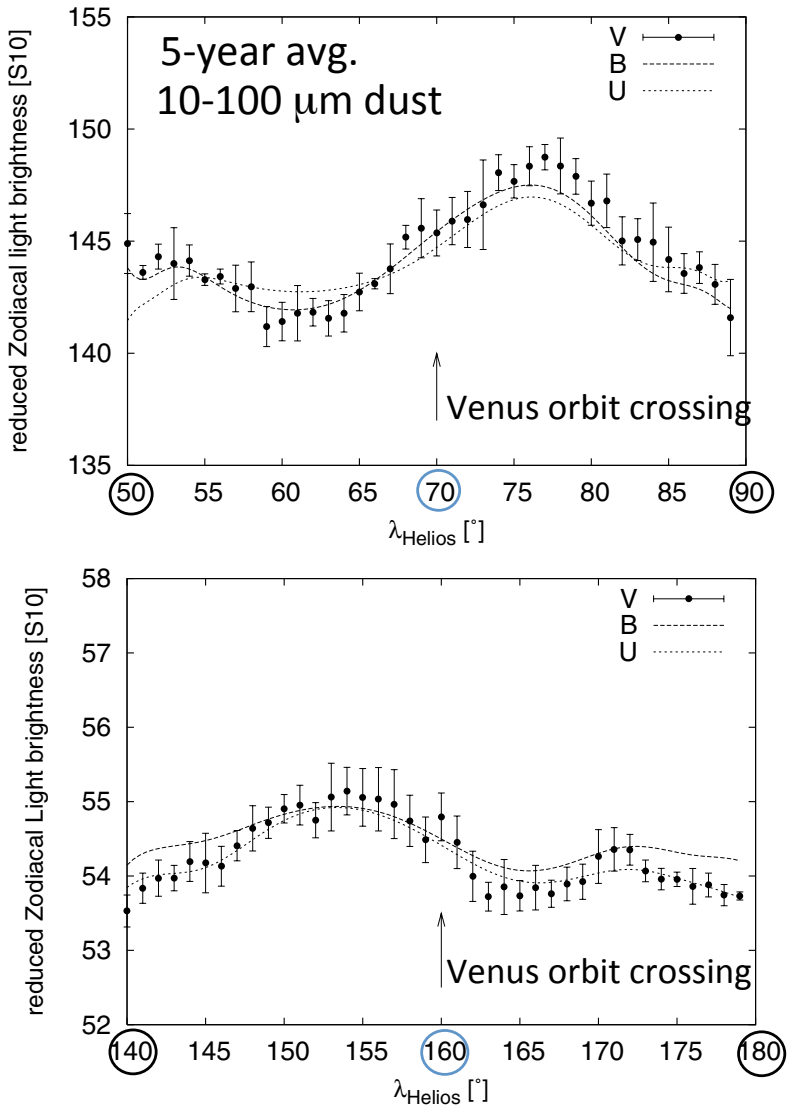

Fig. 2.4. Brightness profile observed by the Helios 2 photometer at crossing the Venus orbit (Leinert and Moster, 2007).

2.1.2 The Clementine Star Tracker Camera

Star tracker camera onboard the Clementine spacecraft observed brightness in visible wavelength (500–900 nm) due to dust distribution in the range of 10 solar radii to 0.6 AU by means of the Moon to occult the Sun. The results indicated $r^{-1.45}$ dependence on the number density (Fig 2.5) that is consistent with the Helios observation $r^{-1.3}$ (Hahn et al., 2002). The asymmetry of zodiacal dust distribution due to the giant planets' secular perturbation was found similar to Helios' observation. However, the brightness map does not reveal any other subtle features such as dust bands associated with asteroid families or dust trails associated with individual comets.

Considering inclination distribution of dust suppliers, Hahn et al. (2002) estimated contribution ratio from three dust sources; 1) low inclination group (asteroids and Jupiter-family comets), 2) high inclination group (Halley-type comets) and 3) isotropic group (Oort Cloud comets). The estimated ratio of low:high:isotropic is 0.45:0.5:0.05. This Hahn model does not include MMRs between dust particles and planets nor dust mutual collisions to simulate the observed brightness.

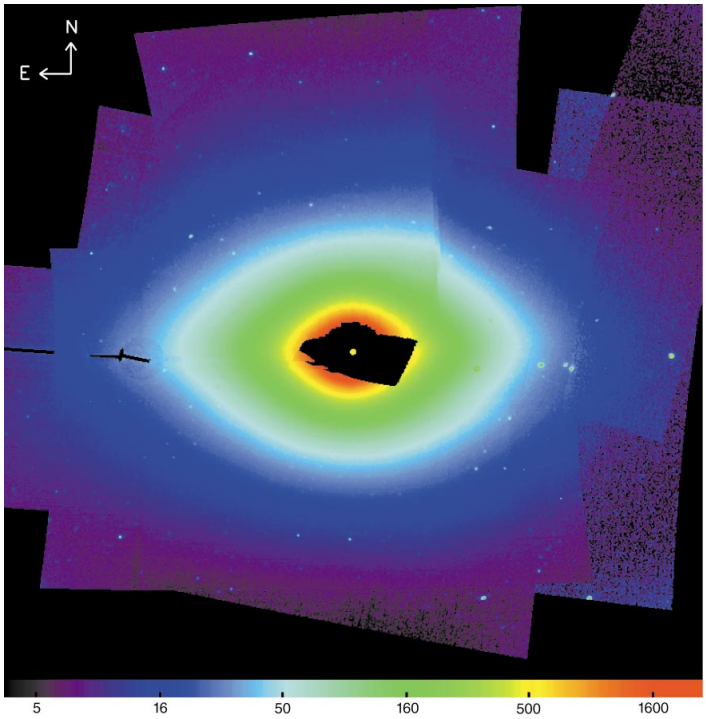

Fig. 2.5. The surface brightness observed by the Clementine star tracker camera (Hahn et al., 2002). A bulge region colored from blue to red corresponds to 0.05–0.6 AU.

2.1.3 The STEREO Imager

Heliospheric Imager instrument (HI-2) -A and -B onboard NASA STEREO-A and -B spacecraft remotely observed from near 1 AU the ring structure just outside the Venus orbit (Jones et al., 2013). The charge-coupled device (CCD) of the HI-2 has sensitivity to 400–1000 nm and dominant diffuse source in the image is solar radiation scattered by dust particles with 10–100 μm in radii.

The observation geometry of the HI-2 and obtained surface brightness are shown in Fig 2.6. Both the HI-2A and HI-2B tangentially looked at the dust ring with some range of ecliptic latitude. The obtained surface brightness shows enhancement around the orbit of Venus, which expands 5 or larger degree in both helioecliptic longitude and latitude. The estimated ring width, ~0.05 AU is consistent to that estimated by the Helios observation (0.06 AU). Also, they suggested the existence of trailing blob behind Venus, comparing the brightness profile whether the presence of Venus in the field of view or not.

The observation of dust ring by the STEREO HI-2 has delivered valuable knowledge about MMRs effect on dust distribution around the orbit of Venus. Nevertheless, detailed structure of trailing blob can not be revealed with the superimposed brightness along a line of sight.

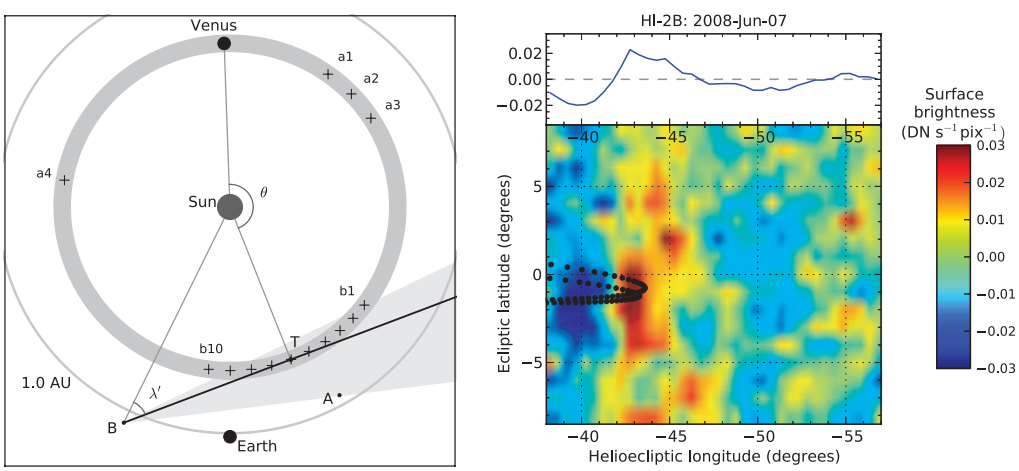

Fig. 2.6. Observation geometry of Heliospheric Imager instrument onboard the STEREO spacecraft (left) and obtained surface brightness (right) (Jones et al., 2013). The point A and B denote the position of STEREO spacecraft (A and B) and in this case a ring at Venus orbit is observed tangentially from B along the line of sight crossing at T. The observed surface brightness indicates double-peaked enhancement of dust number density at the orbit of Venus. For more details about the information of STEREO observation, see Jones et al. (2013).

2.2 In-situ measurements for Dust Distribution within 1 AU from the Sun

In-situ dust measurements have been performed mainly by impact ionization detectors (IIDs), which measures induced charge on the electrode of the detector's target generated by hypervelocity (> 1 km/s) impact of dust particles. IIDs has ability to obtain separately mass and velocity information of impacted dust particle and optionally chemical composition using time-of-flight mass spectrometry. However, increasing its sensor area brings higher weight of detector system than other type of in-situ dust detectors. Furthermore, IIDs need a room inside the detector to separate impact-generated plasma into negative ions and electrons and positive ions, so geometric factor of IIDs becomes narrow. Hence, it is not suitable for measuring the distribution of 10's-μm-sized dust particles in the interplanetary space. All the following three in-situ dust detectors are IIDs, measuring dust impact flux within 1 AU from the Sun.

2.2.1 The Helios 1 Dust Detector

The dust detector onboard Helios 1 performed the first and still only-one in-situ dust measurements reaching inward 0.3 AU from the Sun (Grün, 1981; Grün et al., 1980). Fig 2.7 illustrates the schematics of the Helios spacecraft installed with the dust detector and the trajectory of the spacecraft. The total sensor area of the Helios 1 dust detector consisting of the ecliptic sensor and the south sensor is 0.012 m^2. With this relatively small sensor area, the detector revealed the increase of number density of dust particles having mass range from 10^{-14} to 10^{-10} (0.2–5 μm in diameter) with decreasing heliocentric distance. The measured dust flux of larger than 10^{-12} g along heliocentric distances is depicted in Fig 2.8. Note that the Helios fluxes are averaged values over 10 revolutions around the sun during 5 years. Therefore, it is impossible to discuss MMRs structure formed by 10's micron dust with the measurement data of the Helios detector.

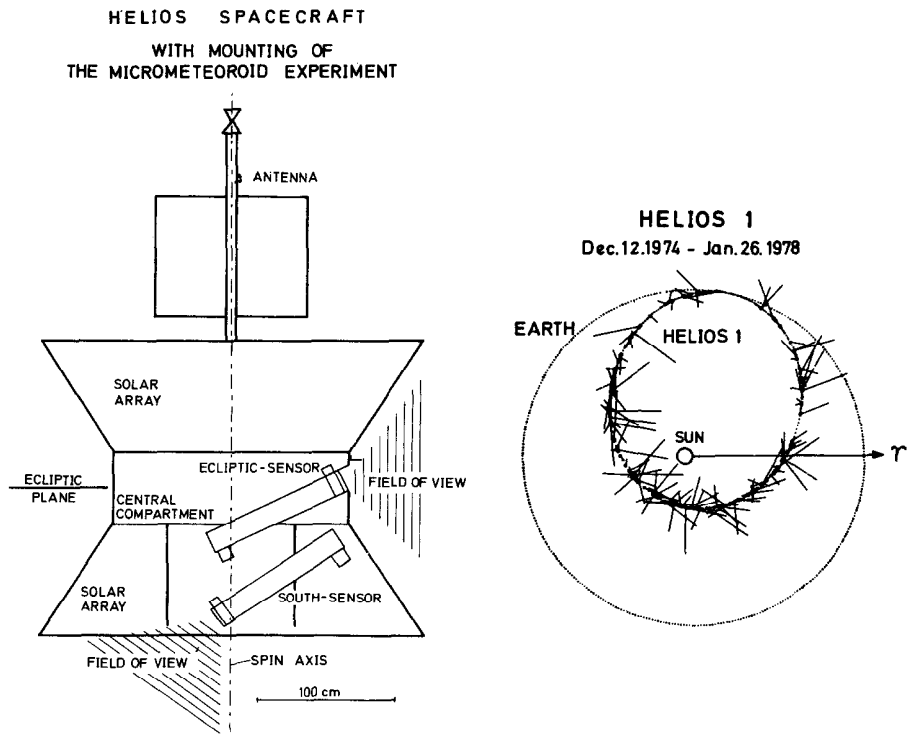

Fig. 2.7. Schematic of the Helios spacecraft installed with the dust detector and the trajectory of the spacecraft (Grün et al., 1980).

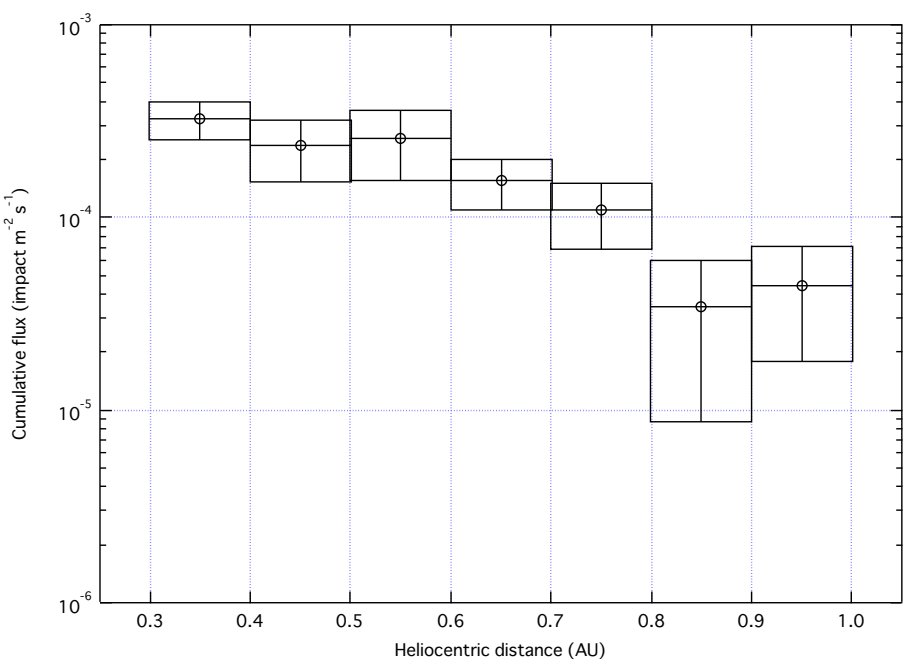

Fig. 2.8. Cumulative flux of $> 10^{-12} g$ dust along with heliocentric distance measured by the Helios in-situ dust detector (Grün, 1981). The vertical error denotes 1σ of Poisson statistics. The corresponding diameter is about 1 μm at the material density of 2.0 g/cm^3.

2.2.2 The Galileo Dust Detection System

The Dust Detection System (DDS) onboard NASA's Galileo spacecraft has 10 times larger sensor area (~0.1 m^2) than that of Helios 1, so some numbers of 10-μm-sized dust impacts were recorded. The Galileo spacecraft executed twice Earth swingby and once Venus swingby to head to Jupiter, hence the DDS measured dust impact flux inside 1 AU toward 0.7 AU of heliocentric distance. Fig 2.9 is a photograph of the DDS sensor and electronics box. The aperture of detector was nominally oriented toward anti-sun direction while the spacecraft orbited within 2 AU from the Sun. Impact flux of dust particles larger than 10-μm-sized measured by the DDS is shown in Fig 2.10. The data were recorded while the first inbound and outbound orbit of the Galileo spacecraft at its Venus flyby. The error bars of fluxes expand to one order or larger.

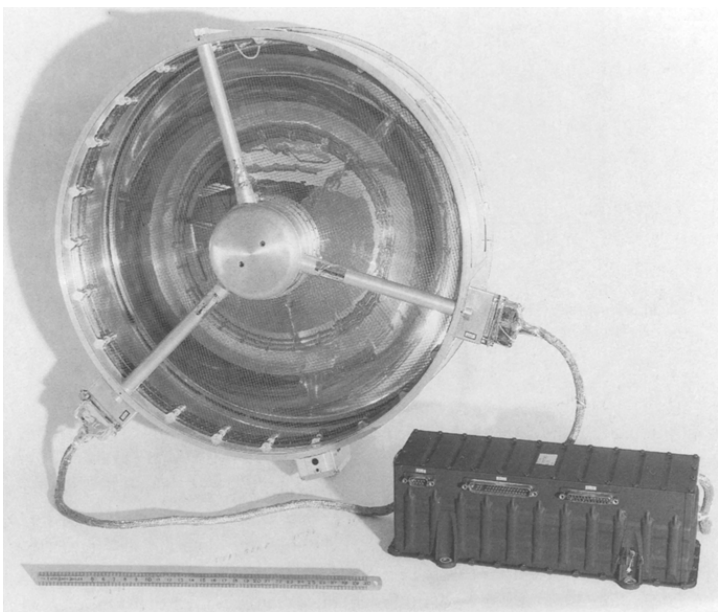

Fig. 2.9. The photograph of sensor and electronics box of the Galileo Dust Detection System (Grün et al., 1992).

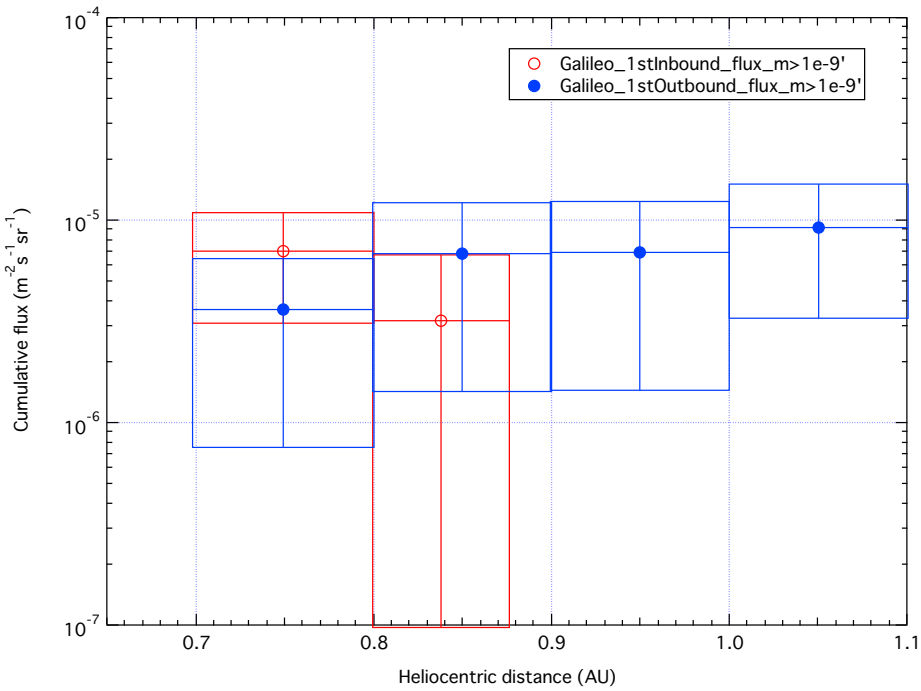

Fig. 2.10. Flux of 10-μm-sized dust particle (10^{-9} g in mass) along heliocentric distance measured by Galileo-DDS (from NASA Planetary Data System and Grün et al., 1995). The vertical error denotes 1σ of Poisson statistics.

2.2.3 The Cassini Cosmic Dust Analyzer

The Cosmic Dust Analyzer (CDA) of NASA's ongoing Cassini mission has nearly same sensor area as the DDS and a function of time-of-flight mass spectrometer inside the detector. The Cassini spacecraft took twice Venus swingby and once Earth swingby to reach Saturn, so the CDA measured dust impact flux inward to 0.7 AU same as the Galileo spacecraft. However, the CDA could not avoid photoelectron noise from sunlight irradiation on the sensor surface due to the attitude of the spacecraft. As a consequence, the CDA detected only 20 interplanetary dust particles of $\sim 10^{-16}$ kg (~0.5 μm in diameter) and 12 interstellar dust particles of 5×10^{-17} kg to 10^{-15} kg (0.4–1 μm in diameter) (Altobelli et al., 2003). Fig 2.11 shows the trajectory of the spacecraft and the direction of sensor axis when the CDA detected dust impacts. The CDA in-situ dust measurements have provided valuable information about interstellar dust penetrating into the inner solar system, but it is hard to model the dust distribution with its measurement data.

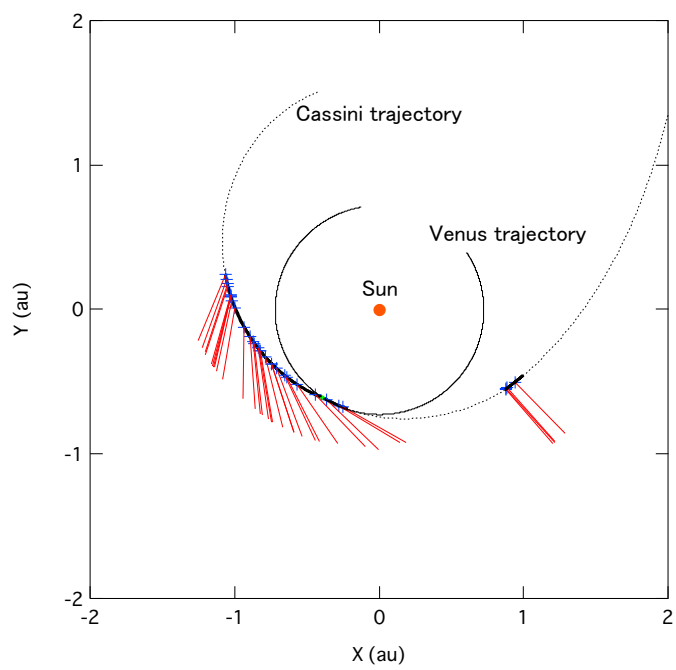

Fig. 2.11. The trajectory of the Cassini spacecraft and the direction of sensor axis at the dust impact detection (from NASA Planetary Data system, R. Srama (private communication), and Altobelli et al., 2003). The vertical error denotes 1σ of Poisson statistics. The dotted line of the trajectory denotes inactive state due to sunlight interference and the spacecraft maneuver.

Chapter 3

The ALADDIN Dust Detector

3.1 PVDF-Based Dust Detectors

3.1.1 Polyvinylidene Fluoride (PVDF)

Polyvinylidene fluoride (PVDF) is a type of semicrystalline, ferroelectric polymer composed of repeated chain of CH_2CF_2. Fig. 3.1 depicts the structural formula of PVDF. After uniaxial extension and polarization treatment, the processed PVDF film shows high piezoelectricity and pyroelectricity (Kawai, 1969; Wada and Hayakawa, 1976). In addition to the electrical properties, its mechanical strength and material flexibility make PVDF widely-utilized in various industrial products such as microphonic sensors or piezo actuators (e.g., Harsanyi, 1995). In the field of space science, Simpson and Tuzzolino (1984) started to investigate availability of PVDF sensors for detecting super-heavy charged nuclei since 1980's.

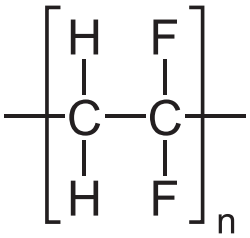

Fig. 3.1. Structural formula of PVDF.

3.1.2 Theory of Charge Production from PVDF at Hypervelocity Impacts and Nanosecond Laser Irradiation

Concurrently with research for charged nuclei detection by PVDF sensors, Simpson and Tuzzolino had probed the sensor response to hypervelocity impacts of micron-sized dust particles and short-pulsed laser irradiation (Simpson and Tuzzolino, 1985; Tuzzolino, 1983).

However, mechanism of charge production from PVDF at hypervelocity (>1 km/s) particle impacts has not been firmly established, some plausible theories have been presented (Poppe et al., 2010; Simpson et al., 1989; Simpson and Tuzzolino, 1985). Those theories all say that the charge fraction from piezo- and pyro-electricity of PVDF is negligible, while the main mechanism at hypervelocity impact is called "local depolarization".

Fig. 3.2 taken from Fig. 1 in Simpson and Tuzzolino (1985) represents a schematic drawing of a hypervelocity impact on a polarized PVDF sensor connected to a readout circuit. When a dust particle impacts on the PVDF sensor at hypervelocity, a crater or a penetration hole is formed on the PVDF within nanoseconds order. Upon the cratering or penetrating process, local rapid removal of dipoles, which is called "local depolarization", from inside the crater or hole volume causes a pulse current in short duration (nano-seconds order).

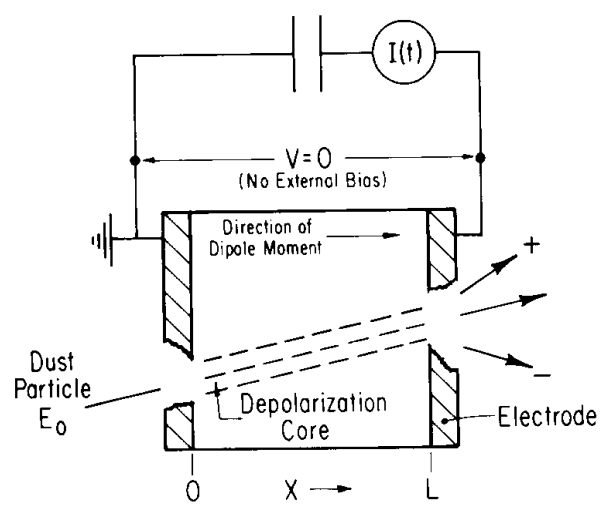

Fig. 3.2. Schematic diagram of hypervelocity impacts on a polarized PVDF sensor connected to a readout circuit (Simpson and Tuzzolino, 1985). The PVDF sensor of thickness L has a volume polarization directed along the x-axis. There is no external bias. A dust particle impact generates a fast current pulse I(t) in the readout circuit.

Based on the "local depolarization" theory, Simpson and Tuzzolino (1985) and Simpson

et al. (1989) have expressed the generated charge as a function of electrical properties of PVDF, specifically dielectric constant and polarization magnitude, and geometric properties of crater or penetration hole, i.e. the diameter and the depth.

In recent years, Poppe et al. (2010) have proposed a new theory for PVDF charge production at non-penetrating hypervelocity impacts. They have adopted a effect of fringing electric field at the crater formation, which modifies the surface charge density on the electrodes, and they have shown a better agreement with experimental results than the previous work by Simpson and Tuzzolino (1985). More theoretical works will be developed together with revealing works for cratering or penetration process on the PVDF film (e.g., Shu et al., 2013).

In spite of the dedication to development of a generic theory, these theories are not still exactly matched with the performance of specific PVDF-based detectors. Hence, empirical calibration is required for each specific PVDF-based dust detector by using, e.g., micro-particle accelerators. The calibration experiments of ALADDIN are presented in Section 3.5. A will be discussed in Section 3.6.2, the calibration of ALADDIN is related to only penetration impacts not cratering impacts.

Nano-second pulsed laser has been widely used in order to simulate hypervelocity impacts not only for development of dust or heavy nuclei detectors but also for simulation of hypervelocity impact phenomena in the solar system (Yamada et al., 1999).

Tuzzolino (1983) mentioned that the charge production from PVDF with pulsed laser irradiation is attributed to both piezoelectricity and pyroelectricity of the material. These two contributions have different time scale of charge production with the piezoelectric response to the acoustic energy being much faster than the pyroelectric response to the thermal energy. In his experiment with 0.4-μs-pulsed laser irradiation, signal response having <100 μs was observed.

In our case, we used nano-second pulsed laser in order to reproduce signal waveform being similar to that observed at hypervelocity impacts (Section 3.5.3). The fundamental mechanisms of charge production between hypervelocity impacts and short-pulsed laser irradiation summarized above are different, but we focused on the similarity of signal waveform and a total impact energy only and resulting signal waveforms seemed to be consistent in our experiments.

3.1.3 The Past PVDF-Based Dust Detectors

PVDF-based dust impact detectors have been utilized for a number of previous spacecraft, thanks to its mechanical and thermal stability, radiation hardness and non-responsiveness to energetic particle impacts. Here is a short list of such PVDF detectors in the past: the Dust Counter and Mass Analyzer (DUCMA) instrument (Simpson et al., 1986) onboard the Vega 1 and 2 spacecraft for comet Halley; the High Rate Detector (HRD) onboard the Cassini spacecraft for the Saturn system (Srama et al., 2004); the Dust Flux Monitor Instrument (DFMI) onboard the Stardust spacecraft (Tuzzolino et al., 2003); the Space Dust (SPADUS) instrument onboard the Earth orbiting Advanced Research and Global Observation Satellite (ARGOS) (Tuzzolino et al., 2005); the Venetia Burney Student Dust Counter (SDC) onboard the New Horizons spacecraft (Horanyi et al., 2008) for the Pluto system and the Edgeworth-Kuiper belt region; and the Cosmic Dust Experiment (CDE) onboard the Earth orbiting Aeronomy of Ice in the Mesosphere (AIM) satellite (Poppe et al., 2011). The ALADDIN onboard the IKAROS spacecraft has realized the largest sensor area among any previous PVDF-based dust detectors listed above (Fig. 3.3).

These PVDF-based dust detectors, including our ALADDIN, do not directly provide information about respective physical parameters of an impacted dust particle such as mass or impact velocity. In our case, general approach of measurement data analysis is to estimate the mass of impacted dust particles by presuming typical impact velocity and the material density of interplanetary dust particles.

3.2 Configuration and Characteristics of ALADDIN onboard IKAROS

The ALADDIN system consists of 8-channel PVDF sensors (ALDN-S) and the electronics box for impact signal processing (ALDN-E) (Yano et al., 2014; Yano et al., 2011). ALDN-S is attached on the anti-sun face of IKAROS's polyimide sail membrane, while ALDN-E is stored in the main body of the spacecraft and connected to the IKAROS's bus instrument called the SAIL-I/F through thin flexible harnesses. Fig. 3.4 shows a photograph of ALDN-S and the

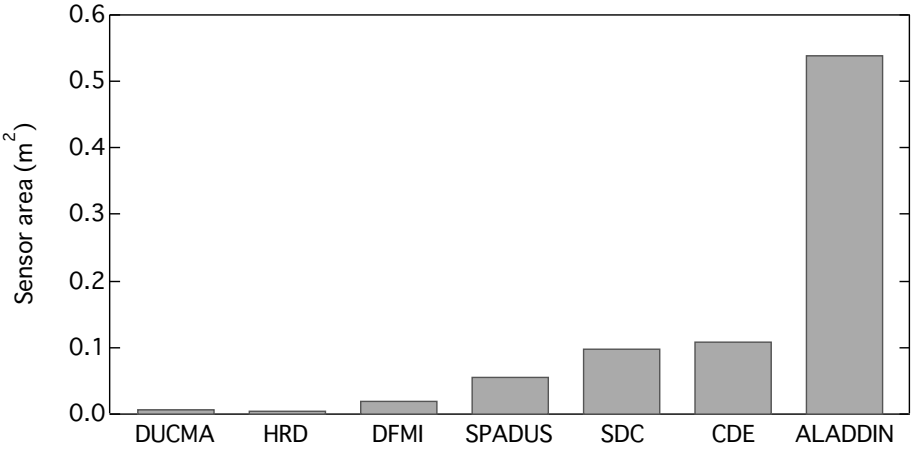

Fig. 3.3. Comparison of sensor area of various PVDF-based dust detectors. The specific values of area from DUCMA to ALADDIN are 0.0075 m^2 (Simpson et al., 1986), 0.006 m^2 (Srama et al., 2004), 0.022 m^2 (Tuzzolino et al., 2003), 0.0576 m^2 (Tuzzolino et al., 2005), 0.1 m^2 (Horanyi et al., 2008), 0.11 m^2 (Poppe et al., 2011) and 0.54 m^2.

schematic configuration on the IKAROS membrane. Four odd-numbered channels of ALDN-S correspond to the PVDF sensors of 20-μm-thick and 25 cm × 50 cm area and four even-numbered channels correspond to those of 9-μm-thick and 10 cm × 10 cm area, respectively. Their total sensor area of ALADDIN is 0.54 m^2. A pair of both sensors is allocated on each of 4 petals of the IKAROS sail membrane.

The 9-μm sensors were installed with the aim of measuring the different size of dust from the 20-μm sensors. However, in this study, our scientific priority is to measure the ≥10-μm-sized dust distribution, which is too sparse to be detected by the "small" 9-μm sensors. According to an interplanetary dust flux model by Grün et al. (1985), the 9-μm sensors (0.04 m^2 in total) detect one 10-μm-sized dust particle per 3 months at 1 AU. Therefore, we focused on the calibration tests for the 20-μm sensors.

Fig. 3.5 illustrates the multi-layered structure of the IKAROS sail membrane on which ALDN-S is attached. The normal of the membrane surface is almost vertically faced to the Sun in order to receive solar photon irradiation. This pointing had been controlled by tacking maneuver and varied to 30° at the maximum during the ALADDIN measurement.

In order to reduce alteration of its detection sensitivity at temperature change, the PVDF sensors of all the ALDN-S flight models and flight spares were thermally-aged at +100°C at their manufacturing process. Details of in-flight sensor temperature and thermal degradation of

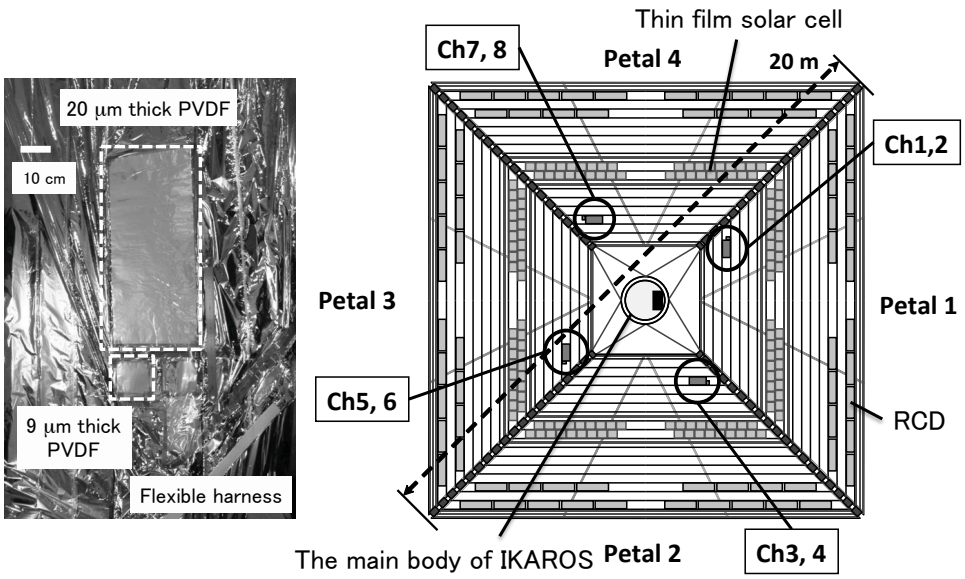

Fig. 3.4. Photograph of ALDN-S installed on the IKAROS membrane (left) and the configuration on the membrane viewed from the sun face (right). The Reflectivity Control Device (RCD) and thin film solar cells are also attached on the sun face, while the ALDN-S arrays are installed on the anti-sun face. Diagonal length of IKAROS membrane is 20 m.

PVDF will be presented in Chapter 4.

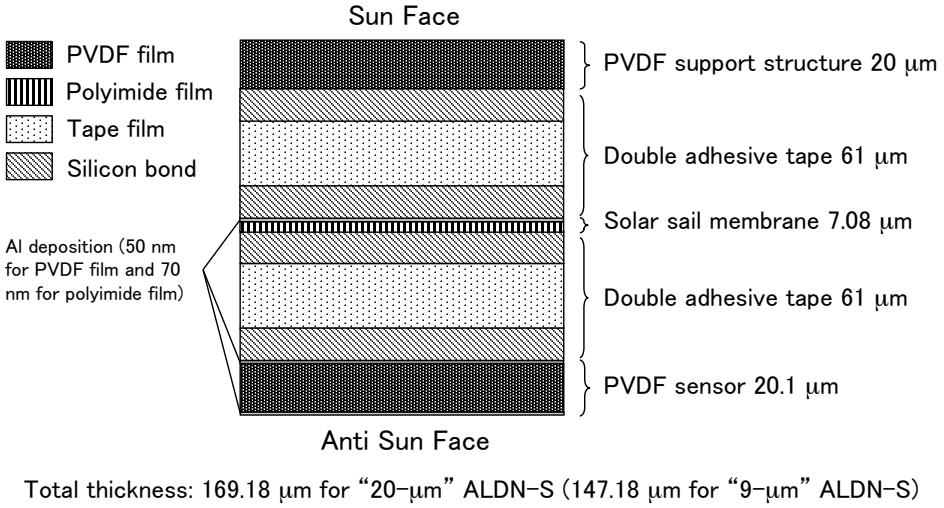

Fig. 3.5. The multi-layered structure of a part of IKAROS membrane on which the ALDN-S sensors are attached. For electrodes, the sensor side of PVDF film is coated with 50 nm of aluminum. PVDF films are known to be gently curled by alteration of the material temperature. Therefore, in order to compensate the curl of the anti-sun face PVDF sensor, the same size of PVDF support structure is attached on the sun-face of the membrane.

3.3 Functional Sequence

Fig. 3.6 depicts functional sequence of the ALADDIN-IKAROS system. When a dust particle impacts onto one channel of ALDN-S, depolarization charge is generated on its surface. The charge is processed via the analog circuit and then the peripheral interface controller (PIC) including analog-to-digital converters (ADC), which generates a digitized pulse signal and measures amplitude (dV) ranging from 0.03421 to 5 V and sampling counts (dt) as an indicator of signal duration for each of the 8 channels. If the sampled signal voltage exceeds the fixed threshold of 19.6 mV, the PIC generates event information that consists of dV, dt, clock time of the event occurrence, and the threshold voltage level. At the end, SAIL-I/F produces a packet data containing the event information to be transmitted to the ground station via the IKAROS telemetry. Consequently, the dV and dt values are obtainable output items on the ground.

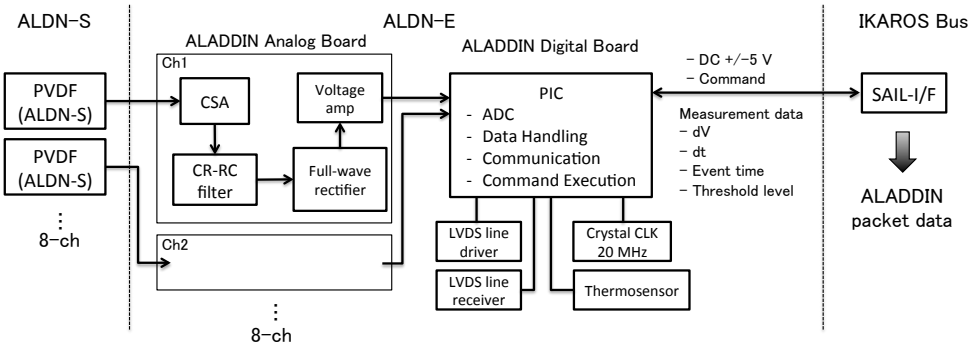

Fig. 3.6. Functional block diagram of the ALADDIN. Analog circuit is provided separately for each 8 channels of ALDN-S.

3.4 Analog Signal Processing

The signal processing of the ALADDIN is different from the past PVDF-based dust detectors in order to deal with its unique characteristics of charge production, which is probably attributed to the multi-layered structure of the IKAROS sail membrane as illustrated in Fig. 3.5. Here, we describe the processing procedure of analog signals within ALDN-E in detail. Also, we provide a brief explanation about uniqueness of a multi-layered PVDF sensor.

Fig. 3.7 shows the sequence of signal processing in the analog circuit and typical signal waveforms at each stage of the signal processing. The output signal of its charge sensitive

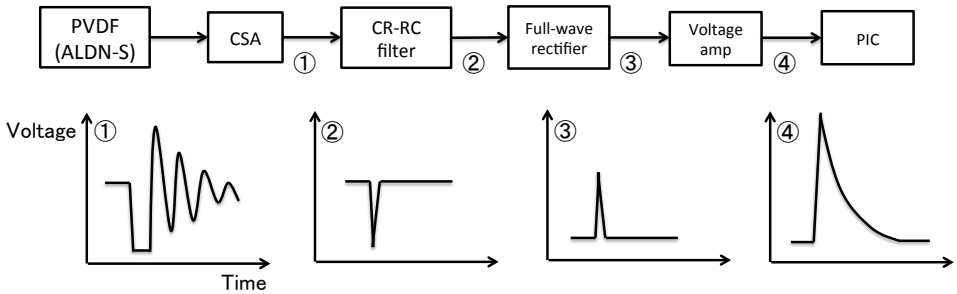

Fig. 3.7. Schematic of the signal processing at each stage within the ALDN-E analog circuit.

preamplifier (CSA) shows oscillating waveforms. If the magnitude of microparticle impact is large enough, the CSA output signal starts to saturate and then a component of specific frequency corresponding to the saturated part is extracted via the CR-RC band-pass filter. Next the shaper forms a full-wave rectified signal. At the end of the analog circuit, the voltage amplifier magnifies the formed signal and generates a final signal output. It is noted that an exceedingly large impact causes a final signal output having a multi-peaked waveform because, with such large impact, the CSA output signal should become saturated not only at the first fall of the signal but also at the following rises and falls. In fact, well-saturated and disturbed CSA signals were observed at the impact experiments with LGG.

The output signal of CSA within ALDN-E shows the oscillating waveforms, while past PVDF-based dust detectors such as DUCMA and SDC generates the transient signal at their output of CSA (Horanyi et al., 2008; Simpson et al., 1989). We think that major difference between ALADDIN and the past detectors, which triggers different mode of charge production, is the structure of sensor membrane in thickness direction. As is reasonably possible, impacts onto the multi-layered PVDF sensor such as ALDN-S would cause somewhat complicated impact energy dissipation inside the multi-layered structure where reflected shockwaves may be generated at the boundaries. In contrast, impacts onto the monolithic PVDF sensor can be regarded as transient phenomenon due to simple energy dissipation. Hence, the PVDF sensor of ALADDIN may be affected by disturbances of its backside layers at particle impacts and thus shows the different mode of signal generation compared to the past PVDF-based dust detectors.

3.5 Calibration Experiments

Calibration experiments should be conducted to determine the detector performance because there is no theory applicable to specific PVDF-based dust detectors as mentioned in Section 3.1. In-situ dust detectors, not only PVDF-based, are calibrated by hypervelocity impact experiment with dust-simulant small particles. For calibration of ALADDIN, we used Van de Graaff accelerators (VdG), Light Gas Guns (LGG), and nano-second pulsed Nd:YAG laser (nsPL).

3.5.1 Van de Graaff Dust Accelerator

As seen with a schematic in Fig. 3.8, general configurations inside the target vacuum chambers of both VdG and LGG experiments are very similar. As for the ALADDIN calibration tests with the VdG, we employed two facilities such as the High Fluence Irradiation Facility of the University of Tokyo (HIT) in Japan (Hasegawa et al., 2001; Shibata et al., 2001) and the Max-Planck-Institut für Kernphysik (MPIK) in Heidelberg, Germany (Mocker et al., 2011). Both accelerators are based on the same principle and they can accelerate electrically conductive dust grains of sub-micron to several microns in diameter up to ≥10 of km/s in impact velocity. Acceleration voltage in nominal operation we used were 1 MV at HIT and 1.8 MV at MPIK. At the HIT experiment, carbon and silver particles were used while at MPIK iron particles were accelerated. Target was the 20-μm-thick ALDN-S at both HIT and MPIK facilities.

Fig. 3.9 shows mass-velocity distribution at these VdG experiments. As a consequence no identifiable signal was observed even in the quite low signal to noise environment. This is not surprising, however, because the single sensor area of each piece of 20-μm-thick ALDN-S, which dictates its detector capacitance, is by far larger than that of any past PVDF-based dust detectors that were calibrated with VdG, aiming for dynamic ranges suitable mainly for micron-sized dust. In general, noise floor is proportional to the detector capacitance for CSA (Spieler, 2005) so that the VdG particles were too small to be detected by the ALADDIN which aims for ≥10-μm-sized dust. Consequently, we have found that the ALADDIN system is better suited for detecting dust particles at larger mass and velocity ranges than those achievable by the VdG facilities.

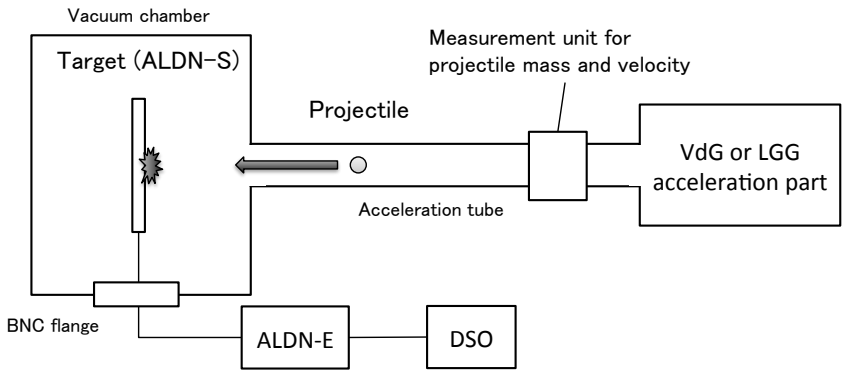

Fig. 3.8. Schematic diagram of microparticle impact experiments using VdG and LGG. The flight spares of the 20-μm-thick ALDN-S were placed inside a vacuum chamber and electronics including the flight spare of ALDN-E were outside the chamber. When a projectile from the acceleration part impacts vertically on the surface of ALDN-S at the velocity above 1 km/s, depolarization charge is processed in ALDN-E. Then a pulsed signal is generated and recorded in a digital storage oscilloscope. Measurement units for projectile mass and velocity for the VdG facility are a pair of cylindrical capacitors to estimate particle mass and velocity from induced charge signals. In particular at MPIK, a system for real-time mass and velocity selection of particle is equipped (Mocker et al., 2011). The LGG facility equips a pair of the laser curtains for estimation of particle velocity. The vacuum level at the VdG experiment was nominally less than 1×10^{-3} Pa, while at the LGG experiment 10 Pa on average.

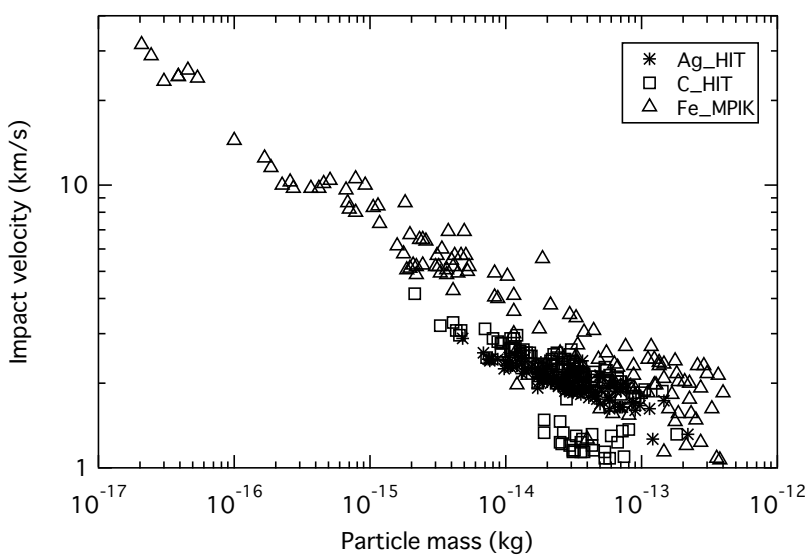

Fig. 3.9. Particle mass and impact velocity distribution of our experiments at both HIT and MPIK. Plots are results of the 20-μm-thick ALDN-S: silver particles at HIT (asterisk), carbon particles at HIT (open square), and iron particles (open triangle). Corresponding diameter ranges are 0.7–3.2 μm for silver particles (density: 10.5 g/cm^3), 1.7–6.1 μm for carbon particles (density: 1.9 g/cm^3), and 0.2–4.5 μm for iron particles (density: 7.9 g/cm^3).

3.5.2 Two-Stage Light Gas Gun

In order to accomplish acceleration of larger dust particles than those achievable by VdG, we first employed two LGG facilities, each of which belongs to the Institute of Space and Astronautical Science (ISAS) in Japan and the University of Kent at Canterbury (UKC) in U.K. (Burchell et al., 1999), respectively. As mentioned in Section 3.1, the schematic configuration of these LGG experiments is illustrated in Fig. 3.8. Both LGGs can shoot a single sub-mm projectile by means of a splitted sabot. The ISAS-LGG has a good track record of accelerating a single spherical projectile in down to 300-μm-diameter, made of soda-lime glass, while the UKC-LGG can accelerate a stainless steel particle in 800-μm-diameter as the smallest single projectile. At these experiments several different combinations of size, and velocity particles were tested. We only used the 20-μm-thick ALDN-S as a target because of a higher priority of larger areas of 20-μm-thick ALDN-S over smaller areas of 9-μm-thick ones.

Fig. 3.10 shows examples of the obtained signals from these LGG experiments. We found that for particles at the above size ranges in up to ~6 km/s, the LGG impacts generate saturated signals well beyond the saturation threshold of the ALADDIN, even with a relatively small impact of 300-μm-glass particle at several km/s. However, it qualitatively represents that larger impact magnitudes generate signals with higher amplitudes and longer pulse widths (i.e., decay time duration). In addition it clearly demonstrates that substantially large impacts could cause the multi-peaked features on their signal waveforms due to the ALADDIN's unique characteristics of signal processing described in Section 3.4. As the result, it is found that the single LGG particles are much larger than saturation threshold of the ALADDIN dynamic range in contrast to the VdG particles.

Obviously, unsaturated signals within its valid dynamic range are required in order to develop a calibration curve for the ALADDIN. Therefore, we adapted two more complimentary calibration methods: (1) the use of signals measured at the input terminal of the voltage amplifier within ALDN-E and (2) high energy irradiation experiments with a nsPL.

As for the method (1), Fig. 3.11 shows the signals simultaneously measured at the output and input terminals of the voltage amplifier within ALDN-E. We have found that unsaturated signals can be obtained at the input terminal even for large impacts by LGG. Considering the signal processing of the ALADDIN system described in Section 2.4, we regarded that all peaks of the

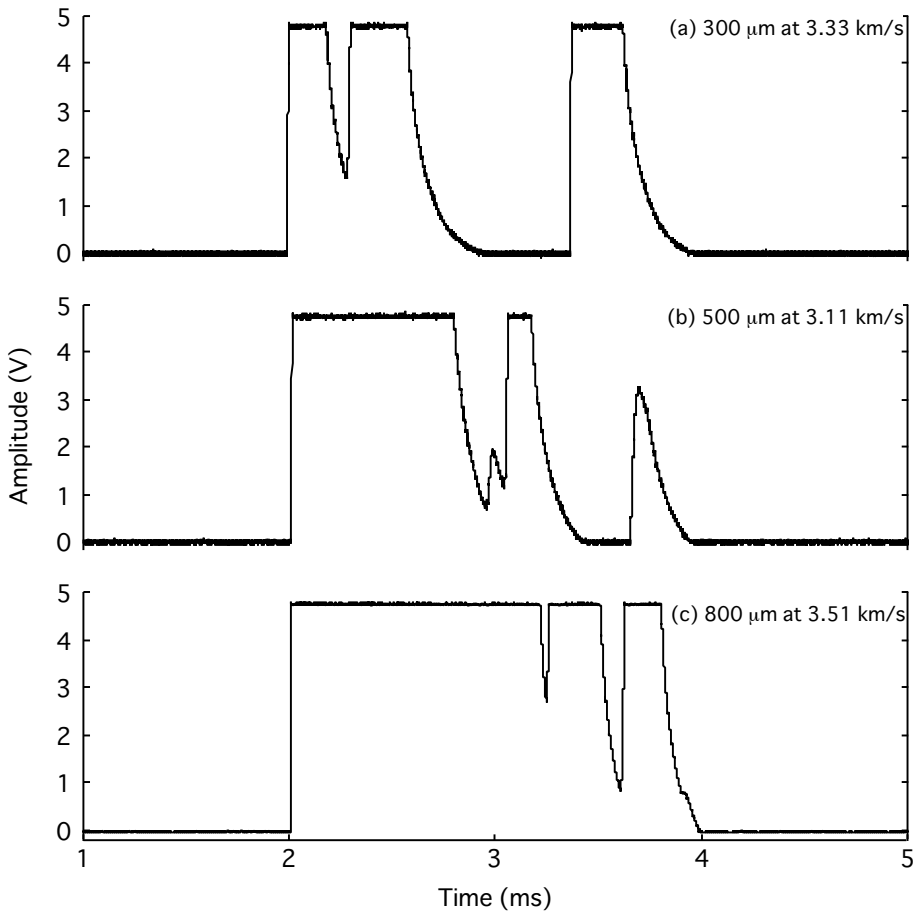

Fig. 3.10. Examples of signals obtained at the LGG experiments: (a) 300-μm glass at 3.33 km/s (130401-1), (b) 500-μm glass at 3.11 km/s (130329-1), and (c) 800-μm stainless steel, at 3.51 km/s (130124-1).

signal represent the magnitude of each impact. Therefore, we calculated time-integration of the input signals in order to sum up the contributions from all the peaks of the individual impact signal. Fig. 3.12 shows an example of such an integrated signal. Intensities after the removal of influence from the base voltage offset is defined as I_s, which has an arbitrary unit. Thus, from the LGG experiments we could obtain the signal parameter of the ALADDIN regarded as a function of impact conditions, such as particle mass and impact velocity. Impact conditions and results at the LGG experiments are summarized in Table 3.1. In addition to normal impacts on the target, we obtained three oblique impacts in order to investigate the angular dependence of the signal output.

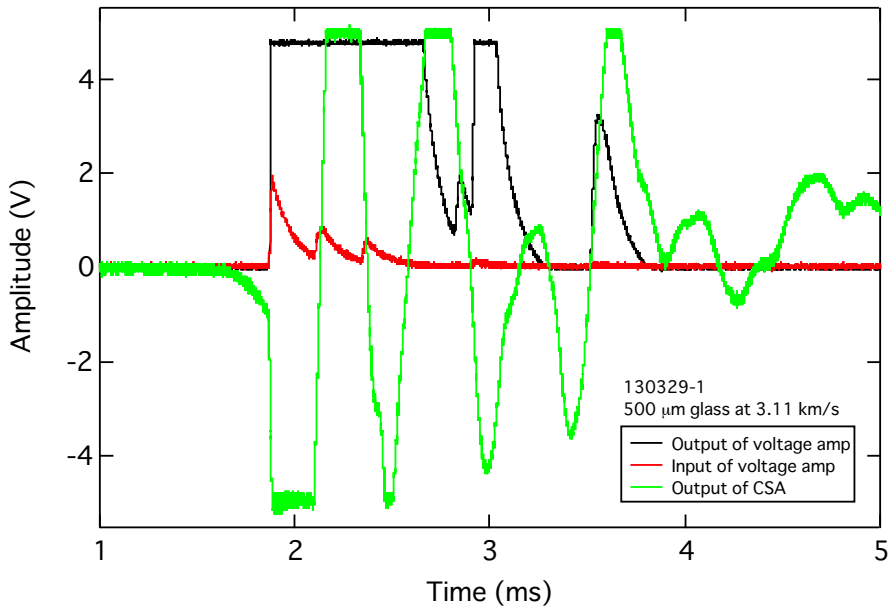

Fig. 3.11. Signals measured at output (black) and input (red) terminals of the voltage amplifier and output of the CSA (green) for the same impact in the LGG experiment. Multiple peaks of the input signal is corresponding to the saturated portion of the CSA output signal (see Section 3.4).

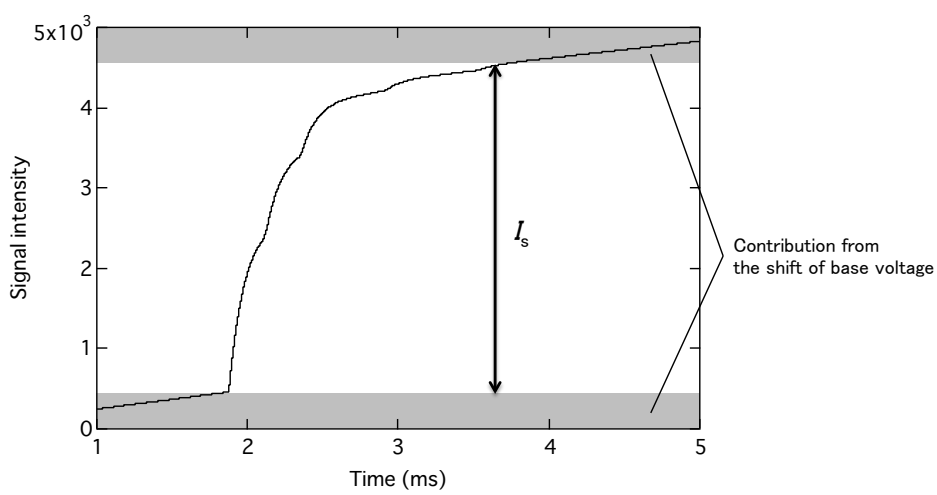

Fig. 3.12. The time-integrated input signal and definition of I_s. Shaded areas denote the contribution from base voltage offset. The unit of I_s is arbitrary.

Table 3.1. Impact conditions and results of signal acquisition at the LGG experiments: shot number (No.), particle material, particle mass (m), particle diameter (d), impact velocity (v), impact angle θ (deg), and the signal parameter of ALADDIN (I_s). The density of soda-lime glass and stainless steel particle used are 2.5 g/cm^3 and 7.8 g/cm^3, respectively. The impact angle, θ, is measured from the surface of the target.

No.	m (kg)	d (μm)	v (km/s)	θ	I_s[b]
Particle material: Soda-lime glass					
130329-1	1.64×10^{-7}	500	3.11	0	3880
130329-3	1.64×10^{-7}	500	6.77	0	11290
130329-6	1.64×10^{-7}	500	5.30	30	5450
130401-1	3.53×10^{-8}	300	3.33	0	1080
130401-2[a]	8.28×10^{-10}	100	5.14	0	390
131025-1	3.53×10^{-8}	300	3.19	0	780
131025-4	1.64×10^{-7}	500	3.04	0	4940
131025-5	1.64×10^{-7}	500	5.10	0	7460
131028-5[a]	8.28×10^{-10}	100	5.50	0	370
131029-1	1.64×10^{-7}	500	5.53	45	6950
Particle material: Stainless steel					
130123-1	2.08×10^{-6}	800	5.57	0	12500
130123-2	2.08×10^{-6}	800	5.60	0	6620
130123-3	2.08×10^{-6}	800	5.62	0	12000
130124-1	2.08×10^{-6}	800	3.51	0	7750
130124-3	2.08×10^{-6}	800	5.64	30	6350
130125-1	7.01×10^{-6}	1200	5.36	0	12530
130123-2	7.01×10^{-6}	1200	5.39	0	16500
130125-3	2.08×10^{-6}	800	7.63	0	14160

[a] These data were serendipitously obtained at a shot of 300-μm-glass projectile. At the shot the main projectile of 300-μm-glass sphere did not impact on the target because of failure of sabot separation. Instead a perforating hole with 100-μm diameter made by a fragment of glass projectile or nylon sabot. Therefore we introduced an uncertainty on its mass considering the difference of density between soda-lime glass (2.5 g/cm^3) and nylon (1.0 g/cm^3).

[b] The unit of I_s is arbitrary.

3.5.3 Nano-Second Pulsed Nd:YAG Laser Irradiation Experiment

As described in the previous section, we now can estimate the relation between I_s and their impact conditions from the LGG experiments. However, an unsaturated signal of the output of voltage amplifier is still required because data packets measured by the ALADDIN and received from the IKAROS telemetry on the ground does not contain the I_s values but the dV value ranging from 0.03421–5 V (see Section 2.3) only. In other words, the correlation between I_s and the output signal amplitude must be estimated with an appropriate method for simulating intermediate particle impacts, namely larger than that of VdG results and smaller than that of LGG results.

In order to solve this condition, we employed a nsPL at the Planetary Exploration Research Center (PERC) of Chiba Institute of Technology in Japan. Fig. 3.13 shows the schematic of the nsPL experiment and Table 3.2 lists technical properties of the instrument. At the experiment we irradiated infrared laser beam directly onto the 20-μm-thick PVDF target of ALADDIN flight spare and recorded their signals using the DSO in the same manner as the LGG experiments. The pulse energy was fixed at about 20 mJ for stabilization of the nsPL output. To adjust the actual irradiation energy on the target, we set glass slides on the beam line as energy absorbers (attenuation rate of each slide is ~13%) and altered the number of the absorber. The nsPL beam was focused on the target by a lens with a focal length of 85 mm to a focal point of about 1 mm in diameter. Irradiation timing was manually controlled and triggering of DSO was coincided with the nsPL shot by synchronized signal from the nsPL controller. We measured the pulse energy at the front of the target using a pyroelectric power sensor several times before and after each shot due to the lack of a beam splitter. The experiment was conducted in the atmosphere.

Here, we present applicability of the use of a nsPL for compensating intermediate signals generated between the VdG and the LGG impacts. Comparison of signals obtained at the LGG and the nsPL experiment is shown in Fig. 3.14. The amplitude of the LGG signal is slightly larger than that of the nsPL signal but the two signals show a good consistency in their waveforms.

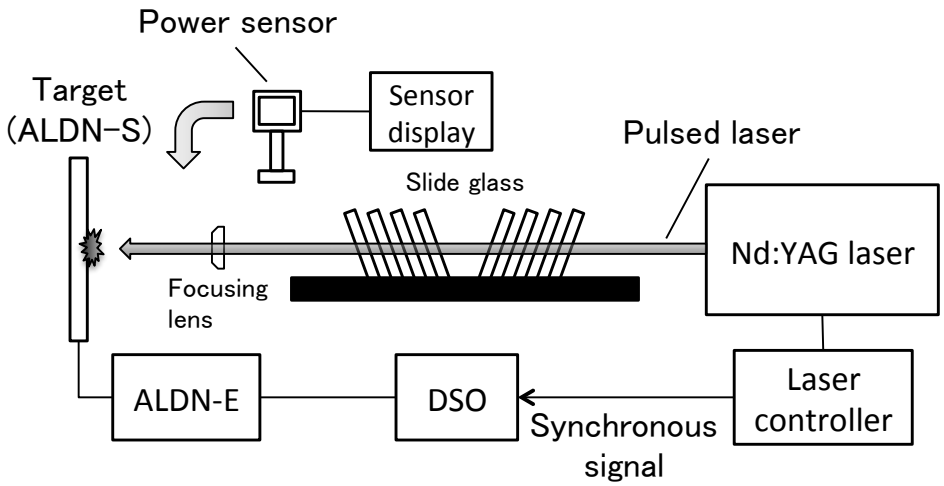

Fig. 3.13. Schematic of the nano-second pulsed Nd:YAG laser irradiation experiment.

Table 3.2. Specification of nsPL at the experiments. The pulse energy was adjusted by altering the number of energy absorber.

Pulse energy	15–20 mJ
Wavelength	1064 nm (IR)
Pulse width	7 ns
Pulse frequency	Singel pulse (manual)
Beam diameter	1 mm[a]

[a] The value is after focusing and averaged over the number of absorber.

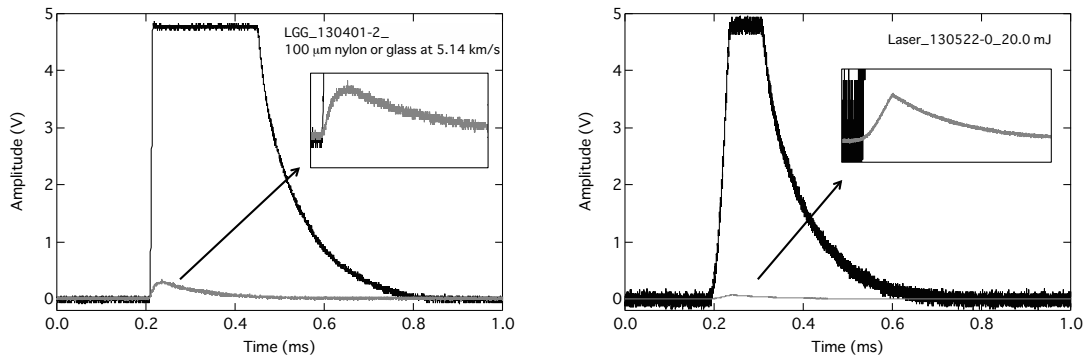

Fig. 3.14. Comparison of signals obtained at the LGG (left) and nsPL (right) experiments. The signals measured at the output (black) and input (gray) terminals of the voltage amplifier are displayed. Zoomed signals at input terminal are also displayed. This LGG signal generated the smallest I_s among our LGG experiments while the nsPL signal represents one of the largest case. The rise times of the LGG (~30 μs) and nsPL (~50 μs) are comparable.

Signal waveforms in question are determined by their rise times and fall times if their amplitudes are in the same level. First, the fall time is determined in principle by the time constant of the CR-RC shaper included in the ALDN-E analog circuit; thus there should be no difference between particle impacts and laser irradiation. Next, the rise time is thought to depend on not only characteristics of signal processing but also time scale of charge production. Physical phenomena of charge production between hypervelocity impacts of solid particles and laser excitation of target materials must be different, although a formation duration of micro-cratering/penetration and energy dissipation of nsPL irradiation should be in the similar time scale (Yamada et al., 1999). In fact, the rise times of the two methods were comparable each other in Fig. 3.14. Therefore, we consider in the ALADDIN calibration that the nsPL irradiation is a reasonable emulator for the waveform of a single-pulsed signal caused by a microparticle impact between the VdG and LGG mass-velocity ranges.

By adjusting a total number of absorbers, we obtained unsaturated output signals covering from 0.4 V to 4.8 V in peak voltage of signal, V. We also analyzed the input signals in the same manner as the LGG impact signals and then estimated I_s accordingly. The experimental conditions and results of the nsPL experiment are summarized in Table 3.3.

Table 3.3. Experimental conditions and results of the nsPL experiments: run number (No.), number of energy absorber (n), averaged laser energy (E_{avg}), deviation of the nsPL energy (E_{dev}), the signal parameter of ALADDIN (I_{s}), and peak amplitude of the output signal (V). E_{avg} and E_{dev} are calculated from several test shots before and after each irradiation to the target.

No.	n	E_{avg} (mJ)	E_{dev} (mJ)	I_{s}	V (V)
130522-1	0	19.96	0.351	442	6.3963[a]
130522-2	0	20.02	0.327	330	4.6796
130522-3	0	19.82	0.228	358	4.7726
130522-4	0	20.12	0.130	350	4.7680
130522-5	0	19.96	0.288	292	4.2246
130522-6	0	20.10	0.200	303	4.3552
130522-7	0	19.98	0.471	240	3.4802
130522-8	0	20.13	0.411	252	3.6302
130522-9	0	20.10	0.480	270	3.8865
130522-10	0	20.26	0.344	284	4.0740
130522-11	1	17.34	0.288	108	1.4944
130522-12	1	17.42	0.239	78	1.0865
130522-13	1	17.52	0.217	99	1.3595
130522-14	1	17.62	0.228	117	1.5910
130522-15	1	17.60	0.274	129	1.7938
130522-16	2	14.86	0.195	50	0.6091
130522-17	2	15.20	0.187	40	0.4580
130522-18	2	15.14	0.182	36	0.3850
130522-19	2	15.26	0.270	49	0.5975

[a] This was inferred from input signal amplitude by considering the gain of the voltage amplifier ($\times$ ~87.6).

3.6 ALADDIN Performance as an In-situ Dust Detector

Before starting the development of the calibration curve of the ALADDIN, we discussed the dynamic range of I_s corresponding to 0.03421–5 V in dV. As explained in Section 2.3, the actual observational information in the space data does not include I_s but dV (practically equivalent to V here). Therefore, we estimated the correlation between I_s and V by using the nsPL experiment data. Fig. 3.15 shows the I_s–V correlation. The fitting curve is given by

$$\log I_s = 0.145(\log V)^2 + 0.858 \log V + 1.87. \tag{3.1}$$

Noted that Eq. (3.1) is valid only when the impact magnitude is small enough, because much larger impacts generates multi-peaked signals at which peak voltages cannot be defined. For example, an impact of 100-μm nylon or glass particle at 5 km/s shows a single-peaked signal (see Fig. 3.14) while 500-μm glass-particle impact at 3 km/s generates a multi-peaked signal (see Fig. 3.11).

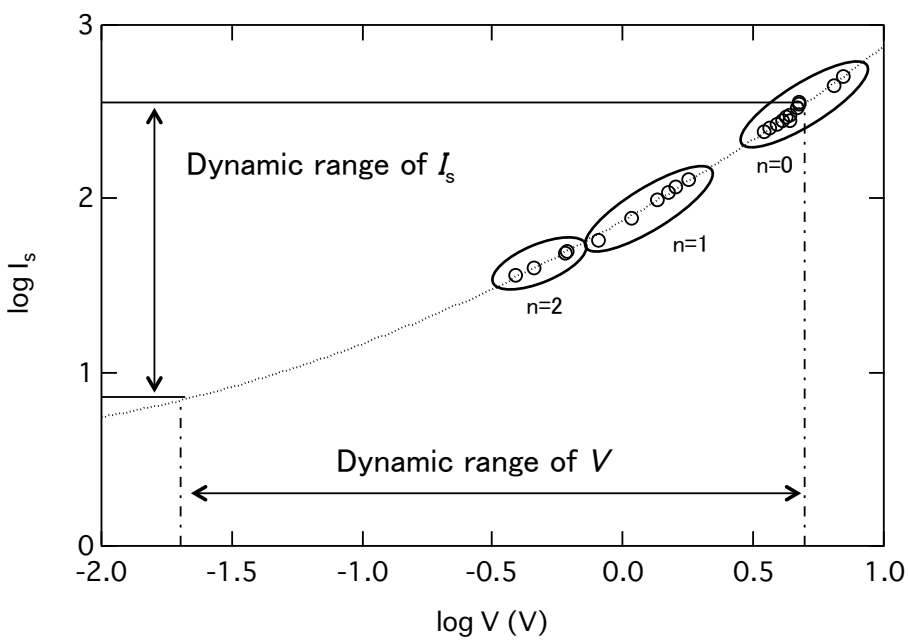

Fig. 3.15. The I_s–V correlation in logarithmic scales fitted by the second-order polynomial function. The dynamic range of V and the dynamic range of I_s are indicated.

3.6.1 Calibration Curve

Having noted the signal processing characteristics of the ALADDIN discussed in Section 2.4, we started with a traditional form to develop a calibration curve for the ALADDIN, i.e., a signal parameter of the detector is a function of particle mass and impact velocity (Simpson and Tuzzolino, 1985).

In addition, we introduced density of the impacting particle to the calibration in order to include the effect of penetration hole area on charge production from PVDF. Simpson et al. (1989) suggest that the charge produced by a particle penetration depends on the hole area. Poppe et al. (2010) also present a theoretical derivation of PVDF response to hypervelocity microparticle impacts based on crater dimension but focusing on non-penetrating impact. To make the initial analysis simple, we just assume that signal parameters of the detector are proportional to cross-sectional area of the impacting particle at the same mass and impact velocity. The cross-sectional area of a particle ($\propto r^2$ where r is radius of particle) can be expressed as $\rho^{-2/3}$ where ρ is density of particle, at a given mass.

Finally, we consider that the calibration law of the ALADDIN can be empirically formulated as

$$I_\mathrm{s} = a m^b v^c \rho^{-2/3} \tag{3.2}$$

where m and v are mass and impact velocity of an impacting particle, respectively, and a, b, and c are empirical coefficients.

We estimated the coefficient c independently, by using the results of the LGG experiments. The relations of I_s–v at the same mass and density (500-μm glass particles and 800-μm stainless steel particles) are shown in Fig. 3.16. We found a certain discrepancy of slopes between the curves from glass and stainless steel particles. Since the ALADDIN system cannot discriminate the composition of impacted dust particles, we adopt their averaged value of 0.952 as the coefficient c.

Then, we correlated $I_\mathrm{s} v^{-0.952} \rho^{2/3}$ and m of the LGG data and determined the remaining coefficient a and b by fitting to the LGG plot. Fig. 3.17 shows the $I_\mathrm{s} v^{-0.952} \rho^{2/3}$–$m$ correlation.

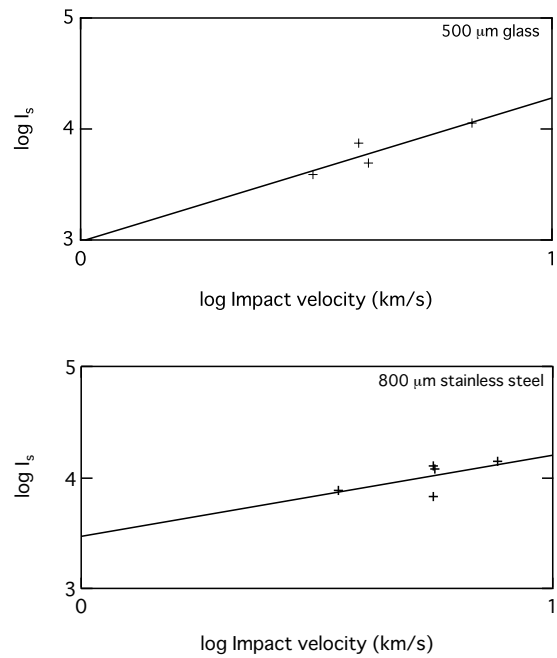

Fig. 3.16. The relation between I_s and v plotted in logarithmic scales: 500-μm glass particle (upper) and 800-μm stainless steel particle (bottom). The data plots were obtained at the LGG experiments. The slopes of calibration curves are 1.165 for glass particle and 0.741 for stainless steel particle, respectively.

Hence the calibration law for ALADDIN can be represented by using the signal parameter I_s, and impact conditions m (kg), v (km/s), and ρ (g/cm^3) as

$$I_s = 6.34 \times 10^6 m^{0.52} v^{0.952} \rho^{-2/3}. \tag{3.3}$$

The nsPL data has been extrapolated onto the calibration curve of Eq. (3.3) by calculating $I_s v^{-0.952} \rho^{2/3}$. The values of I_s are referred from Table 3.3, while for v and ρ we assumed 20 km/s as an average impact velocity at 1 AU (Grün et al., 1985), and 2.0 g/cm^3 as a representative bulk density of cosmic dust (Nesvorny et al., 2010). Under these assumptions of v and ρ, we found that the nsPL irradiation corresponds to 6.2×10^{-13} kg–1.0×10^{-10} kg in mass (8–46 μm in diameter).

Since the VdG particles did not generate any identifiable signals, the corresponding region of VdG particles is automatically determined only by the mass distribution at a given velocity (see Fig. 3.9) and Eq. (3.3) ($I_s v^{-0.952} \rho^{2/3} = 6.34 \times 10^6 m^{0.52}$). The striped area in Fig. 3.17

indicates the signal range of the VdG particles having about 20 km/s and 4.0×10^{-17} kg–1.0×10^{-16} kg referred from the mass-velocity distribution in Fig. 3.9.

A horizontal dashed-and-dotted line indicates $V = 1$ mV at 20 km/s and 7.9 g/cm^3 drawn by using Eq. (3.1), which means "detection threshold", a rough boundary of detectable or undetectable by the DSO at the ground experiments. Noted that this boundary can be varied in accordance with combined values of velocity and density of an impact particle; therefore the boundary lined in Fig. 3.17 is valid only for particles of 20 km/s in velocity and 7.9 g/cm^3 in bulk density. With this point above in mind, the developed calibration law reconfirms its consistency with the experimental results that no signal was observed at the VdG experiments.

The data of oblique impacts are also plotted in Fig. 3.17 and all those are included in the scattering of the normal impact data. For an isotropic flux of meteoroids, mean impact angle of incidence on a body is 45° and "shallow" impacts (e.g., less than 15°) have a probability of occurring of only 6.7% (Pierazzo and Melosh, 2000). Therefore, we conclude that the developed calibration law with the normal impacts data can be used without the consideration for angular dependence of the signal output.

Uncertainty in mass determination of the calibration law is about a factor of 2–6 as estimated from the prediction band of 1σ. We calculated which space impact data by the ALADDIN are generated by 10-μm-sized or larger ($m > 1.0 \times 10^{-12}$ kg at 2.0 g/cm^3) dust particles that are our primary scientific objective to reveal fine spatial-temporal structures of zodiacal cloud along the IKAROS trajectory. By considering this uncertainty, $\log(I_s v^{-0.952} \rho^{2/3}) > 0.85$ corresponds to $m > 1.0 \times 10^{-12}$ kg. From Eq. (3.1) we found that $V > \sim 1$ V is generated by impact of dust particles having $m > 1.0 \times 10^{-12}$ kg at 20 km/s.

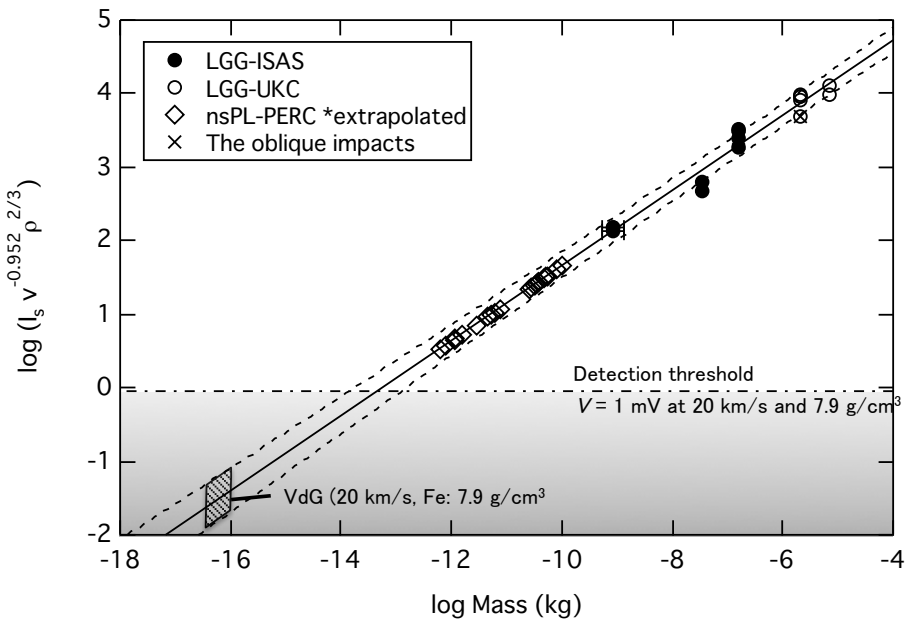

Fig. 3.17. Calibration curve of the ALADDIN. Plots denote the LGG data at ISAS (closed circle), the LGG data at UKC (open circle), the oblique impacts data (cross), and the nsPL data at PERC (open diamond). The error bar of the mass of "LGG-ISAS" denotes the uncertainty of its impactor material (see Table 3.1). The dashed-and-dotted line indicates a detection threshold line equivalent to V = 1 mV by a 7.9 g/cm^3-particle impact at the velocity of 20 km/s. The nsPL plots are determined by Eq. (3.3) under the assumptions that the dust impact velocity and density are 20 km/s and 2.0 g/cm^3, respectively.

3.6.2 Dynamic Mass-Velocity Range

From Eqs. (3.1) and (3.3) we estimated the dynamic mass-velocity range of the ALADDIN corresponding to the dynamic range of V. Fig. 3.18 is the mass-velocity diagram containing the detection and saturation thresholds of the ALADDIN, the impact conditions of the calibration experiments, the nsPL data converted to equivalent impacts by dust particles at 20 km/s, and the mass-velocity range on which we focus as primary scientific objective, corresponding to ≥10-μm-sized dust of impact velocity above 10 km/s. Consequently, the dynamic mass range of the ALADDIN system corresponds from 2.5×10^{-14} kg to 5.2×10^{-11} kg (3–37 μm in diameter at density of 2.0 g/cm^3) at the average impact velocity of 20 km/s around 1 AU (Grün et al., 1985). We found that the dynamic range of ALADDIN covers the intended mass-velocity range as our primary scientific objective.

We discuss here the validity of extrapolation from the LGG particle impact to several-micron particle impact. Simpson et al. (1989) reveals the clear difference in the coefficient of calibration curve for their PVDF-based dust detector between stopping and penetrating impacts on PVDF films. Although the signal processing of ALADDIN is different from theirs, the different mode of charge production Simpson et al. (1989) found should be considered for the calibration of our detector.

According to a micro-cratering study on PVDF films by Shu et al. (2013), impacts of a particle of 2 μm in diameter at 20 km/s velocity onto 52-μm-thick PVDF film result in a crater with 19-μm depth. We do not provide here comprehensive analysis of non-penetrating, micro-crater formation onto the ALADDIN-PVDF. However, it is possible to presume the validity of extrapolating from the LGG experiment results to at least 10-μm-diameter dust impacts which ensure complete penetration on the 20-μm-thick sensor of ALADDIN.

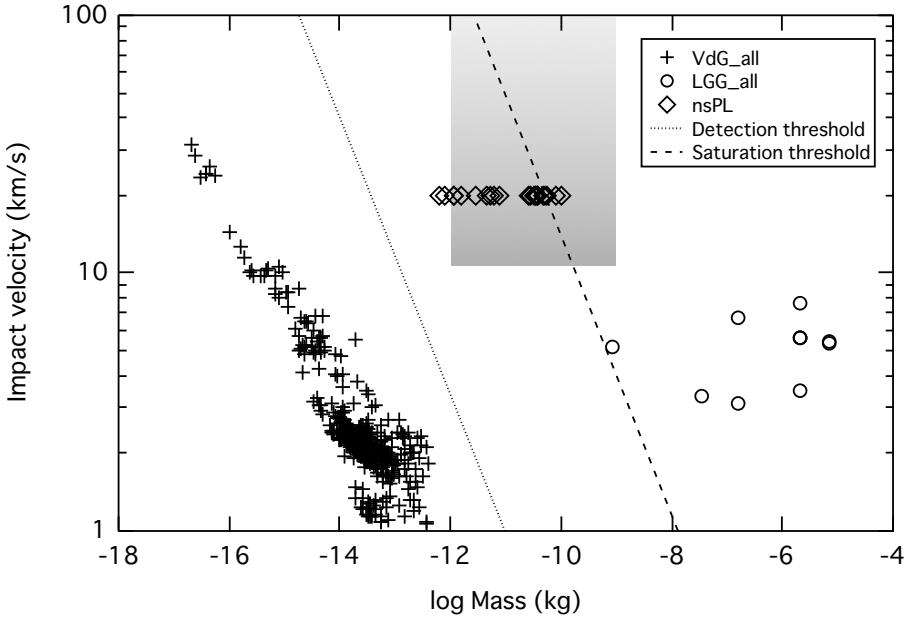

Fig. 3.18. Mass-velocity diagram composed of the results from all the VdG experiment (cross), all the LGG experiments (open circle) and the nsPL experiments (open diamond); the estimated dynamic range of the ALADDIN; and the range corresponding to our scientific objective. The mass of nsPL plots are taken from Fig. 3.17 under the assumption of impact velocity of 20 km/s. Detection threshold (V = 0.03421 V) and saturation threshold (V = 5 V) at 20 km/s and 2.0 g/cm^3 are indicated by dotted line and dashed line, respectively. Shaded area denotes the mass-velocity range corresponding to 10–100 μm sized dust of impact velocity above 10 km/s (see text).

Chapter 4

Noise Screening and Reduction of the ALADDIN Space Data

In this chapter, processes to screen noise events and to reduce the measured raw data by the ALADDIN to physical parameters of impacted dust particles are presented. We obtained 4356 raw data measured by the ALADDIN between 0.7 and 1.1 AU from July 2010 to October 2011 with a total observation period of ~300 days. The noise screening and data reduction processes are based on following 5 factors: 1) an operation history of the IKAROS spacecraft, 2) feature analysis of the measured raw data such as frequency of event occurrence, 3) results of laboratory impact calibration experiments with the ALADDIN flight spare (Section 3.5), 4) an effect of signal sampling probability attributed to the sampling rate of analog-to-digital converter (ADC) used for the ALADDIN electronics, and 5) estimate of thermal degradation of PVDF.

A flow chart for the noise screening and data reduction processes is shown in Fig. 4.1. According to the operation history of IKAROS and features of the measured raw data, we identified and removed false events caused by crosstalk noise and a malfunctioning channel. By analyzing the measured data after screening these noise events, we identified the actual dust-impacted sensor type (20-μm-thick "large" sensor or 9-μm-thick "small" sensor) and classified them by the signal amplitude level (dV), which is recorded in the measured data. At the laboratory calibration of ALADDIN, we verified correlation between the signal amplitude level and properties of dust particles, i.e., mass, impact velocity, and density (Hirai et al., 2014). From the results

of laboratory impact calibration tests, we can estimate the mass of impacted dust particles assuming typical impact velocity and material density of interplanetary dust. At the laboratory calibration tests, we only focused on the analog response of the ALADDIN electronics to hypervelocity microparticle impacts. However, in order to fully interpret the measured raw data by the ALADDIN, its digital characteristics, specifically the sampling rate of ADC, must be considered. Therefore, We investigated the probabilistic effect due to the signal sampling rate of the ALADDIN electronics. Furthermore, in order to assess an effect of thermal of PVDF on the sensor sensitivity, we obtained the laboratory calibration data of thermal-degraded PVDF sensors.

4.1 Noise Screening and Data Extraction for Scientific Discussion

4.1.1 Noise Screening

We found that the measured raw data from the ALADDIN includes false events caused by crosstalk noise coincided with operation of some specific instruments onboard IKAROS and malfunction of a particular channel of the ALADDIN. From the feature of measured data such as pattern of flagged channel and timing of event occurrence, we can identify and remove these false events.

The crosstalk noise events occurred when charge sensors for measuring membrane charge of IKAROS, Plasma Patch (PP) and Reaction Control System (RCS) were operated. Table 4.1 shows examples of the crosstalk noise events. The charge measurement by the PP were conducted on each petal of IKAROS in order. A feature of the PP crosstalk events is that the flagged channels are coincident with petals on which the charge measurement was conducted. On the other hand, the RCS crosstalk events occur at 30-second interval that corresponds to the time of thruster ejection.

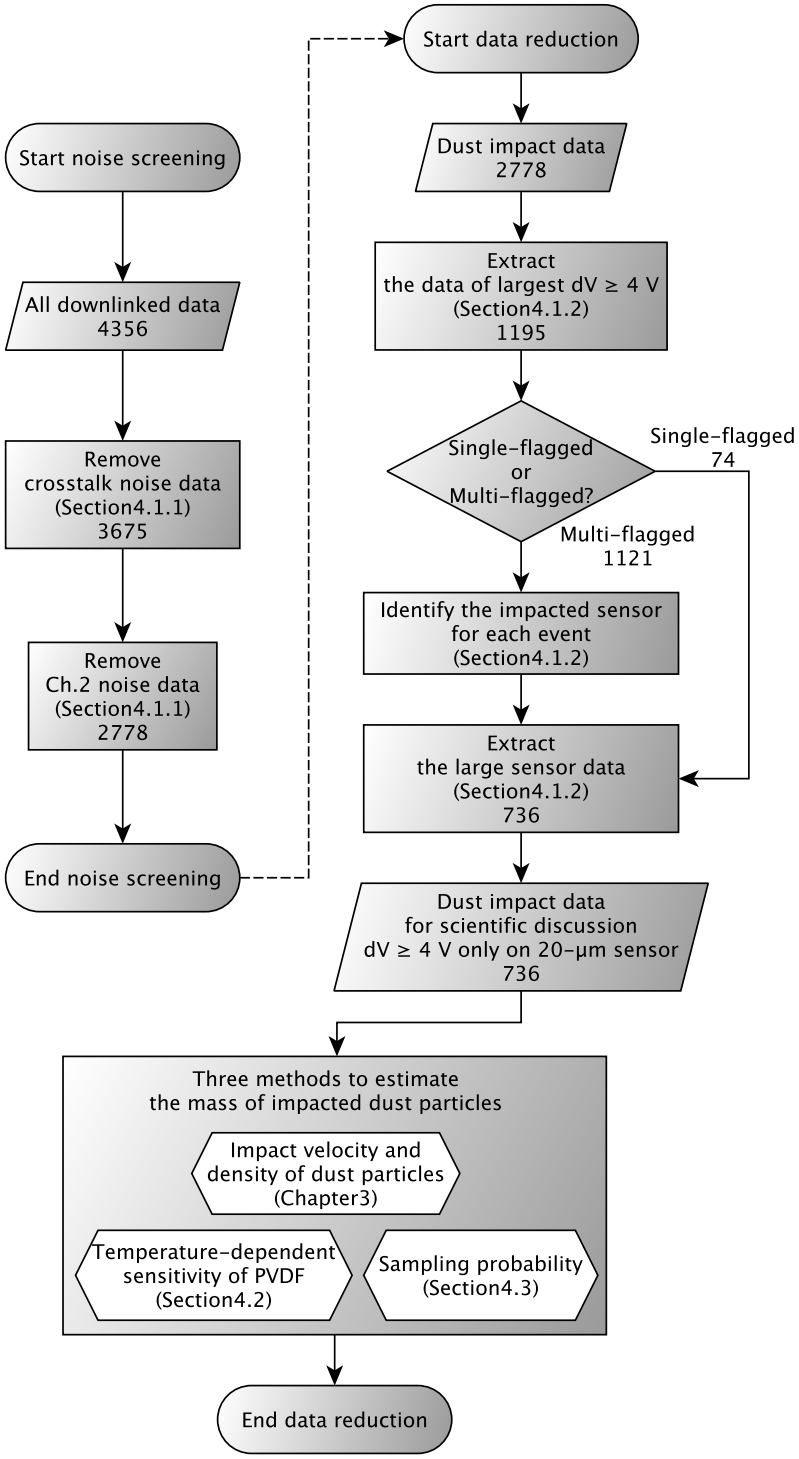

Fig. 4.1. Flow chart of the noise screening and data reduction process for the ALADDIN measurement data.

Table 4.1. Examples of crosstalk noise events. The odd-numbered channels are the large sensors (L) while the even-numbered are the small sensors (S). The values for each channel is dV (V). The time lag between the noise events of ALADDIN and the operation time of PP is about 1 minute that is just difference of their own internal clocks.

Event time (UTC)	Ch.1 (L)	Ch.2 (S)	Ch.3 (L)	Ch.4 (S)	Ch.5 (L)	Ch.6 (S)	Ch.7 (L)	Ch.8 (S)	Operation time of PP/RCS
In conjunction with the PP operation									
2010/07/05 7:17:32	4.92669	0.03421							2010/07/05 7:16:34
2010/07/05 7:17:47	0.2737	0.03421							2010/07/05 7:16:49
2010/07/05 7:19:35		0.03421	4.37928	0.30792					2010/07/05 7:18:38
2010/07/05 7:19:50			3.75367	0.03421					2010/07/05 7:18:53
2010/07/05 7:21:18					4.10068	0.34702			2010/07/05 7:20:21
2010/07/05 7:21:35					0.54741				2010/07/05 7:20:37
2010/07/05 7:23:36							0.62072	0.38612	2010/07/05 7:22:37
2010/07/05 7:23:54							4.10068	0.34702	2010/07/05 7:22:55
In conjunction with the RCS operation									
2010/11/12 0:32:57	4.84848	0.4741							Gas ejection every 30 sec[a]
2010/11/12 0:33:28	4.84848	4.84848							
2010/11/12 0:33:58	4.84848	1.24633							
2010/11/12 0:34:28	0.43011	0.1173							
2010/11/12 0:34:58	4.84848	1.95015							
2010/11/12 0:35:28	4.84848	2.34604							
2010/11/12 0:35:58	4.84848	0.93842	0.03421		0.03421				
2010/11/12 0:36:28	0.07331	3.87097							

[a] RCS was nominally operated by programmed sequential command so that the specific time information of each gas ejection is not provided. About 30-second thrust was preset for the each gas ejection at the time.

The specific cause of these crosstalk noise has not been confirmed by laboratory simulations, but we suspect that unstable electric connections between the IKAROS system (SAIL-I/F) and the ALADDIN occurred after the launch of spacecraft. At the spacecraft integration test on the ground, there were no crosstalk noise between these instruments and the ALADDIN. The PP is also connected to the SAIL-I/F along with ALADDIN, so the failure in the ALADDIN-IKAROS connection may likely pick up some interferences from the PP operation. We confirmed the generation of event data from ALADDIN with the RCS "no-gas" operation, which indicates that the RCS crosstalk is not caused by gas blowing on ALDN-S but by electrical problem between the RCS and the ALADDIN. Whatever the cause is, these noise events are not used for scientific discussions and we have dealt with them by temporary suspending of the ALADDIN operation during the PP and RCS operation.

Malfunction of a particular channel, specifically Ch.2, was identified by the dt information and occurrence frequency. Table 4.2 lists the examples of noise events due to malfunctioning Ch.2. Most of the dV were 0.03421, which is the minimum value of dV while dt shows error values, 0 or 769. Furthermore, the occurrence frequency sometimes becomes exceedingly higher than any other channel. According to these features, it seems that the single event of Ch.2 is caused by fluctuation of base voltage. We suspect that the mechanical connection of Ch.2 sensor on the IKAROS membrane might have become unstable at the deployment of membrane and it caused such noise event on the Ch.2. Therefore, we regard the Ch.2 as an invalid sensor and remove the sensor area, 0.01 m^2, from total sensor area of the ALADDIN.

Table 4.2. Examples of noise events due to the malfunctioning Ch.2 noises.

Event time (UTC)	dV (V)	dt
2010/07/26 2:45:53	0.03421	0
2010/07/31 9:04:22	0.05865	0
2010/08/04 7:11:36	0.03421	769
2010/08/07 2:32:55	0.03421	0
2010/08/07 20:38:16	0.3421	0

4.1.2 Data Extraction for Scientific Discussion

After removing noise events from all downlinked 4356 data, there remain 2778 data as candidates of dust impact events. Among these dust candidate data, single channel should be flagged because the probability of simultaneous impacts of multiple dust particles is infinitely small in the interplanetary space. Nevertheless, about 70% of the dust candidate data show "multi-flagged" feature. First 10 multi-flagged events obtained in space are listed in Table 4.3. Note that the dt values of the flagged channels were almost "9" and partly the error value "0" or "769". The combination of channels seem to be random except for small numbers of flagged Ch.6 and Ch.8.

In order to confirm repeatability of the multi-flagged events, we conducted laboratory impact experiments. It is difficult to prepare the full set of the ALDN-S flight-spares and reproduce the in-flight configuration on the deployed solar sail in the vacuum chamber of the LGGs. Therefore, we only used flight spare of the large (20-μm thick) and the small (9-μm thick) ALDN-S for only the impact target sensor and employed a 10 cm × 10 cm PVDF sensor piece for the simplified, alternative dummy sensor. The target sensor was connected to Ch.1 of ALDN-E while the dummy sensor to Ch.2. The projectile material used were soda-lime glass and tungsten carbide. The diameter of projectiles was 300 μm. The projectiles were impacted on the target sensor as single shot at 2–6 km/s accelerated by the LGG of ISAS. The obtained 6 data are shown in Table 4.4. We observed only one multi-flagged event (101020-1) among the 6 data. In 101020-1, dV of Ch.1 shows two orders larger value compared to that of Ch.2 and the signals were sampled three times on Ch.1 (dt = 27) and once on Ch.2 (dt = 9).

Table 4.3. First 10 multi-flagged events obtained in space. The odd-numbered channels are the large sensors (L) while the even-numbered are the small sensors (S). The values are dV (V) of each channel.

Event time (UTC)	Ch.1 (L)	Ch.2 (S)	Ch.3 (L)	Ch.4 (S)	Ch.5 (L)	Ch.6 (S)	Ch.7 (L)	Ch.8 (S)
2010/06/30 14:35:12		0.03421	4.37928		1.36852		0.07331	
2010/06/30 15:37:00	4.92669	0.03421	0.38123	0.07331				
2010/06/30 18:51:04	0.46921	4.38416	0.77713	4.84848	0.03421		0.07331	
2010/07/03 4:49:11	4.92669	1.55425	4.96579	1.55914			0.38612	
2010/07/03 17:44:24			1.79863	4.84848			0.07331	
2010/07/04 10:44:05		0.03421	0.1173					
2010/07/04 22:20:24	4.92669	0.03421	0.2346					
2010/07/05 2:12:52	2.34604	0.38612	1.17302	1.57869	0.46921		1.23167	3.16227
2010/07/05 15:15:12	1.59824	0.07331	1.95015	0.30792	0.93842		0.69892	0.07331
2010/07/05 18:06:01	4.92669		4.06158	0.54741	1.95015		0.93842	

Table 4.4. Event data obtained at the laboratory impact experiment aimed at reproducing the multi-flagged event. WC is tungsten carbide. The values for each channel correspond to dV/dt.

No.	Target sensor	Projectile material	Projectile mass (kg)	Impact velocity (km/s)	Ch.1	Ch.2
101018-3	20 μm	WC	2.38×10^{-7}	5.89	4.84848/18	
101019-3	9 μm	WC	2.38×10^{-7}	2.70	4.84848/27	
101019-4	9 μm	WC	2.38×10^{-7}	2.76	4.84848/18	
101019-5	9 μm	Glass	3.53×10^{-8}	1.90	0.2346/9	
101019-6	9 μm	Glass	3.53×10^{-8}	1.90	4.84848/18	
101020-1	9 μm	Glass	3.53×10^{-8}	1.93	4.84848/27	0.07331/9

Comparing between Table 4.3 and Table 4.4, we found that the multi-flagged events at the laboratory experiment occur with a remarkably low frequency, on contrary to in space (70% in space while 17% at the laboratory). However, according to the only example of multi-flagged event at the laboratory experiment (101020-1 in Table 4.4), we may be able to consider a channel that generates the maximum dV among the other channels as the impacted channel. On the other hand, dt of the laboratory experiment were relatively large compared to typical value of the space data ("9"). The reason of this is considered due to that the projectiles at the LGG experiment are significantly larger than dust particles detected by the ALADDINin space, hence signal decay time at the laboratory experiment becomes longer.

Consequently, the laboratory experiment does not reproduce the situation in space too well. We also did not observe multi-flagged events at the pre-launch operation tests, so the cause of such events should be happened in space. Recalling the crosstalk noise with the operation of some instruments on IKAROS and malfunction of Ch.2 (see Section 4.1.1), the root of these troubles may be common and something related to electrical circuit/ground problem between the ALADDIN and IKAROS system.

Based on the identification method of impacted channel for the multi-flagged events, we extracted specific data from the 2778 dust candidate data for further scientific discussion about cosmic dust. Fig. 4.2 is a tree diagram of the data extraction. With several criteria explained below, each event are sorted into impact data on the large sensors or the small sensors.

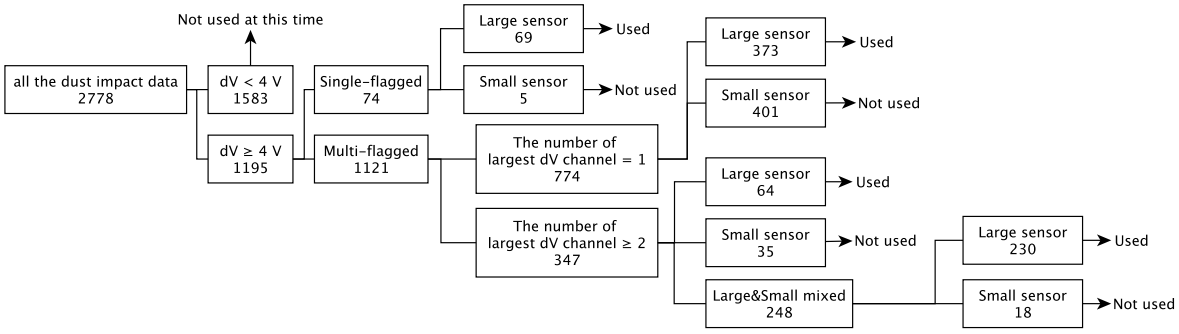

Fig. 4.2. The tree diagram for extracting the dust impact data for further scientific discussion.

As will be explained in Section 4.3 and this section, we only used the data of dV ≥ 4 V on the large sensors for further scientific discussion at present. With the criterion of dV ≥ 4 V, 74 single-flagged data and 1121 multi-flagged data were obtained from the 2778 dust candidate

data. The single-flagged data can be easily divided into each sensor type (large or small).

As for the multi-flagged data, sorting process is different depending on the number and combination of maximum dV channels. First, in case of only one maximum dV channel, this type of multi-flagged data can be sorted into each sensor type in the same manner as the single-flagged data. 774 data are categorized as this data type and divided into 376 data on the large sensors and 398 data on the small sensors. Next, even in case there are more than two channels having the same maximum dV values (347 data), the identification of impacted sensor type is straightforward if the combination of those channels is only on large sensor channels or only on small sensor channels. We found 64 data for only large sensors and 35 data for only small sensors, respectively. Finally, if the data has a combination of more than two large and small sensor channels that show the same maximum dV values, we cannot distinguish at present on which sensor the dust particle actually impacted. We counted 248 of such data. Nevertheless, we could estimate the number ratio between the large sensor data and the small sensor data according to the ratio of sensor area and detection sensitivity between each sensor type.

The large/small sensor area ratio is 12.5:1 (see Section 3.2). We have lacked impact calibration data for the small sensors due to restriction of experiment opportunities. Therefore, we refer to experiment results of Tuzzolino et al. (2003) in which they showed the detection sensitivities of PVDF dust sensors that have similar ratio of sensor area and thickness.

They conducted impact calibration experiments with their sensor configuration which consists of a large sensor (28-μm-thick and 200 cm^2) and a small sensor (6-μm-thick and 20 cm^2), using a plasma drag dust accelerator. The results show that the sensitivities of both type of sensors are nearly the same when the impacted dust particle penetrates the PVDF sensor instead of stopping in the target, i.e., cratering (see their Fig. 9). In our case, we have confirmed that the data of dV $\geq$ 4 V are generated by penetration impacts (Hirai et al., 2014). Therefore, we regard that the detection sensitivities of our large sensors and small sensors beyond their respective threshold levels are almost the same. According to the sensor area ratio, we can divide a total of 248 data into 230 for the large sensors and 18 for the small sensors, respectively.

Thus, the 1195 dust candidate data showing dV $\geq$ 4 V are divided into 736 data on the large sensors and 459 data on the small sensors. If the impacted-sensor identification method demonstrated above is valid, the data number ratio between each sensor should be nearly equiv-

alent to the sensor-area ratio (12.5:1). However, the obtained ratio is far from the sensor-area ratio. Since the large sensors have not represented any malfunctioning signs like Ch.2 (see Section 4.1.1), we presume that there are still some amount of noise data on the small sensors.

Fig. 4.3 shows the event number on each small sensor that have single channel of the maximum dV including single-flagged data. Since Ch.2 is the malfunctioning channel, we neglect it here. Ch.4 and Ch.8 show significantly larger number compared to Ch.6.

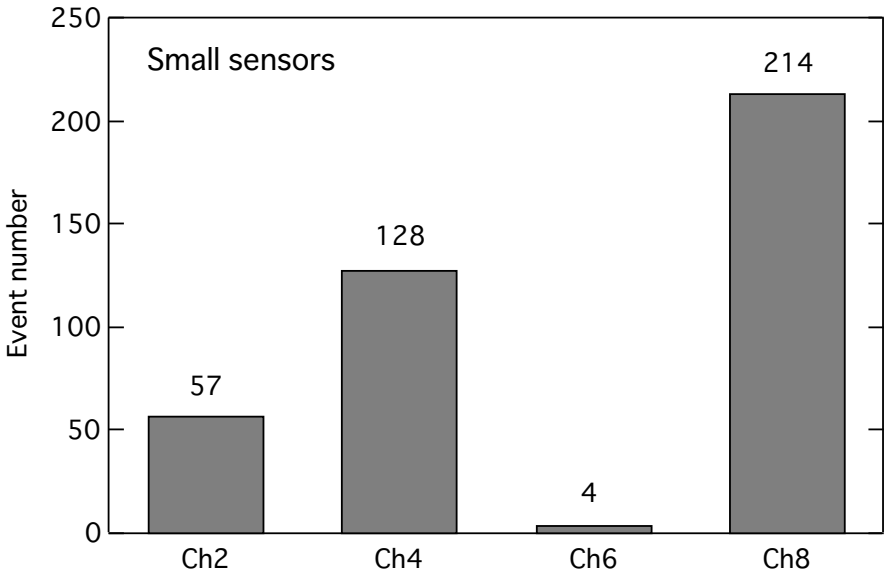

Fig. 4.3. Event number on each small sensor that have single channel of the maximum dV including single-flagged data. The detection numbers of each channel are denoted on each bar.

Table 4.5. Event number ratio between the large sensor data and the small sensor data at three measurement terms: the whole term, before IKAROS's Venus closest approach (VCA) (UTC2010/12/9), and well before VCA (UTC2010/11/1).

Sensor type	The whole term	Before VCA	Well before VCA
Large sensor	736 (1.6)	283 (7.6)	124 (8.3)
Small sensor	459 (1)	37 (1)	15 (1)

Fig. 4.4 denotes the event rate of Ch.4 and Ch.8 along the heliocentric distance. Impact rate for a given dust detector at the same heliocentric distance is thought to be the same order due to azimuthal smoothness of the zodiacal cloud. However, the event rates of Ch.4 and Ch.8 continue to increase over time, which any other channel has not represented. Moreover, as will be

explained in Section 4.2, the detection number should decrease after perihelion passage at about 0.7 AU due to thermal degradation of PVDF sensor's sensitivity. These facts suggest that Ch.4 and Ch.8 have become "noisy" such as Ch.2 probably due to exposure to high temperature. We have suspected that there might happen some problem of sensor part, e.g., unstable connection between the sensor terminal and the cable due to thermal deformation or something like that.

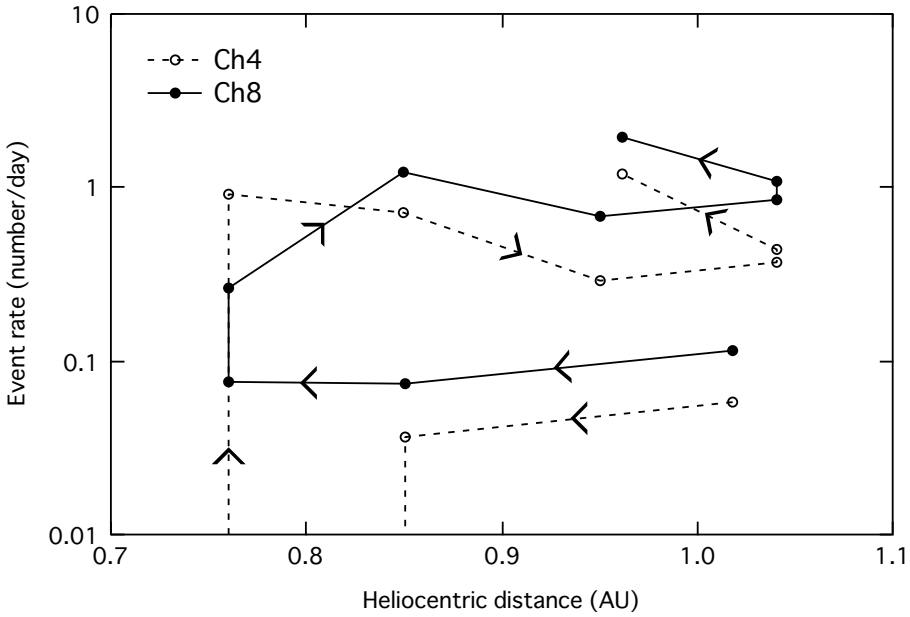

Fig. 4.4. The event rate of Ch.4 and Ch.8 along the heliocentric distance between 0.72 AU and 1.1 AU. Each point is plotted per about 0.1 AU. The start of the measurement corresponds to the lower right point.The rate of Ch.4 at the first 0.72-0.8 AU bin dropped to 0.

In order to eliminate these noise data on the small sensors, we estimated the event number ratio between the large sensors and the small sensors in following two terms: before IKAROS's Venus closest approach (VCA) (UTC2010/12/9, at 0.72 AU) and well before VCA (UTC2010/11/1, at 0.78 AU). Table 4.5 contains the event number ratio at the added two terms and the whole measurement term. The event number ratio well before VCA is nearer to the ratio of large/small sensor area (12.5:1) than that of the whole term, but there is still a bit difference. This might suggest either the small sensors have generated noise data from the beginning of measurement or the detection sensitivity of the small sensors is higher than that of the large sensors unlike the experiment results from Tuzzolino et al. (2003). In either case, our method for identification of impacted sensor seems to be plausible.

Another data analysis seems to support the method for impacted-sensor identification. Fig. 4.5

shows dV histogram of the single-flagged (filled black bar) and the multi-flagged (unfilled red bar) data on the large sensors. Note that these multi-flagged data have single channel of the maximum dV. We can clearly see different distributions between the single-flagged data and the multi-flagged data; the single-flagged data are dominated by low dV values while the multi-flagged data by high dV values. If the multi-flagged events are caused by large charge current on an impacted channel which may interfere with the other not-impacted channels, the difference in dV distributions between the single-flagged data and multi-flagged data can be explained as follow; the single-flagged data implies smaller and more abundant dust impacts, while the multi-flagged data do larger and less frequent dust impacts. The multi-flagged, low dV data are found with a certain amount. We think that these type of data could be caused by fluctuation of the base voltage, which is common to all the channels, since low dV means low signal-to-noise ratio. Note that the signals showing low dV values are suffered from miss-detection due to sampling probability explained in the next section, so impacts of small dust particles should actually occur with higher frequency.

Consequently, based on the method for impacted-sensor identification, the 736 data on the large sensors can be used for further scientific discussion about interplanetary dust. However, as for the large and small mixed 248 data (230 data for the large sensor and 18 data for the small sensor), we cannot distinguish between large and small against individual data. Therefore, we consider 754 data as data on the large sensors, including the indistinguishable 18 data for the small sensor.

4.2 Thermal Degradation of PVDF

Piezoelectric and ferroelectric sensitivities, i.e. dust detection sensitivity, of PVDF are known to be varied depending on its material temperature (e.g., James et al., 2010). Furthermore, exposure to a certain level of high temperature causes irreversible degradation of the sensitivity due to disarray of molecular dipole structure in PVDF. We conducted aging heat treatment at 100°C for the flight-model of ALDN-S before its launch in order to mitigate the variation of sensitivity due to temperature change in flight.

Fig. 4.6 shows the temperature history of ALDN-S and a component on the IKAROS mem-

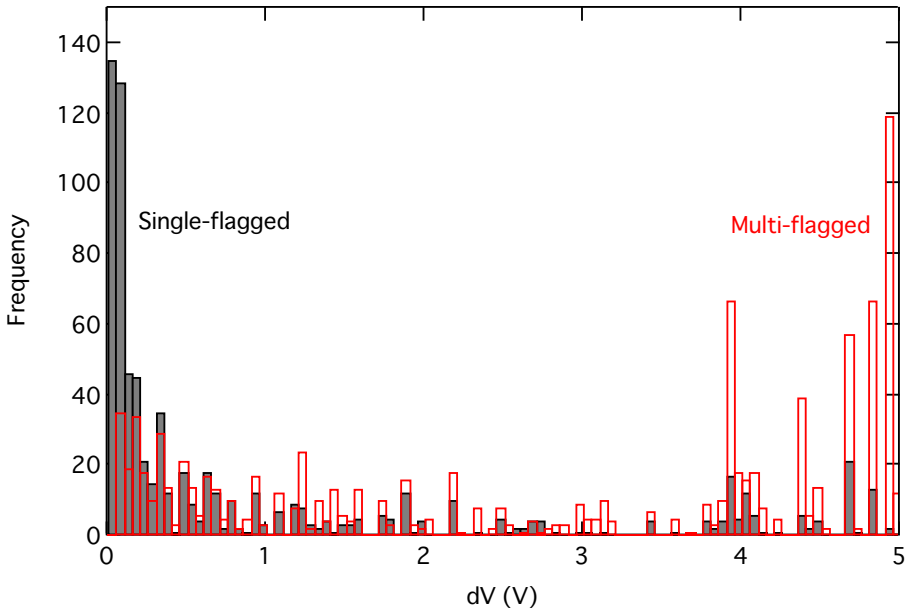

Fig. 4.5. dV histogram of the large sensors. As for the single-flagged (filled black bar) and the multi-flagged (unfilled red bar) data, maximum dV are shown. These multi-flagged data have single channel of the maximum dV.

brane (MEMB2), which has similar emissivity and absorption coefficient and is attached on the same side of IKAROS membrane as ALDN-S, along the first inbound orbit between 0.72 and 1.1 AU of heliocentric distance. Thermometer for ALDN-S (MEMB4) has been failed since about 4 months after the launch, so we refer to MEMB2 at 0.7 AU and 0.8 AU and estimate the ALDN-S temperature by considering the offset from MEMB2. It is found that ALDN-S has experienced temperature from 80 to ~180°C during its orbit around the Sun.

In order to evaluate the thermal degradation of PVDF, we performed LGG impact experiment using the flight-spare of 20-μm-thick ALDN-S heated at 156°C. Experimental condition and results are listed in Table 4.6. For comparison with the sensitivity of aging 100°C-heated sensor, we analyzed the output signals and derived I_s in the same manner as described in Chapter 3.

Fig. 4.7 depicts three types of the calibration curves for and two types of the LGG experiment data. Horizontal line denotes the level of $I_s v^{-1.06} \rho^{2/3}$ calculated from V = 4 V, impact velocity of 20 km/s, and material density of 2.0 g/cm^3. The calibration curves are for 100°C-, 156°C-, 180°C-heated sensor. Two dashed line denotes the 95% confidence band of the 100°C calibration curve. The experimental data points of the 100°C-heated sensor listed in Table 3.1

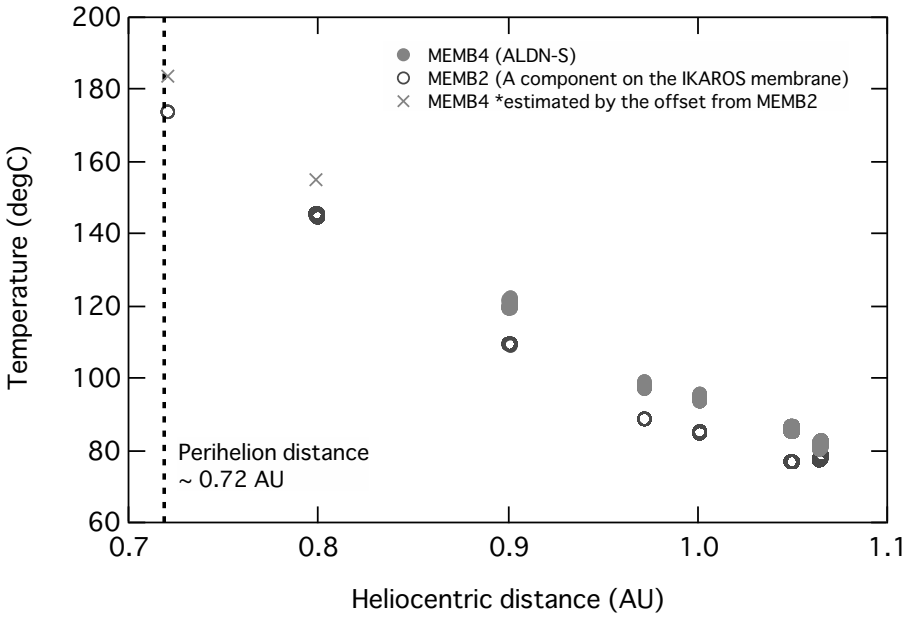

Fig. 4.6. The temperature of ALDN-S (MEMB4) and a component on the IKAROS membrane (MEMB2) along the first inbound orbit between 0.72 and 1.1 AU of heliocentric distance. Fluctuation of temperature was up to several degree.

Table 4.6. Experimental condition and results of the impact experiment with LGG for investigating the sensitivity of 156°C-heated 20-μm-thick ALDN-S. The material of projectile is soda-lime glass. I_s is arbitrary unit.

No.	Projectile mass (kg)	Impact velocity (km/s)	I_s
101028-1	1.64×10^{-7}	3.37	500
101028-2	1.64×10^{-7}	5.48	1950
101028-4	3.53×10^{-8}	3.18	1000

and the 156°C-heated sensor listed in Table 4.6 are also plotted. The calibration curve of 156°C-heated sensor passes through the averaged point of the three experimental data of the 156°C-heated sensor, which is obtained by assuming the same slope of the 100°C calibration curve. Vertical offset between the calibration curves of 100°C and 156°C is 0.485.

By considering the sensor temperature, T (°C), dependence of this offset, we can obtain the calibration curve of the 180°C-heated sensor which may be the highest temperature ALDN-S experienced. Also, the correlation between the offset and T is required to find out continuous decay of the sensor sensitivity during the IKAROS's first inbound orbit from 1.1 AU to 0.72 AU. By simply assuming that the offset expands linearly with increasing in T, the offset can be

represented as $8.66 \times 10^{-3}T - 0.866$. After the fist perihelion passage at 0.72 AU, the detection sensitivity is fixed at $T = \sim 180°$C due to irreversibility of PVDF degradation.

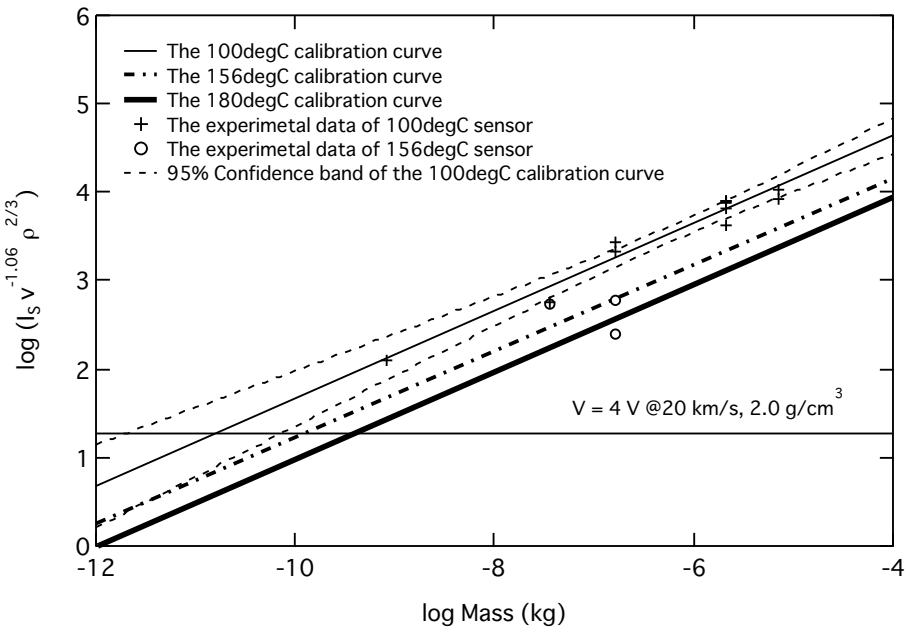

Fig. 4.7. The calibration curves for the 100°C-, 156°C-, and 180°C-heated sensor. The experimental data points of the 100°C- and 156°C-heated sensor are also plotted. The dashed lines denotes 95% confidence band of the 100°C calibration curve. The calibration curve of 180°C-heated sensor was obtained by the vertical offset of calibration curve estimated by the 100°C- and 156°C curve, $8.66 \times 10^{-3}T - 0.866$.

Consequently, the equation of ALADDIN calibration curve including the T effect is formulated as

$$\begin{aligned} &0.145(\log V)^2 + 0.858 \log V + 1.87 \\ &= \log(4.08 \times 10^6) - (8.66 \times 10^{-3}T - 0.866) + 0.49 \log m + 1.06 \log v - 2/3 \log \rho. \end{aligned} \tag{4.1}$$

Note that the confidence levels of these calibration curve at $V = 4$ V are quite ambiguous due to a lack of the impact experiment data with 10's-μm-sized projectiles ($m = 10^{-12}$–10^{-9} kg). Furthermore, the slopes of these calibration curves for different temperature are not necessarily the same. Therefore, it is possible that the detection size of the 180°C sensor, which generates $V = 4$ V at $v = 20$ km/s and $\rho = 2.0$ g/cm^3, is smaller than the estimated value, ~67 μm. Eberle and Eisenmenger (1992) reported that a PVDF sensor heated at 180°C recovers its piezoelectric sensitivity to the level of 100°C-heated sensor. As a conclusion, we regards the

detection sensitivity of the 180°C sensor may be open to discuss.

4.3 Sampling Probability

The measurement information of ALADDIN, dV and dt, are obtained by the signal sampling of the ADC inside ALDN-E. The sampling interval, i.e. 600 μs, is somewhat slow for the signals ALADDIN generates. Fig. 4.8 shows an example of signal waveform observed at the LGG experiments. Since the pulse duration is a few milliseconds at the longest, it is difficult for this ADC speed to accurately reproduce the signal wave form. Therefore, in order to estimate the physical properties of impacted dust particles from dV, the signal sampling effect should be considered.

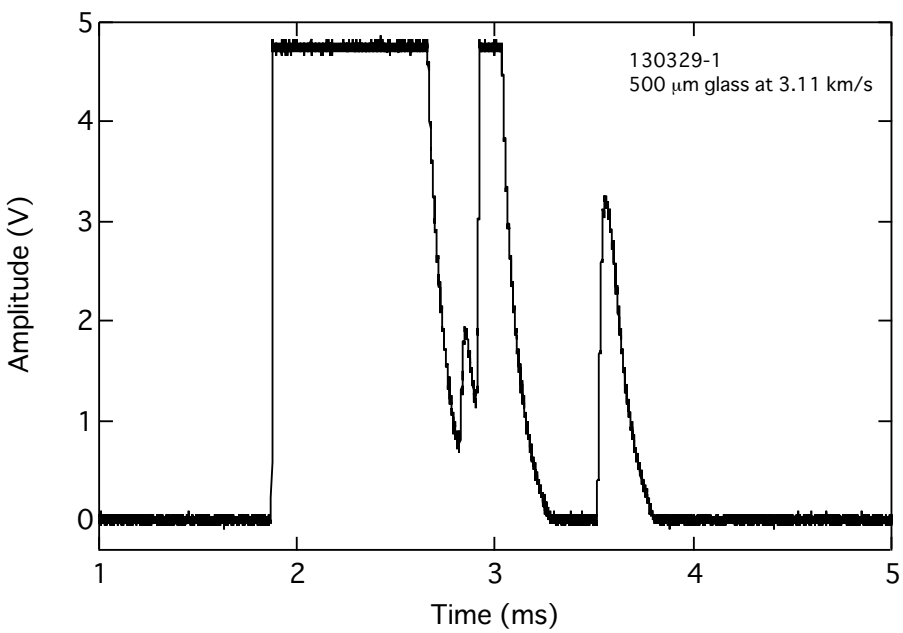

Fig. 4.8. An example of signal waveform obtained at the LGG experiments. The projectile of 500-μm-diameter glass particle was impacted on the flight-spare of 20-μm-thick ALDN-S at 3.11 km/s.

The coarse sampling rate triggers miss-detection against the signals with pulse width of <600 μs. Fig. 4.9 represents the relation between V (the peak voltage of signal defined in Section 3.5) and detection probability by using some of the nsPL experiment data. The detection probability can be calculated by dividing the pulse width of signals by the sampling interval (600 μs). At $V < 1$ V, the half of signals are miss-detected, while nearly 90% of signals can

be detected at about 5 V. Significant large signals, e.g. obtained at the LGG impact experiment (Fig. 4.8), is detected with 100%.

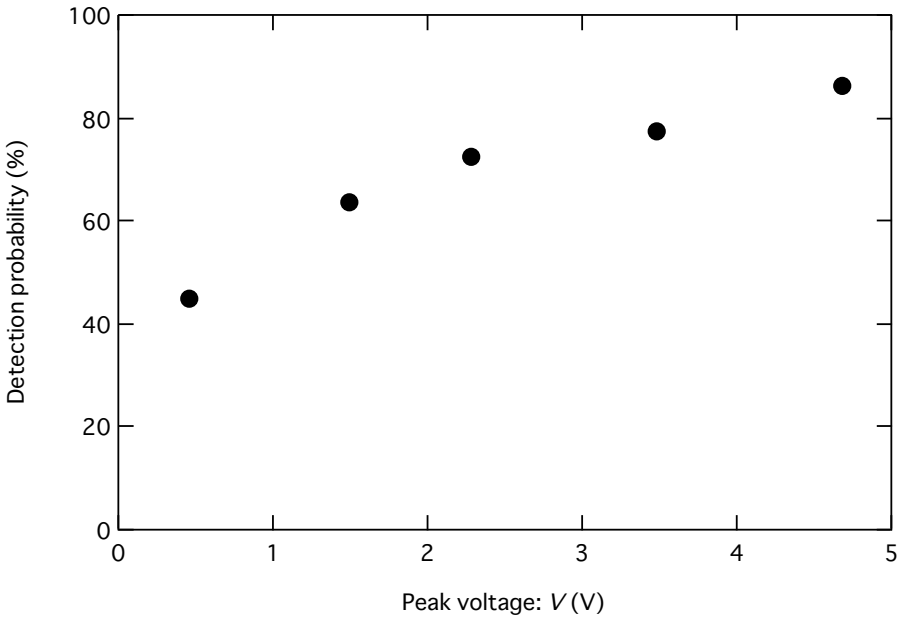

Fig. 4.9. The relation between V and detection probability.

In addition to the miss-detection, dV is not necessarily corresponding to V depending on the signal magnitude and the timing of signal sampling. Typical probability of being sampled as dV bins for various V are listed in Table 4.7. The sum of the probabilities of each V corresponds to the detection probability plotted in Fig. 4.9.

Table 4.7. Probability of being sampled as dV bins for various V.

	Probability of being sampled as the dV bin (%)				
V (V)	0.03421–1 V	1–2 V	2–3 V	3–4 V	4–5 V
4.7	51.9	13.1	8.3	6.2	6.8
3.5	49.9	12.8	8.5	6.0	0
2.3	53.5	14.4	4.6	0	0
1.5	52.8	11.0	0	0	0
0.5	44.7	0	0	0	0

From the analyses about the probabilistic signal sampling effects, the data of dV $\geq$ 4 V are found to be the most robust to interpret. Therefore, at present we will use the measured data of

dV ≥ 4 V for further scientific discussions about cosmic dust.

Considering the signal sampling effect and the calibration law developed in Chapter 3 and Section 4.2, we investigated the physical properties, here especially mass, of the impacted dust particles which generates dV ≥ 4 V. Fig. 4.10 represents the probability distribution of being sampled as dV ≥ 4 V by an impact of dust particle having a certain mass at 20 km/s. These data plots were obtained from the signal data of LGG and nsPL experiments and the inclined solid line is the fitting curve on the plots of probability less than 100%. Probability of each plot was calculated by the pulse width corresponding to the amplitude of ≥4 V. Note that the masses of the LGG data plots are not actual mass but corrected by Eq. (3.3) using v = 20 km/s and ρ = 2.0 g/cm^3. The masses of the nsPL data were derived with the same manner as the LGG data. Here, T = 100°C is assumed. It is found that impacts of dust particles ≥~ 7×10^{-11} (~40 μm in diameter) are recorded as dV ≥ 4 V with 100%, while impacts of dust particles having m =~ 1×10^{-11} (~20 μm in diameter) generate the data of dV ≥ 4 V with 1%.

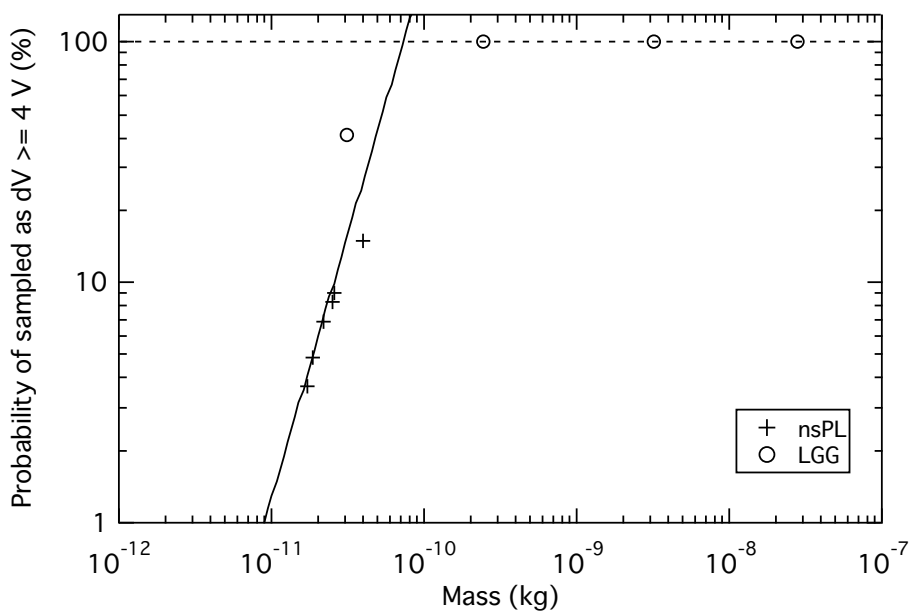

Fig. 4.10. Probability distribution of being sampled as dV ≥ 4 V by an impact of dust particle having a certain mass at 20 km/s.

We show how to analyze the actual measured data of dV ≥ 4 V obtained during a certain bin of heliocentric distance or observation time. First, we prepare the following parameters: T averaged over the bin, v, and assumed ρ of dust particles. Note that v is estimated by considering

the velocity vector of IKAROS, pointing information of the ALDN-S (direction of normal to the IKAROS membrane), and the distribution of orbital elements of typical zodiacal dust particles (Hirai et al., 2014). Then, we estimate mass by using V = 4 V in addition to the prepared T, v, and ρ. This estimated mass is the minimum mass (defined as probability of 1%), which is detectable as dV ≥ 4 V (i.e. dV = 4 V) under these T, v, and ρ conditions. From the relation represented in Fig. 4.10, we can finally find out the mass range of dust particles generating the measured data of dV ≥ 4V.

For example, at 0.72 AU with T = 180°C, v = 24 km/s (calculated by Keplerian velocity variation from 20 km/s at 1 AU), and ρ = 2.0 g/cm^3, the minimum diameter being detected as dV ≥ 4 V (the probability of 1% in Fig. 4.10) is ~67 μm.

Chapter 5

New Dust Distribution Model inside the Earth's Orbit

We calculated cumulative impact flux between 0.72 AU and 1.1 AU using the screened and reduced ALADDIN measurement data. The flux error of ALADDIN is well less than that of the past in-situ detectors. The highly accurate and precise flux by ALADDIN indicates significant discrepancy compared to the standard model of interplanetary dust flux at 1 AU, Grün model (Grün et al., 1985). We consider that this discrepancy is due to azimuthal difference in number density of interplanetary dust, i.e., circumsolar dust ring and blob. In order to reproduce the observed discrepancy of dust impact flux, we developed new hybrid dust distribution model, which can simultaneously handle the MMRs and the dust-dust collisions, by combining the MMRs model provided by Stark and Kuchner (2008) and the collisional evolution algorithm developed by Ishimoto (2000).

5.1 The ALADDIN Measurement Results and Its Interpretation

Using the 754 reduced measurement data of ALADDIN described in Chapter 4, we estimated cumulative flux (impact number of dust particles having $\geq m$ per unit of time, sensor area, and effective solid angle) and compared with fluxes obtained by the past in-situ dust detectors. We consider that the reduced ALADDIN data at 1 AU are composed of impacts by dust particles with $\geq$20 μm in diameter. From Fig. 5.1 depicts the cumulative flux obtained by

ALADDIN and the past in-situ dust detectors, the Galileo DDS and the Helios detector, along the heliocentric distance ranging from 0.7 AU to 1.1 AU. Note that the flux of the Helios detector is the averaged value during its 5-year measurement orbiting around the Sun between 0.3 AU and 1 AU, while the ALADDIN's and the Galileo DDS's were obtained at single passage in the interplanetary space. The trajectories of the three spacecrafts in the Sun-Earth line fixed coordinate is shown in Fig. 5.2.

The modeled cumulative flux at 1 AU by Grün et al. (1985) and its extrapolated flux profile to 0.7 AU are also shown in Fig. 5.1 as parallelogram boxes denoting the model uncertainty. The Grün model is an empirical mass (size) distribution of interplanetary dust particles based on in-situ flux measurement by Earth orbiting satellites and crater counting of lunar samples (Grün et al., 1985). This model has approximately one-order uncertainty in its flux values. The extrapolation is based on Keplerian velocity and geometrical concentration of number density (Eq. 18 in Grün et al., 1985). This model has been widely-referred for long by various cosmic dust studies not only around 1 AU but also for inferring dust distribution other than 1 AU (e.g., Poppe and Hornyi, 2012).

Note that the flux value of the Grün model in Fig. 5.1 is corrected from original value provided in Grün et al. (1985), in which a factor of gravitational enhancement, 2, is considered. They aimed at establishing an "interplanetary" dust flux model at 1 AU, which means the effect of Earth's gravity should be removed. Hence, they divided the raw flux value obtained at near-earth environment by the factor of gravitational enhancement. In contrast to their purpose, we need crude flux including Earth's gravity. Therefore, we corrected their providing flux values in Grün et al. (1985) by multiplying a factor of 2.

The radial concentration of dust number density due to PR effect is observed as upward trend of the measured flux along the heliocentric distance except for the Galileo measurement. It is also found that our ALADDIN shows the most accurate flux data in the past detectors thanks to its large sensor area and viewing angle despite the fact that ALADDIN detected larger ($\approx$ lower number density) dust particles than that detected by the past detectors. The flux of inbound and outbound orbit of ALADDIN are not much different each other. This feature may indicate that the 180°C-heated ALDN-S has been comparable with the sensor on the inbound orbit as suggested in Section 4.2.

The ALADDIN flux shows significant higher flux than the Grün flux, even considering the large uncertainty of the Grün flux. On the other in-situ measurement, their flux are within the uncertainty of Grün flux. The discrepancy found by the ALADDIN measurement may suggest the significant variation in azimuthal number density of large dust particles due to MMRs between Earth and interplanetary dust. Focusing on the dust distribution at 1 AU and using the 20 μm flux obtained by the ALADDIN, we tried to explain the observed discrepancy by use of the Stark model (MMRs-only) and our new hybrid model (MMRs and dust-dust collision).

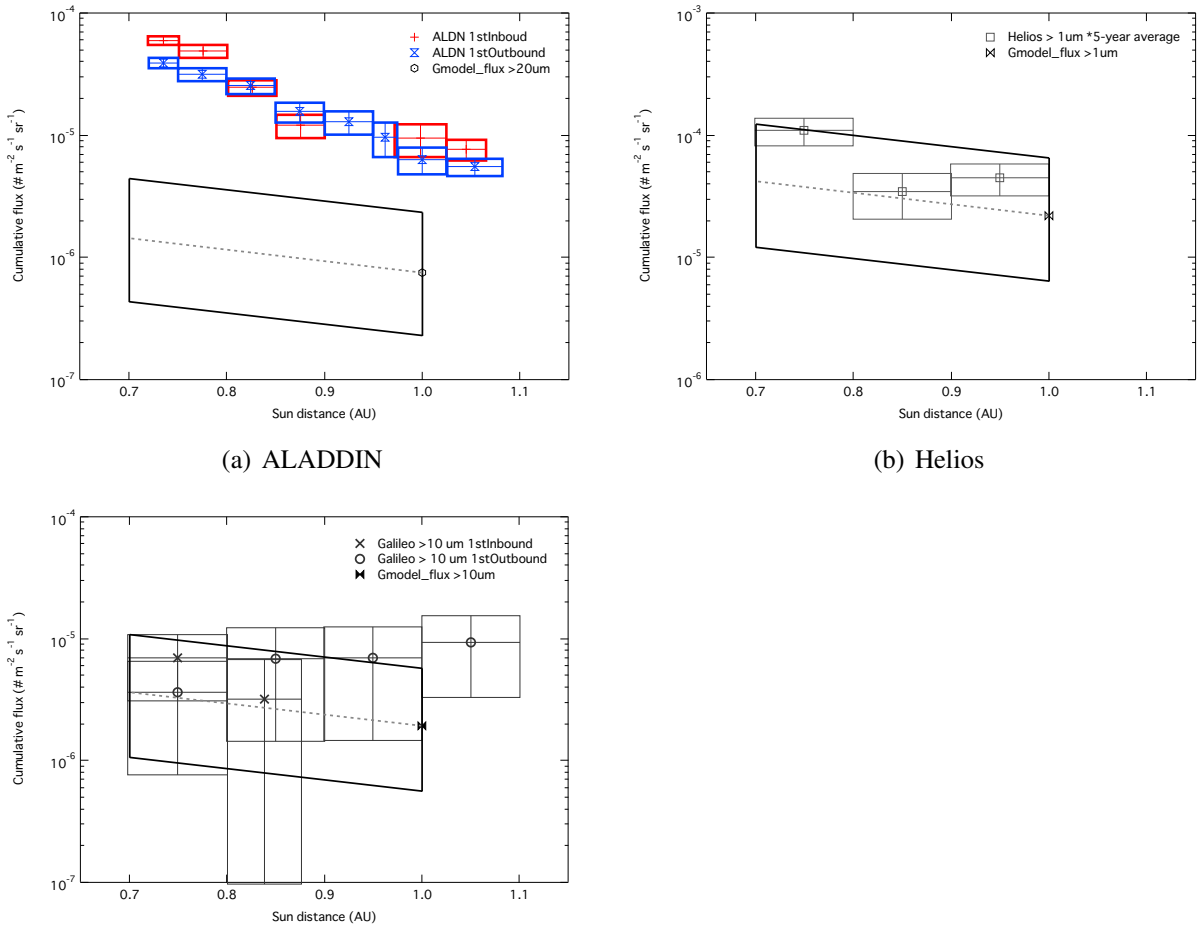

(a) ALADDIN

(b) Helios

(c) Galileo

Fig. 5.1. Flux comparison between (a) ALADDIN, (b) Helios, (c) Galileo, and Grün flux model. The detected size of dust particles by ALADDIN is dependent on the sensor temperature, i.e, heliocentric distance. At 1 AU, the detection threshold size was around ≥20 μm, and then the sensitivity was gradually degraded. After its perihelion passage, the ALADDIN detected dust particles larger than ~67 μm but it leaves a room for discussion (Section 4.2). The flux of Helios can be calculated with its measurement data of ≥1 μm due to its small sensor geometry (Section 2.2.1). The Galileo detector has large sensor area of 0.1 m^2, so the flux of ≥10 μm can be estimated.

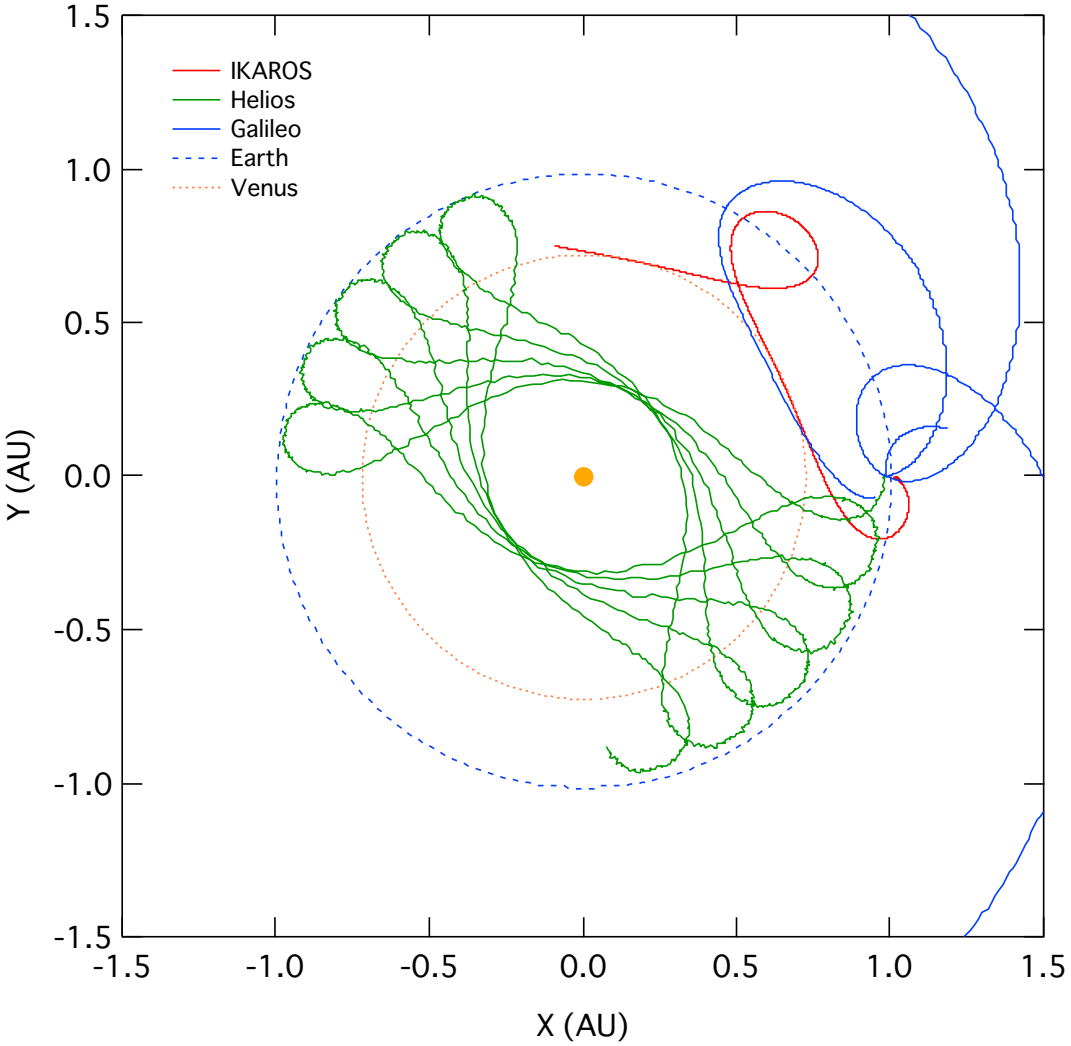

Fig. 5.2. Trajectories of the ALADDIN, Helios, and Galileo in the Sun-Earth line fixed coordinate. The fluxes from ALADDIN and Galileo were obtained in a part of their trajectory, while the flux from Helios is accumulated value along its whole trajectory.

5.2 Development of a New Hybrid Dust Distribution Model

5.2.1 Stark's Mean Motion Resonances (MMRs) Model

One of most reliable models for evaluating the effect of MMRs based on numerical calculation of substantial number of test particles has been provided by Stark and Kuchner (2008). They have provided their calculation results with various planet mass, test particle size, and semi-major axis of planet. The density of test particle is assumed to be 2.0 g/cm^3. The source region of test particles ranges from 3.5 AU to 4.375 AU and initial inclination are ranging in 0–20 degree. This Stark MMRs model does not include effects of dust-dust collisions on the particle distribution and only generates the relative value of the number density.

Fig. 5.3 shows examples of resulting maps of surface number density drawn in the Sun-Earth line fixed co-rotating coordinate system. The diameter of test particles are 8, 25, 80, 250 μm and a 1-earth-mass planet is orbiting at 1 AU around the Sun. It is found that the larger particles represent clearer contrast in number density than the smaller particles. Note that their simulation result of 25-μm-diameter particles is consistent with the ringed feature presented by the past simulation work (Fig. 1.3, Dermott et al., 1994).

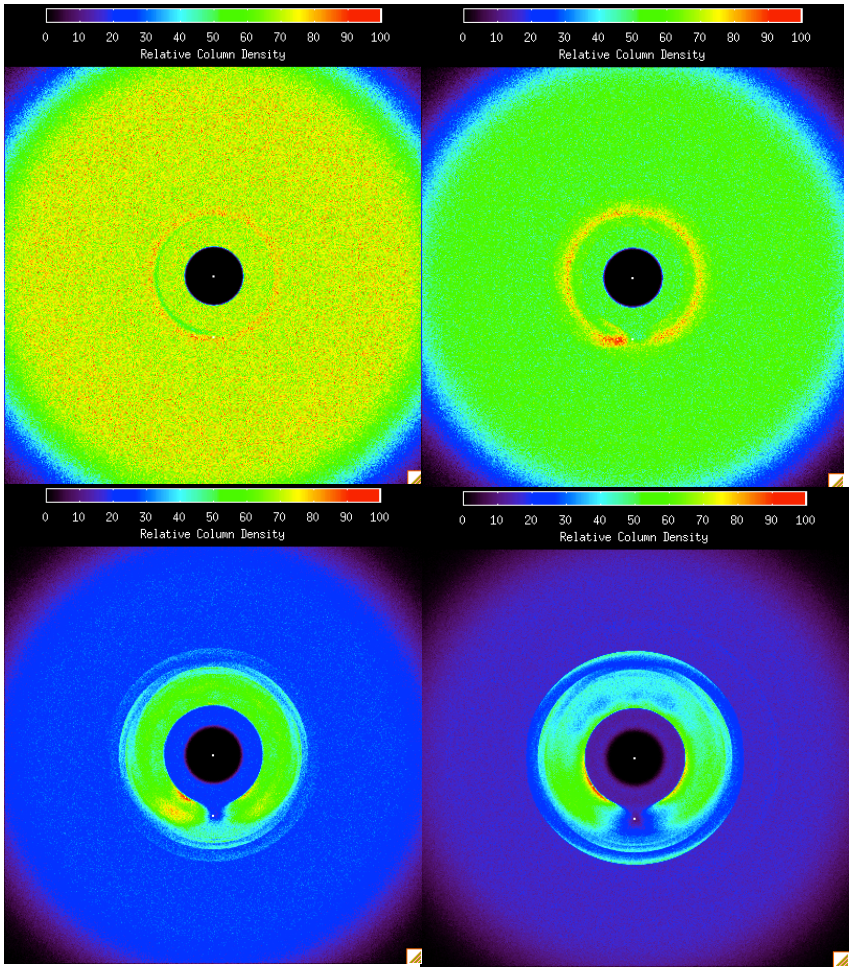

Fig. 5.3. Surface number density maps of 8 μm (upper left), 25 μm (upper right), 80 μm (bottom left), and 250 μm (bottom right) in diameter with 1 earth-mass planet orbiting at 1 AU (Stark and Kuchner, 2008).

5.2.2 Ishimoto's Collisional Model

Ishimoto (2000) developed a collisional evolution model for the dust distribution in the inner solar system. The Ishimoto model predicted selective variation of number density with dependence on the mass of dust particles and heliocentric distance. In contrast to the Stark MMRs model, the Ishimoto model does not include density variation due to MMRs.

In the Ishimoto model, the Grün model is used as initial or boundary condition to determine the dust size distribution at 1 AU. Orbital lifetime of dust particles, which is determined by collisional lifetime and PR lifetime, in the each mass bin is sequentially calculated for the each step of heliocentric distance. Both the collisional and PR lifetime are calculated in the same manner as Grün et al. (1985). Then, in accordance with orbit transition and collisional gain and loss for each mass at each heliocentric distance are calculated with following equations,

$$n(m,r-\Delta r) = n(m,r)dm - \Delta r \frac{\partial n(m,r)}{\partial r} dm, \tag{5.1}$$

$$\frac{\partial n}{\partial r} = -\frac{n}{r} - \frac{rc}{2\beta\mu}\left[\frac{dn_{\mathrm{g}}}{dt} - \frac{dn_{\mathrm{l}}}{dt} + \frac{dn_{\mathrm{s}}}{dt}\right] \tag{5.2}$$

where $\frac{dn_{\mathrm{g}}}{dt}$, $\frac{dn_{\mathrm{l}}}{dt}$, $\frac{dn_{\mathrm{s}}}{dt}$ are variation rate of number density at unit time by collisional gain, collisional loss, and supply from parent bodies at the heliocentric distance, r.

An example of calculated mass (size) distribution within 1 AU by the Ishimoto model is shown in Fig. 5.4. The example shows decreasing density of large particles ($>10^{-6}$ g, approximately $>\sim$100 μm in diameter) and increasing density of intermediate-sized particles (10^{-12}–10^{-6} g) in which range ~20 μm size (10^{-8} g) the reduced ALADDIN measurement data covers is included. These feature means that destructed large particles, which have shorter collisional lifetime than PR lifetime, makes the density of intermediate-sized particles higher. The number density of small particles ($<10^{-12}$ g) drops sharply because these small particles are blown out by the radiation pressure due to its high β value (Eq. (1.3)).

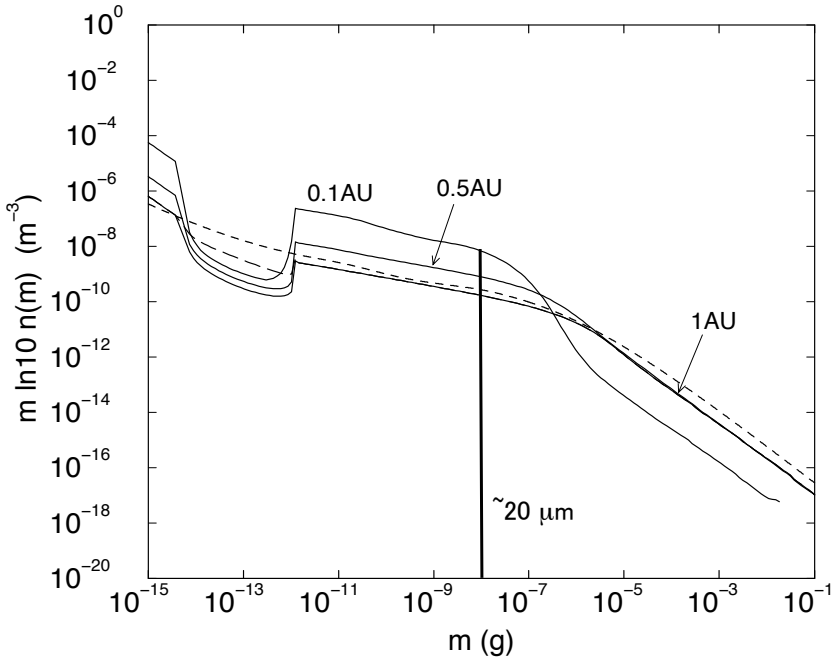

Fig. 5.4. Calculated size distribution within 1 AU by the Ishimoto model (Ishimoto, 2000). Dashed line denotes the mass distribution at 1 AU by the Grün model. The reduced ALADDIN measurement data covers ~20 μm to several tens micron sized dust particles.

5.2.3 A New MMRs-Collisional Hybrid Model

We made a new MMRs-collisional hybrid model by introducing MMRs effect estimated by Stark and Kuchner (2008) into the collisional evolution model by Ishimoto (2000). Fig. 5.5 shows radial density profiles from the Stark model (blue and red solid line) along the "gap line" and "trailing line" illustrated in Fig. 5.7, which are corespondent with the 1 AU position of the IKAROS-ALADDIN trajectory. Also, density profile without collision nor MMRs, which is equivalent to the non-collision version of the Ishimoto model, is shown. In order to implement the MMRs effect into the Ishimoto model, the non-collision Ishimoto model should be equivalent with the Stark's MMRs-only density profile along the both gap and trailing line, respectively. Hence, the modified non-collision version of Ishimoto model can be expressed as modified Eq. (5.2) as follows:

$$\frac{\partial n}{\partial r} = -\frac{n}{r}x \tag{5.3}$$

where x is a correction coefficient in order to match the number density profile of the Stark model. By using the Stark density maps of 8, 25, 80, and 250 μm in diameter with 1 Earth-mass planet orbiting at 1 AU from the Sun-mass central star, we calculated radial density profiles between 8 and 250 μm at a r step of 0.001 AU and a mass step of 0.1 in log m (g). Then, we estimated the coefficient x for each r and log m steps. Finally, by adding collisional and supply term as described in Eq. (5.2), an equation of the new MMRs-collisional hybrid model has been developed as follows:

$$\frac{\partial n}{\partial r} = -\frac{n}{r}x - \frac{rc}{2\beta\mu}\left[\frac{dn_{\mathrm{g}}}{dt} - \frac{dn_{\mathrm{l}}}{dt} + \frac{dn_{\mathrm{s}}}{dt}\right] \tag{5.4}$$

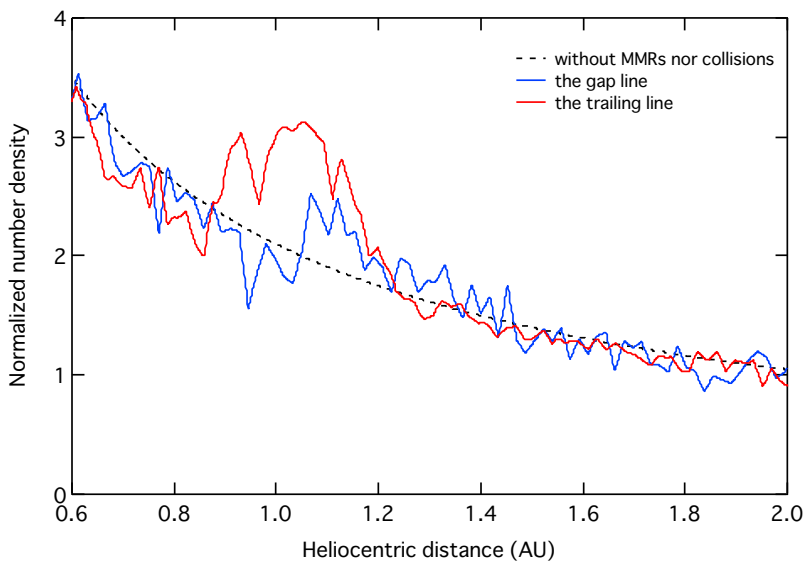

Fig. 5.5. Radial profiles of normalized number density of 25 μm test particles along the gap line (blue solid line) and the trailing line (red solid line) retrieved from the Stark's density map. Dashed line denotes the density profile without MMRs nor dust-dust collision (density $\propto r^{-1}$).

Boundary condition and model parameters, i.e., initial distribution, collisional gain and loss algorithm, and dust supply rate from parent bodies, are referred from the past modeling works and in-situ dust flux measurements.

For the boundary condition, we adopted the Grün flux at 1 AU same as the Ishimoto model. We will modify the model parameters in order to fit our calculation result with Grün flux at 1 AU. At this moment, however, we have not finished the parameter adjustment, so it will be completed in the future works.

We defined that the calculation is started at 2 AU in order to estimate the dust size distribution within 1 AU. Ten times reduced Grün differential number density is tentatively used as the initial size distribution at 2 AU. Fig. 5.6 shows the differential number density by Grün et al. (1985) at both 1 AU and 2 AU.

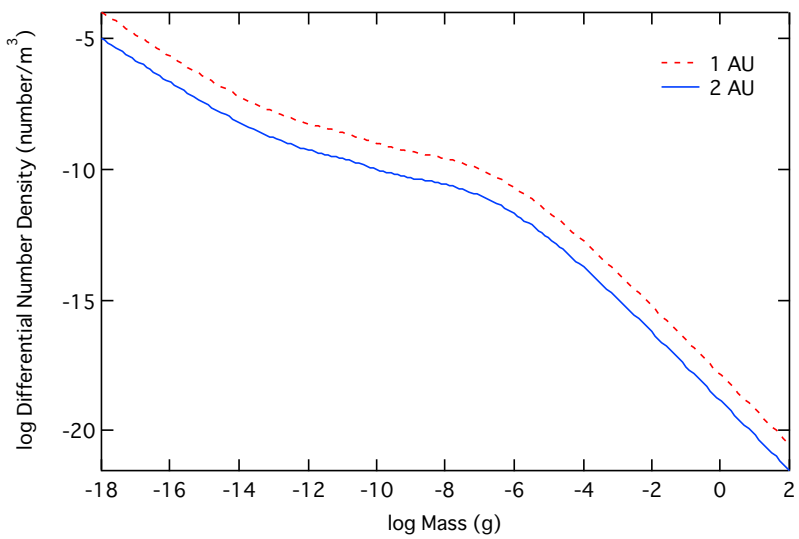

Fig. 5.6. The initial number density at 2 AU calculated from Grün flux model (Grün et al., 1985). The differential number density at 1 AU and 2 AU are shown as red-dashed line and blue-solid line, respectively.

Our collisional gain and loss rate, which are equivalent to that of Grün et al. (1985) Ishimoto (2000) also used, can be written as follows:

$$\frac{dn_g(m,r)}{dt} = \iint g(m_p,m_t,m)n(m_t,r)n(m_p,r)v_i(r)dm_p dm_t \tag{5.5}$$

$$\frac{dn_l(m,r)}{dt} = n(m,r)\int n(m_p,r)v_i(r)\sigma(m,m_p)dm_p \tag{5.6}$$

where m_p and m_t are the masses of the projectile and the target, respectively, and σ is the collisional cross section. The mean impact velocity, $v_i(r)$, can be calculated from $0.53 \times v_k$ (v_k is Keplerian velocity at a given heliocentric distance), taking into account dispersion of orbital inclination (~30°) and orbital evolution due to Poynting-Robertson drag. For example, $v_i(r)$ at 1 AU equals ~16 km/s. Note that we have not included dust particles on hyperbolic trajectory. The $g(m_p,m_t,m)$, which is equivalent to Eq. (1.4), denotes the impact fragment size

distribution. The slope of size distribution, η, is same as Grün et al. (1985), 0.83.

The dust supply rate was determined on the basis of Ishimoto (2000) and Economou et al. (2013) and expressed as follows:

$$\frac{dn_{\mathrm{s}}(m,r)}{dt} = 1.0 \times 10^{-31} m^{-0.65} r^{-3.5} \tag{5.7}$$

The heliocentric dependence, -3.5, is referred from Ishimoto (2000), in which they determined it by using the boundary condition of the Grün flux at 1 AU. The increasing supply rate with decreasing heliocentric distance represents the dust supply from comets. They also included the dust supply from asteroids, but it is confined between 2 AU and 3 AU. Since our calculation starts from at 2 AU, we neglected the asteroidal dust supply.

In Economou et al. (2013), the result of in-situ dust measurement at the flyby of Comet 9P/Tempel 1 conducted by Dust Flux Monitor Instrument of Stardust-NExT mission is reported. They estimated the mass dependence of dust particles from the comet as -0.65. According to Nesvorny et al. (2010), the dominant source of cometary dust for zodiacal cloud is due to Jupiter-family comets (JFCs). Since Comet 9P/Tempel 1 is a periodic JFC, so we can consider this mass dependence as typical value for the cometary dust supply.

5.3 Azimuthal Variation of Interplanetary Dust Particles at 1 AU

Using the newly developed MMRs-collision hybrid model, we investigated the observed azimuthal discrepancy in dust number density at 1 AU. The number densities used were calculated from the impact flux on the ALADDIN and the Grün flux. Both the simulation results from the Stark model and the new hybrid model are compared with the in-situ measured flux by the ALADDIN and the Grün model which is based on in-situ measurement around the earth.

Fig. 5.7 shows the trajectory of IKAROS spacecraft superimposed on the Stark 25-μm density map. The density map predicts that the ALADDIN on its inbound orbit detected the trailing clump of the earth.

Fig. 5.8 shows the differential number density of 20 μm obtained and simulated by the in-situ measurement (ALADDIN and Grün flux), the Stark model, and our new hybrid model. The differential number density of in-situ measurements were calculated by the correlation between cumulative flux and differential number density presented in Grün et al. (1985). Note that we used the Grün flux as boundary condition in the calculation of our hybrid model. Hence, the density at 1 AU of heliocentric distance on the gap line is biased to correspond to the Grün flux same as the Stark model (see Section 5.2.1).

The in-situ measurement shows significant difference between the gap and the trailing clump by a factor of 12.6, while the difference estimated by the Stark model and our new model are a factor of 1.7 and 2.1, respectively. However, considering the uncertainty of the number density of in-situ measurements, especially large error bar of the Grün flux, the difference could be 2.8 at the minimum. Consequently, our new model shows better estimate of discrepancy between the gap and trailing clump.

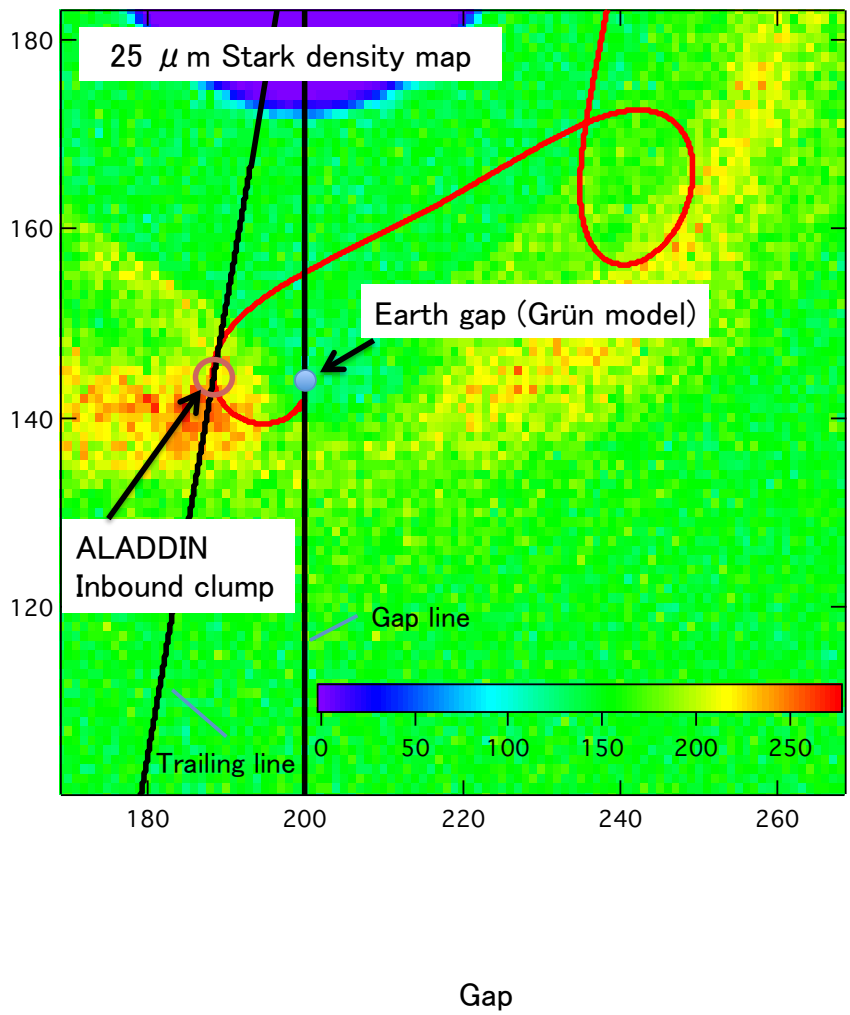

Fig. 5.7. The trajectory of ALADDIN superimposed on the Stark 25-μm density map. The color scale represents relative number density (Stark and Kuchner, 2008).

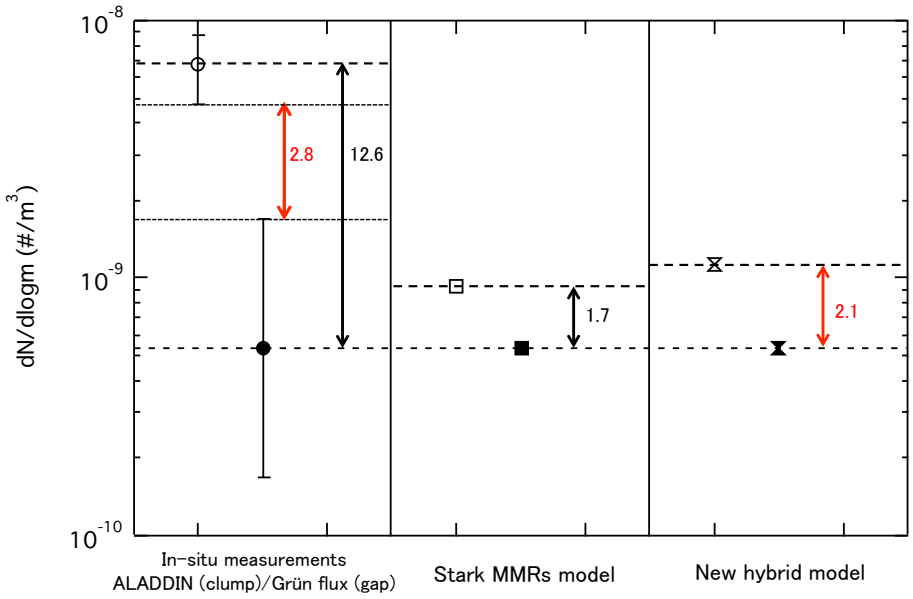

Fig. 5.8. The comparison of in-situ measurements an model calculations. The in-situ measurement density are obtained by ALADDIN and the Grün flux. The simulation density calculated by using stark model and our new hybrid model are compared with the in-situ measurement density.

Chapter 6

Conclusions and Future Work

6.1 Conclusions

The largest PVDF-based in-situ dust detector, ALADDIN, was calibrated using the extrapolation method with the LGG experiment and complementary experiment with the nsPL. The calibration shows that the ALADDIN has ability to detect ≥10-μm-sized dust particles within its dynamic range.

From the analysis of the combination and dV value of flagged channels, the measured data of ALADDIN in space can be reduced to the physical properties of detected dust particles. As a specific issues of the ALADDIN, the sampling probability due to the detector electronics and thermal degradation of PVDF at significantly high temperature are also investigated. The reduced ALADDIN data provides the 10 times more accurate flux value of ≥10-μm-sized dust particles in the past in-situ measurements.

The comparison of the flux obtained by the ALADDIN and the Grün flux model revealed unambiguous discrepancy between the gap region and the trailing clump region at 1 AU distance from the sun. In order to interpret the observed density variation, we developed a hybrid model, which can handle simultaneously the MMRs and dust-dust collision effect in the calculation for the dust number density by introducing an existing dust-dust collision model (Ishimoto model) to the MMRs model (Stark model). The new hybrid model can estimate the density difference between the gap and the trailing clump observed by the ALADDIN measurement and the Grün flux model better than the MMRs-only model or the collision only model.

6.2 Future Works

Orbiting around the Sun between 1 AU and 0.7 AU, IKAROS made Venus closest approach (VCA) close to ~13 Venus radii at its first inbound orbit. Fig. 6.1 shows the trajectory of IKAROS in the Sun-Venus line fixed co-rotating coordinate system. The ALADDIN successfully measured dust impact flux around the VCA. From analyses of these flux data obtained by the ALADDIN at VCA, we will expand our newly developed dust distribution model in order to explain the observed anisotropy in dust distribution around Venus.

In addition to the ringed structure along the Venus orbital path observed by Helios and STEREO (Section 2.1.1 and 2.1.3), our ALADDIN will provide the dust distribution in the vicinity of Venus with its detailed in-situ measurement data. Venus should have gap structure similar to that around the Earth.

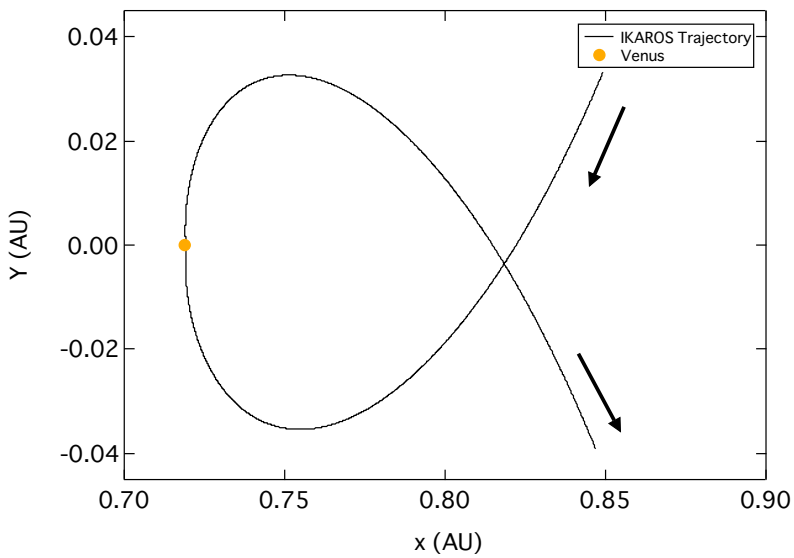

Fig. 6.1. The IKAROS trajectory at its Venus closest approach plotted in the Sun-Venus line fixed co-rotating coordinate system.

Further investigation of model parameters, such as size distribution at the initial heliocentric distance or the fragment size distribution produced by dust-dust collisions, will give the complete model to reproduce the measured difference of number density at 1 AU. The developed hybrid model for 1 AU can be expanded to estimate the dust distribution at 0.7 AU including gap and clump structures induced by Venus MMRs. Hence, a practical cosmic dust distribution model inside the Earth's orbit will be developed.

Our distribution model for cosmic dust inside the Earth's orbit can be also used to estimate dust distribution in the outer region of the Solar System. It has been thought that Neptune has the gap and clump structure caused by MMRs around its orbital trajectory (e.g., Liou and Zook, 1999). In-situ measurement data will be obtained by the Student Dust Counter onboard NASA New Horizons spacecraft in near future (Han et al., 2011).

Ultimately, our model will provide unique insights about formation and evolution of exo-zodiacal cloud or dust disks by constraining the mechanisms of interaction between MMRs and dust-dust collisions. Thanks to the knowledge obtained in dust distribution of our Solar System, the physical properties, such as mass or orbital radii, of hidden planets inside the exo-planetary disk can be estimated.

Acknowledgements

First, I would like to thank to my practical Ph.D. advisor, Dr. Hajime Yano, who is also the principal investigator of IKAROS-ALADDIN, for his academic supervision and joint research. He provided research opportunity as ALADDIN-PI. I thank to my official Ph.D. advisor, Dr. Makoto Yoshikawa, for administrative support. They supported me over the entire period of 4 years my Ph.D. work.

I thank the past and present staff at HIT, especially Dr. Hiromi Shibata, Dr. Takeo Iwai and Mr. Takao Omata, and MPIK, especially Prof. Eberhard Grün, Dr. Ralf Srama, and Mr. Sebastian Bugiel, respectively, for their support to our use of their VdGs. I appreciate Dr. Sunao Hasegawa and other supporting staff of the ISAS Plasma Experiment Laboratory and Mr. Mike Cole and Prof. Mark J. Burchell of UKC, respectively, for their assistance and operation of their LGGs. I wish to thank Dr. Masanori Kobayashi of PERC for his assistance and advice in the nsPL experiments.

The VdG experiments at HIT and MPIK were supported by the join usage of HIT. The VdG experiments at MPIK were supported by the exchange program of Center for Planetary Science (CPS) and the course-by-course education program of the Graduate University for Advanced Studies. The LGG experiments at ISAS were supported by the Plasma Experiment Laboratory, ISAS-JAXA. The LGG experiments at UKC were supported by JAXA's Solar Power Sail Working Group and the course-by-course education program of the Graduate University for Advanced Studies.

I would like to thank the IKAROS project led by Dr. Osamu Mori and Dr. Yuichi Tsuda for operating the IKAROS spacecraft and giving us the flight opportunity. Other members of the IKAROS- ALADDIN team are acknowledged for their contributions to design, build, test, operate, and analyze space data of ALADDIN: Mr. Masayuki Fujii, Dr. Naoko Ogawa, Dr.

Chisato Okamoto, Mr. Nobuyuki Moriyama, Dr. Kyoko Okudaira, and Dr. Makoto Tanaka. I also give thank to Dr. Maki Nakamura for her existence as only one coeval student struggling the dust research.

Finally, I would like to express my thanks to my parents, wife, and cats. Their existence always mitigated my pain and anxiety from the dismal situation of my Ph.D. work. This work would not be finished without their existence.

Bibliography

Altobelli, N., Kempf, S., Landgraf, M., Srama, R., Dikarev, V., Krüger, H., Moragas-Klostermeyer, G., Grün, E., 2003. Cassini between Venus and Earth: Detection of interstellar dust. Journal of Geophysical Research A: Space Physics 108. Cited By (since 1996) 27.

Asada, N., 1985. Fine fragments in high-velocity impact experiments. Journal of Geophysical Research: Solid Earth 90, 12445–12453.

Burchell, M.J., Cole, M.J., McDonnell, J.A.M., Zarnecki, J.C., 1999. Hypervelocity impact studies using the 2 MV Van de Graaff accelerator and two-stage light gas gun of the University of Kent at Canterbury. Measurement Science and Technology 10, 41.

Burns, J.A., Lamy, P.L., Soter, S., 1979. Radiation forces on small particles in the solar system. Icarus 40, 1 – 48.

Dermott, S., Jayaraman, S., Xu, Y., Gustafson, B., Liou, J., 1994. A circumsolar ring of asteroidal dust in resonant lock with the earth. Nature 369, 719–723. Cited By (since 1996) 95.

Dohnanyi, J.S., 1969. Collisional model of asteroids and their debris. Journal of Geophysical Research 74, 2531–2554.

Eberle, G., Eisenmenger, W., 1992. Thermal depolarization of PVDF: anomaly at 180 degC. Electrical Insulation, IEEE Transactions on 27, 768–772.

Economou, T.E., Green, S.F., Brownlee, D.E., Clark, B.C., 2013. Dust flux monitor instrument measurements during stardust-next flyby of comet 9p/tempel 1. Icarus 222, 526 – 539. <ce:title>Stardust/EPOXI</ce:title>.

Fujiwara, A., Kamimoto, G., Tsukamoto, A., 1977. Destruction of basaltic bodies by high-velocity impact. Icarus 31, 277 – 288.

Gault, D.E., Wedekind, J.A., 1969. The destruction of tektites by micrometeoroid impact. Journal of Geophysical Research 74, 6780–6794.

Grün, E., 1981. Physikalische und chemische Eigenschaften des interplanetaren Staubes-Messungen des Mikrometeoritenexperimentes auf Helios. Technical Report. Max Planck Institute for Nuclear Physics. Weltraumforschung/Weltraumtechnologie.

Grün, E., Baguhl, M., Divine, N., Fechtig, H., Hamilton, D., Hanner, M., Kissel, J., Lindblad, B.A., Linkert, D., Linkert, G., Mann, I., McDonnell, J., Morfill, G., Polanskey, C., Riemann, R., Schwehm, G., Siddique, N., Staubach, P., Zook, H., 1995. Three years of Galileo dust data. Planetary and Space Science 43, 953 – 969.

Grün, E., Fechtig, H., Hanner, M.S., Kissel, J., Lindblad, B.A., Linkert, D., Maas, D., Morfill, G.E., Zook, H.A., 1992. The Galileo Dust Detector. Space Sci. Rev. 60, 317–340.

Grün, E., Pailer, N., Fechtig, H., Kissel, J., 1980. Orbital and physical characteristics of micrometeoroids in the inner solar system as observed by Helios 1. Planetary and Space Science 28, 333 – 349.

Grün, E., Zook, H., Fechtig, H., Giese, R., 1985. Collisional balance of the meteoritic complex. Icarus 62, 244 – 272.

Grün, E., Zook, H.A., Baguhl, M., Balogh, A., Bame, S.J., Fechtig, H., Forsyth, R., Manner, M.S., Horanyi, M., Kissel, J., Lindblad, B.A., Linkert, D., Linkert, G., Mann, I., McDonnell, J.A.M., Morfill, G.E., Phillips, J.L., Polanskey, C., Schwehm, G., Siddique, N., Staubach, P., Svestka, J., Taylor, A., 1993. Discovery of Jovian dust streams and interstellar grains by the Ulysses spacecraft. Nature 362, 428–430.

Hahn, J.M., Zook, H.A., Cooper, B., Sunkara, B., 2002. Clementine Observations of the Zodiacal Light and the Dust Content of the Inner Solar System. Icarus 158, 360 – 378.

Han, D., Poppe, A., Piquette, M., Grün, E., Horanyi, M., 2011. Constraints on dust production in the edgeworth-kuiper belt from pioneer 10 and new horizons measurements. Geophysical Research Letters 38. Cited By (since 1996) 0.

Harsanyi, G., 1995. Polymer Films in Sensor Applications. Taylor & Francis.

Hasegawa, S., Hamabe, Y., Fujiwara, A., Yano, H., Sasaki, S., Ohashi, H., Kawamura, T., Nogami, K.I., Kobayashi, K., Iwai, T., Shibata, H., 2001. Microparticle acceleration for hypervelocity experiments by A 3.75MV van de Graaff accelerator and a 100KV electrostatic accelerator in Japan. International Journal of Impact Engineering 26, 299 – 308.

Hirai, T., Cole, M.J., Fujii, M., Hasegawa, S., Iwai, T., Kobayashi, M., Srama, R., Yano, H., 2014. Microparticle impact calibration of the Arrayed Large-Area Dust Detectors in {INterplanetary} space (ALADDIN) onboard the solar power sail demonstrator {IKAROS}. Planetary and Space Science , –.

Holland, W.S., Greaves, J.S., Zuckerman, B., Webb, R.A., McCarthy, C., Coulson, I.M., Walther, D.M., Dent, W.R.F., Gear, W.K., Robson, I., 1998. Submillimetre images of dusty debris around nearby stars. Nature 392, 788–791.

Ishimoto, H., 2000. Modeling the number density distribution of interplanetary dust on the ecliptic plane within 5 AU of the Sun. A&A 362, 1158–1173.

James, D., Hoxie, V., Horanyi, M., 2010. Polyvinylidene fluoride dust detector response to particle impacts. Review of Scientific Instruments 81, 034501.

Jones, M.H., Bewsher, D., Brown, D.S., 2013. Imaging of a circumsolar dust ring near the orbit of venus. Science 342, 960–963. Supplementary Materials: Jones2013suppl http://www.sciencemag.org/content/suppl/2013/11/20/342.6161.960.DC1/Jones.SM.pdf.

Kawai, H., 1969. The Piezoelectricity of Poly (vinylidene Fluoride). Japanese Journal of Applied Physics 8, 975–976.

Kelsall, T., Weiland, J.L., Franz, B.A., Reach, W.T., Arendt, R.G., Dwek, E., Freudenreich, H.T., Hauser, M.G., Moseley, S.H., Odegard, N.P., Silverberg, R.F., Wright, E.L., 1998. The

COBE Diffuse Infrared Background Experiment Search for the Cosmic Infrared Background. II. Model of the Interplanetary Dust Cloud. The Astrophysical Journal 508, 44.

Kempf, S., Srama, R., Horanyi, M., Burton, M., Helfert, S., Moragas-Klostermeyer, G., Roy, M., Grun, E., 2005. High-velocity streams of dust originating from Saturn. Nature 433, 289–291.

Leinert, C., Moster, B., 2007. Evidence for dust accumulation just outside the orbit of Venus. Astronomy and Astrophysics 472, 335–340. Cited By (since 1996) 2.

Leinert, C., Richter, I., Pitz, E., Hanner, M., 1980. The plane of symmetry of interplanetary dust in the inner solar system. A&A 82, 328–336.

Leinert, C., Richter, I., Pitz, E., Planck, B., 1981. The zodiacal light from 1.0 to 0.3 A.U. as observed by the HELIOS space probes. A&A 103, 177–188.

Leinert, C., Roser, S., Buitrago, J., 1983. How to maintain the spatial distribution of interplanetary dust. A&A 118, 345–357.

Liou, J.C., Zook, H.A., 1999. Signatures of the giant planets imprinted on the edgeworth-kuiper belt dust disk. The Astronomical Journal 118, 580.

Horanyi, M., Hoxie, V., James, D., Poppe, A., Bryant, C., Grogan, B., Lamprecht, B., Mack, J., Bagenal, F., Batiste, S., Bunch, N., Chanthawanich, T., Christensen, F., Colgan, M., Dunn, T., Drake, G., Fernandez, A., Finley, T., Holland, G., Jenkins, A., Krauss, C., Krauss, E., Krauss, O., Lankton, M., Mitchell, C., Neeland, M., Reese, T., Rash, K., Tate, G., Vaudrin, C., Westfall, J., 2008. The Student Dust Counter on the New Horizons Mission. Space Science Reviews 140, 387–402. 10.1007/s11214-007-9250-y.

Mocker, A., Bugiel, S., Auer, S., Baust, G., Colette, A., Drake, K., Fiege, K., Grün, E., Heckmann, F., Helfert, S., Hillier, J., Kempf, S., Matt, G., Mellert, T., Munsat, T., Otto, K., Postberg, F., Roser, H.P., Shu, A., Sternovsky, Z., Srama, R., 2011. A 2 mv van de graaff accelerator as a tool for planetary and impact physics research. Review of Scientific Instruments 82, 095111.

Nakamura, A., Fujiwara, A., 1991. Velocity distribution of fragments formed in a simulated collisional disruption. Icarus 92, 132 – 146.

Nesvorny, D., Jenniskens, P., Levison, H.F., Bottke, W.F., Vokrouhlicky, D., Gounelle, M., 2010. Cometary origin of the zodiacal cloud and carbonaceous micrometeorites. implications for hot debris disks. The Astrophysical Journal 713, 816.

Ozernoy, L.M., Gorkavyi, N.N., Mather, J.C., Taidakova, T.A., 2000. Signatures of exosolar planets in dust debris disks. The Astrophysical Journal Letters 537, L147.

Pierazzo, E., Melosh, H.J., 2000. Understanding oblique impacts from experiments, observations, and modeling. Annual Review of Earth and Planetary Sciences 28, 141–167. PMID: 11583040.

Poppe, A., Hornyi, M., 2012. On the edgeworth-kuiper belt dust flux to saturn. Geophysical Research Letters 39. Cited By (since 1996) 0.

Poppe, A., Jacobsmeyer, B., James, D., Horanyi, M., 2010. Simulation of polyvinylidene fluoride detector response to hypervelocity particle impact. Nuclear Instruments and Methods in Physics Research Section A: Accelerators, Spectrometers, Detectors and Associated Equipment 622, 583 – 587.

Poppe, A., James, D., Horanyi, M., 2011. Measurements of the terrestrial dust influx variability by the cosmic dust experiment. Planetary and Space Science 59, 319 – 326.

Reach, W.T., Morris, P., Boulanger, F., Okumura, K., 2003. The mid-infrared spectrum of the zodiacal and exozodiacal light. Icarus 164, 384 – 403.

Robertson, H.P., 1937. Dynamical effects of radiation in the solar system. MNRAS 97, 423.

Röser, S., Staude, H.J., 1978. The zodiacal light from 1500 A to 60 micron - Mie scattering and thermal emission. A&A 67, 381–394.

Shibata, H., Kobayashi, K., Iwai, T., Hamabe, Y., Sasaki, S., Hasegawa, S., Yano, H., Fujiwara, A., Ohashi, H., Kawamura, T., ichi Nogami, K., 2001. Microparticle acceleration by a van

de graaff accelerator and application to space and material sciences. Radiation Physics and Chemistry 60, 277 – 282. International symposium on prospects for application of radiation.

Shu, A., Bugiel, S., Grün, E., Hillier, J., Horányi, M., Munsat, T., Srama, R., 2013. Cratering studies in polyvinylidene fluoride (pvdf) thin films. Planetary and Space Science In press.

Simpson, J., Rabinowitz, D., Tuzzolino, A., 1989. Cosmic dust investigations: I. pvdf detector signal dependence on mass and velocity for penetrating particles. Nuclear Instruments and Methods in Physics Research Section A: Accelerators, Spectrometers, Detectors and Associated Equipment 279, 611 – 624.

Simpson, J., Tuzzolino, A., 1985. Polarized polymer films as electronic pulse detectors of cosmic dust particles. Nuclear Instruments and Methods in Physics Research Section A: Accelerators, Spectrometers, Detectors and Associated Equipment 236, 187 – 202.

Simpson, J.A., Sagdeev, R.Z., Tuzzolino, A.J., Perkins, M.A., Ksanfomality, L.V., Rabinowitz, D., Lentz, G.A., Afonin, V.V., Ero, J., Keppler, E., Kosorokov, J., Petrova, E., Szabo, L., Umlauft, G., 1986. Dust counter and mass analyser (ducma) measurements of comet halley's coma from vega spacecraft. Nature 321, 278–280.

Simpson, J.A., Tuzzolino, A.J., 1984. Pyroelectric materials as electronic pulse detectors of ultraheavy nuclei. Phys. Rev. Lett. 52, 601–604.

Spieler, H., 2005. Semiconductor Detector Systems. Oxford University Press.

Srama, R., Ahrens, T.J., Altobelli, N., Auer, S., Bradley, J.G., Burton, M., Dikarev, V.V., Economou, T., Fechtig, H., Görlich, M., Grande, M., Graps, A., Grün, E., Havnes, O., Helfert, S., Horanyi, M., Igenbergs, E., Jessberger, E.K., Johnson, T.V., Kempf, S., Krivov, A.V., Krüger, H., Mocker-Ahlreep, A., Moragas-Klostermeyer, G., Lamy, P., Landgraf, M., Linkert, D., Linkert, G., Lura, F., McDonnell, J.A.M., Möhlmann, D., Morfill, G.E., Müller, M., Roy, M., Schäfer, G., Schlotzhauer, G., Schwehm, G.H., Spahn, F., Stübig, M., Svestka, J., Tschernjawski, V., Tuzzolino, A.J., Wäsch, R., Zook, H.A., 2004. The cassini cosmic dust analyzer. Space Science Reviews 114, 465–518. 10.1007/s11214-004-1435-z.

Stark, C.C., Kuchner, M.J., 2008. The detectability of exo-earths and super-earths via resonant signatures in exozodiacal clouds. The Astrophysical Journal 686, 637.

Stark, C.C., Kuchner, M.J., 2009. A new algorithm for self-consistent three-dimensional modeling of collisions in dusty debris disks. The Astrophysical Journal 707, 543.

Su, K.Y.L., Rieke, G.H., Malhotra, R., Stapelfeldt, K.R., Hughes, A.M., Bonsor, A., Wilner, D.J., Balog, Z., Watson, D.M., Werner, M.W., Misselt, K.A., 2013. Asteroid belts in debris disk twins: Vega and fomalhaut. The Astrophysical Journal 763, 118.

Takasawa, S., Nakamura, A.M., Kadono, T., Arakawa, M., Dohi, K., Ohno, S., Seto, Y., Maeda, M., Shigemori, K., Hironaka, Y., Sakaiya, T., Fujioka, S., Sano, T., Otani, K., Watari, T., Sangen, K., Setoh, M., Machii, N., Takeuchi, T., 2011. Silicate dust size distribution from hypervelocity collisions: Implications for dust production in debris disks. The Astrophysical Journal Letters 733, L39.

Tuzzolino, A., 1983. Pulse amplitude method for determining the pyroelectric coefficient of pyroelectric materials. Nuclear Instruments and Methods in Physics Research 212, 505 – 516.

Tuzzolino, A., Economou, T., McKibben, R., Simpson, J., BenZvi, S., Blackburn, L., Voss, H., Gursky, H., 2005. Final results from the space dust (spadus) instrument flown aboard the earth-orbiting {ARGOS} spacecraft. Planetary and Space Science 53, 903 – 923.

Tuzzolino, A.J., Economou, T.E., McKibben, R.B., Simpson, J.A., McDonnell, J.A.M., Burchell, M.J., Vaughan, B.A.M., Tsou, P., Hanner, M.S., Clark, B.C., Brownlee, D.E., 2003. Dust flux monitor instrument for the stardust mission to comet wild 2. J. Geophys. Res. 108, 8115.

Wada, Y., Hayakawa, R., 1976. Piezoelectricity and pyroelectricity of polymers. Japanese Journal of Applied Physics 15, 2041–2057.

Wyatt, M.C., 2005. The insignificance of p-r drag in detectable extrasolar planetesimal belts. A&A 433, 1007–1012.

Wyatt, M.C., Dermott, S.F., Telesco, C.M., Fisher, R.S., Grogan, K., Holmes, E.K., Pina, R.K., 1999. How observations of circumstellar disk asymmetries can reveal hidden planets: Pericenter glow and its application to the hr 4796 disk. The Astrophysical Journal 527, 918.

Wyatt, S.P., Whipple, F.L., 1950. The poynting-robertson effect on meteor orbits. ApJ 111, 134–141.

Yamada, M., Sasaki, S., Nagahara, H., Fujiwara, A., Hasegawa, S., Yano, H., Hiroi, T., Ohashi, H., Otake, H., 1999. Simulation of space weathering of planet-forming materials: Nanosecond pulse laser irradiation and proton implantation on olivine and pyroxene samples. Earth, Planets and Space 51, 1255–1265.

Yano, H., Hirai, T., Fujii, M., Okamoto, C., Tanaka, M., 2014. ALADDIN first results. Nature Geoscience, in preparation.

Yano, H., Tanaka, M., Okamoto, C., Hirai, T., Ogawa, N., Hasegawa, S., Iwai, T., Okudaira, K., 2011. Cosmic Dust Detection by the IKAROS-Arrayed Large-Area Dust Detectors in Interplanetary Space (ALADDIN) from the Earth to Venus, in: Lunar and Planetary Institute Science Conference Abstracts, p. 2647.

Zuckerman, B., 2001. Dusty circumstellar disks. Annual Review of Astronomy and Astrophysics 39, 549–580.